

INFORMATION TO USERS

This manuscript has been reproduced from the microfilm master. UMI films the text directly from the original or copy submitted. Thus, some thesis and dissertation copies are in typewriter face, while others may be from any type of computer printer.

The quality of this reproduction is dependent upon the quality of the copy submitted. Broken or indistinct print, colored or poor quality illustrations and photographs, print bleedthrough, substandard margins, and improper alignment can adversely affect reproduction.

In the unlikely event that the author did not send UMI a complete manuscript and there are missing pages, these will be noted. Also, if unauthorized copyright material had to be removed, a note will indicate the deletion.

Oversize materials (e.g., maps, drawings, charts) are reproduced by sectioning the original, beginning at the upper left-hand corner and continuing from left to right in equal sections with small overlaps.

Photographs included in the original manuscript have been reproduced xerographically in this copy. Higher quality 6" x 9" black and white photographic prints are available for any photographs or illustrations appearing in this copy for an additional charge. Contact UMI directly to order.

ProQuest Information and Learning
300 North Zeeb Road, Ann Arbor, MI 48106-1346 USA
800-521-0600

UMI[®]

UNIVERSITY OF OKLAHOMA

GRADUATE COLLEGE

AVO POLARIZATION ATTRIBUTES

AND HODOGRAMS

A Dissertation

SUBMITTED TO THE GRADUATE FACULTY

in partial fulfillment of the requirements for the

degree of

Doctor of Philosophy

By

Patrice NSOGA MAHOB

Norman, Oklahoma

2001

UMI Number: 3025984

UMI[®]

UMI Microform 3025984

Copyright 2001 by Bell & Howell Information and Learning Company.

All rights reserved. This microform edition is protected against
unauthorized copying under Title 17, United States Code.

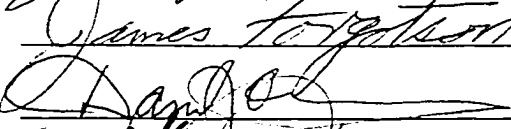
Bell & Howell Information and Learning Company
300 North Zeeb Road
P.O. Box 1346
Ann Arbor, MI 48106-1346

© Copyright by Patrice NSOGA MAHOB 2001
All Rights Reserved.

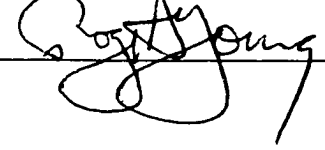
AVO POLARIZATION ATTRIBUTES AND HODOGRAMS

**A Dissertation APPROVED FOR THE
SCHOOL OF GEOLOGY AND GEOPHYSICS**

BY


James Forjsten

Dan Jones

Luther White

Doug S. E.

Roger Young

ACKNOWLEDGEMENTS

I am highly indebted to my advisor, Dr. John P. Castagna for his support. His guidance, collaboration, expertise, motivation, and encouragement are responsible for the completion of this work. He has been of great help during the past years, and a “big brother” during “hard times”. He gave me the opportunity to learn more than I had hoped for.

I wish to thank all of my committee members, Drs. James M. Forgotson, Daniel J. O’Meara Jr., Luther White, Roger A. Young, and Doug J. Foster for their time, invaluable comments, and their encouragement through the years.

I am very appreciative to the financial support of my Doctorate program by the School of Geology and Geophysics, the Institute of Exploration and Development Geosciences, the Sarkeys Energy Center, and the Society of Exploration Geophysicists (SEG). The National Association for Black Geologists and Geophysicists (NABGG) also partially supported my program.

I would like to express my gratitude to Chevron Corporation for providing the seismic data utilized in this study and for providing me with substantial financial support.

I would like also to thank all the staff, students, and professors at the School of Geology and Geophysics and other associated Research Institutes for their continuous assistance and help. A special thanks goes to Dr. William J. Lamb for the useful discussions and advice during my program, and to my “mom” Donna S. Mullins for all the love and moral support during my years at the University of Oklahoma.

I am very grateful to the support provided by my “adopted” brother Daniel Moussa Samake during the hard times.

I wish to dedicate this work to my parents, Ruth and Jacques Mahob-ma-Nkou for investing and believing in education. All the thanks to my brothers and sisters, Aime Mamert, Jean-Claude, Emmanuel Marin, Job Jules, Michele Flore, and Rebecca Marlyse for their unconditional love and encouragement. May this work be always a great source of motivation for them.

Lastly, I would like to thank all my friends for their encouragement, love, and suggestions. Without you, I would never be who I am today.

TABLE OF CONTENTS

	<i>Page</i>
ACKNOWLEDGEMENTS	iv
LIST OF FIGURES	x
LIST OF TABLES	xv
ABSTRACT	xvi
Chapter 1: INTRODUCTION	1
1.1 Importance of AVO Attributes	1
1.2 Conventional AVO Attributes	2
1.3 Why Polarization Attributes	4
1.4 Outline of the Dissertation	5
Chapter 2: SEISMIC ENERGY PARTITIONING IN ISOTROPIC MEDIA	7
2.1 Seismic Wave Partitioning at a Boundary	7
2.1.1 Snell's Law	7
2.2 Knott and Zoeppritz Equations	9
2.2.1 Derivation of the Knott and Zoeppritz equations	11
2.2.2 Approximations to the Knott and Zoeppritz equations ...	17
Chapter 3: CONVENTIONAL AVO ATTRIBUTES	22
3.1 AVO Attributes	22

3.2 Other AVO Attributes	24
Chapter 4: AVO HODOGRAMS AND POLARIZATION ANGLE	27
4.1 AVO Hodograms	27
4.2 AVO Hodogram Construction	29
4.3 Polarization Angle	32
4.4 Polarization Angle Difference	34
Chapter 5: POLARIZATION ATTRIBUTES	37
5.1 The AVO Strength	37
5.2 The Linear-Correlation Coefficient	40
5.3 The Product of AVO Strength and Polarization Angle Difference	41
Chapter 6: MODELING EXAMPLES	43
6.1 Model	43
6.2 Window Size Analysis	46
6.3 Wave Propagation and Processing Effects on Polarization Attributes	58
6.4 Thin Layer Modeling	66
Chapter 7: A CASE STUDY	74
7.1 Study Area	74
7.2 Seismic Data	77

7.3 Conventional AVO Attributes	84
7.4 Polarization Attributes	101
7.5 Discussion.	124
Chapter 8: CONCLUSIONS AND RECOMMENDATIONS.....	126
8.1 Conclusions	126
8.2 Recommendations.....	127
REFERENCES.....	129
APPENDIX A MATRIX REPRESENTATION OF THE KNOTT-ZOEPPRITZ EQUATIONS	133
APPENDIX B DERIVATION OF THE POLARIZATION VECTOR COMPONENTS.....	136

LIST OF FIGURES

<i>Figure</i>		<i>Page</i>
2.1	Partitioning of seismic wave at a boundary between two infinite isotropic media	8
2.2	Reflection of compressional waves at an interface between two elastic media	13
3.1	Plane-wave reflection coefficients at the top of each gas sand	25
3.2	AVO intercept versus gradient crossplot showing four possible quadrants and the relative positions of the gas sand classes	26
4.1	Schematic diagram of reflection at a boundary between two media ...	28
4.2	Intercept-gradient crossplot showing an anomalous trend that is embedded in a background trend	31
4.3	Angle of polarization definition.	36
5.1	Definition of the AVO strength attribute	39
5.2	Linear-correlation coefficient attribute and sample points scattering ..	42
6.1	Schematic diagram of the flat-layered model used for synthetic gather generation	45
6.2	Synthetic CDP gather generated from the flat-layered model	47
6.3	Extracted intercept and gradient traces along with the synthetic gather	48
6.4a	Display of the synthetic gather polarization angle for different analysis window sizes: 10 ms, 20 ms, 50 ms, and 200 ms.....	51
6.4b	Overlay of the synthetic gather polarization angle computed using different time window sizes.	52
6.5a	Display of the synthetic gather strength for different analysis window sizes: 10 ms, 20 ms, 50 ms, and 200 ms	53
6.5b	Overlay of the synthetic gather strength attribute computed using	

	different time window sizes	54
6.6a	Display of the synthetic gather linear-correlation coefficient attribute for different analysis window sizes: 10 ms, 20 ms, 50 ms, and 200 ms	55
6.6b	Overlay of the synthetic gather linear-correlation coefficient attribute computed using different time window sizes	56
6.7	AVO hodogram of the event for the top of B Sand, D Sand, G1 Sand, and I Sand	57
6.8	Wave propagation and processing effects on the AVO hodogram for the top B Sand reflection	64
6.9	Polarization angle and linear-correlation coefficient for the top B Sand event	65
6.10	Extracted intercept and gradient traces along with the synthetic gather from the thin-layered model	68
6.11	Background polarization angle determination	69
6.12	Display of intercept trace, gradient trace, polarization angle, strength, and linear-correlation coefficient computed from the synthetic gather with layer thickness above the tuning thickness	70
6.13	Display of intercept trace, gradient trace, polarization angle, strength, and linear-correlation coefficient computed from the synthetic gather with thin layers	71
6.14	Display of the synthetic gather, the product of strength and polarization angle difference, and the linear-correlation coefficient for the thick-layered model	72
6.15	Display of the synthetic gather, the product of strength and polarization angle difference, and the linear-correlation coefficient for the thin-layered model	73
7.1	Map of the study area.....	75
7.2	Generalized stratigraphy of the Barrow-Dampier sub-basin.....	76
7.3	Grid map with seismic lines of interest.....	79
7.4a	Seismic tie line at well 1.....	80

7.4b	Seismic tie line at well 2.....	81
7.4c	Seismic tie line at well 3.....	82
7.4d	Seismic tie line at well 4.....	83
7.5a	AVO intercept for seismic line 1.....	85
7.5b	AVO gradient for seismic line 1.....	86
7.5c	AVO product for seismic line 1.....	87
7.5d	Scaled Poisson's ratio change for seismic line 1.....	88
7.6a	AVO intercept for seismic line 2.....	89
7.6b	AVO gradient for seismic line 2.....	90
7.6c	AVO product for seismic line 2.....	91
7.6d	Scaled Poisson's ratio change for seismic line 2.....	92
7.7a	AVO intercept for seismic line 3.....	93
7.7b	AVO gradient for seismic line 3.....	94
7.7c	AVO product for seismic line 3.....	95
7.7d	Scaled Poisson's ratio change for seismic line 3.....	96
7.8a	AVO intercept for seismic line 4.....	97
7.8b	AVO gradient for seismic line 4.....	98
7.8c	AVO product for seismic line 4.....	99
7.8d	Scaled Poisson's ratio change for seismic line 4.....	100
7.9	Background polarization angle determination for seismic line 2	102
7.10a	Polarization angle for seismic line 1.....	104
7.10b	Polarization angle difference for seismic line 1.....	105

7.10c	AVO strength for seismic line 1.....	106
7.10d	Polarization product for seismic line 1.....	107
7.10e	Square of linear-correlation coefficient for seismic line 1.....	108
7.11a	Polarization angle for seismic line 2.....	109
7.11b	Polarization angle difference for seismic line 2.....	110
7.11c	AVO strength for seismic line 2.....	111
7.11d	Polarization product for seismic line 2.....	112
7.11e	Square of linear-correlation coefficient for seismic line 2.....	113
7.12a	Polarization angle for seismic line 3.....	114
7.12b	Polarization angle difference for seismic line 3.....	115
7.12c	AVO strength for seismic line 3.....	116
7.12d	Polarization attribute for seismic line 3.....	117
7.12e	Square of linear-correlation coefficient for seismic line 3.....	118
7.13a	Polarization angle for seismic line 4.....	119
7.13b	Polarization angle difference for seismic line 4.....	120
7.13c	AVO strength for seismic line 4.....	121
7.13d	Polarization product for seismic line 4.....	122
7.13e	Square of linear-correlation coefficient for seismic line 4.....	123

LIST OF TABLES

<i>Table</i>		<i>Page</i>
2.1	Typical values of Poisson's ratio in several types of rocks	21
6.1	Elastic parameters of the flat-layered model	44
6.2	Time equivalence between the window size and the wave period	49
6.3	Optimum window size for the computation of polarization attributes of the synthetic data	58
6.4	Average values for the top B Sand event of the polarization angle and the linear-correlation coefficient	60
6.5	Calculated tuning thickness values of the sand units and their respective thickness used in the thin layer model	66
7.1	Average background angle values for seismic line 2	103

ABSTRACT

An alternative approach to identifying AVO anomalies is to consider the AVO polarization in the intercept-gradient (A-B) plane. This method does not require deviations or separations from a background trend exhibited in traditional crossplots such as intercept-gradient (A-B) or near trace-far trace (N-F). A benefit of the hodogram or polarization method is that the wavelet is taken into consideration as it is convolved with the reflection coefficient series. Crossplotted intercept and gradient are polarized along a “background trend” for non-anomalous events and at angles different from the “background trend” for anomalous events.

New attributes resulting from this methodology include (1) the polarization angle, (2) the polarization angle difference, (3) the AVO strength, (4) the linear-correlation coefficient, and (5) the product of AVO strength and polarization angle difference. These different attributes can then be used to enhance or to show the AVO effects for any given event on of a seismic trace (seismic section). The results obtained from a flat-layered model made of a succession of gas and brine sand layers encased in shale units are shown. Processing and wave propagation effects, and thin-layer modeling are also investigated.

A case study using seismic data from the Gorgon field of the NW Shelf of Australia is done to validate the methodology. Application of this new scheme can help one recognize AVO anomalies and enhances AVO interpretation.

Chapter 1

INTRODUCTION

1.1 Importance of AVO Attributes

A better understanding of large seismic amplitudes and associated features noticed on stacked sections by exploration geophysicists in the late 1960's and the early 1970's led to amplitude variation with offset (AVO) analysis (Backus and et., 1982; Ostrander, 1982 and 1984). These amplitude anomalies are associated with hydrocarbon-saturated (gas and light oil) sandstone in environments of young clastic sediments. AVO analysis has been used as a direct hydrocarbon indicator based upon difference in the response of the compressional-wave velocity (V_P), the shear-wave velocity (V_S) and density contrast between hydrocarbon-saturated sands and shales. More specifically, the AVO response is related to contrasts in Poisson's ratio (a direct function of V_P/V_S ratio) when hydrocarbons are present in pore spaces.

For the past two decades, AVO attributes have been used to determine anomalous amplitude behavior in seismic reflection data. The attributes are statistical values that are calculated by a given algorithm and are directly related to the seismic traces examined. They can be either displayed as attribute stacks (near-offset stack, far-offset stack, intercept, gradient, etc.) for a better identification of amplitude variations or crossplotted to provide a good characterization of trace amplitude changes on seismic data, thereby enhancing subtle AVO anomaly interpretation, particularly in the case of data with low signal-to-noise ratio.

Crossplotting AVO attributes is a means of qualifying any anomalous seismic response; that is, it helps in establishing trends against which anomalous amplitude behavior can be seen. Discussion of such AVO indicators may be found in Castagna et al. (1998), Castagna and Smith (1994), Foster et al. (1997), Sams (1998), and Smith and Gidlow (1987). Successful utilization of an AVO crossplot requires a deviation of anomalous events (hydrocarbon-saturated reservoirs) from a well-defined 'background' trend.

AVO attributes have been used in a wide range of applications in exploration and production. They can be applied effectively in discriminating hydrocarbon-filled reservoirs (e.g. Hidalgo and Haryono, 2000). Moreover, to improve prospect evaluations in new areas such as deep offshore environments, AVO attributes are being utilized as an analysis tool for quantitative prospect ranking (e.g. Cardamone et al., 1998; Adamick et al., 1994). In addition, these attributes are considered to be a valuable tool of evaluating anomalous seismic amplitude responses on large volume 2-D and 3-D datasets (e.g. Barton and Gullette, 1996). Furthermore, an evolving application of AVO attributes is in the detection and characterization of fractured reservoirs (fracture related anisotropy detection) (e.g. Rueger and Tsvankin, 1995; Ramos, 1996; Lefeuvre, 1994).

1.2 Conventional AVO Attributes

In recent years, the exploration geophysics community has shown a growing interest in the use of AVO attributes to characterize hydrocarbon-saturated rocks. A better understanding of amplitude variation with offset analysis has helped improve the

use of the methodology (e.g. Ostrander, 1984; Ross, 2000). However, there has been much misuse of AVO analysis (Allen and Peddy, 1993).

Characterizing or identifying hydrocarbon reservoirs has been one of the most important applications of AVO to oil and gas exploration or development. This characterization is useful in that anomalous seismic amplitudes and related attributes usually correspond to rocks with noticeable physical property contrasts such as density (ρ), porosity (ϕ), or Poisson's ratio ($\Delta\sigma$). Common AVO attributes are the intercept (A) and the gradient (B). The intercept is related to the near-offset trace (N); whereas, the gradient is related to the change in amplitude from zero-offset trace. The intercept and the gradient can be extracted by regression analysis on the CDP gathers (pre-stack domain). The near and far traces result from partial stacking of near and far offset ranges. There are many AVO attributes that result from linear combinations of intercept and gradient. Some of the attributes are:

- intercept times gradient ($A*B$),
- intercept plus gradient ($A+B$) or scaled Poisson's ratio,
- intercept minus gradient ($A-B$) or scaled S-wave reflectivity,
- fluid factor, ΔF .

The AVO attributes can be displayed as color plots or stacks (Wrolstad, 1988) so that variations can be easily identified. Crossplotting the attributes is another means of qualifying any anomalous seismic response. AVO crossplots such as the intercept-gradient crossplot have been very helpful in characterizing both water- and hydrocarbon-saturated rocks.

1.3 Why Polarization Attributes?

AVO crossplotting is used successfully as an AVO indicator when there is a deviation or separation of anomalous points related to hydrocarbons (gas or light oil) from the well-defined brine sand and shale trend. However, when there is no deviation from the background trend, the AVO crossplot cannot be used as an AVO indicator. Rather, determining all preferred orientations of the sample points in the A-B plane is an alternative approach (Keho, 2000).

This approach does not require deviations from a background trend and takes into consideration the wavelet as it is convolved with the reflectivity series. It is important to understand that at any given interface, sample points resulting from a reflection have a preferred orientation and can be spread across the four quadrants in the A-B plane (intercept – gradient space). The angle defining any preferred orientation in the intercept-gradient space is called the polarization angle. Non-anomalous events related to shales and brine sands can exhibit a well-defined orientation (or background angle). Hence, events at angles different from the background angle can be considered as anomalous. Therefore, the angle of polarization can be used in identifying AVO anomalies of Class I, II, III, and IV based on the modified gas sand classification of Rutherford and Williams (1989).

One of the main benefits of this approach is the enhancement of seismic anomalies that are either exhibited as small anomalies or embedded in the background trend using traditional AVO indicators (AVO crossplot). For example, an event corresponding to a gas sand whose points are plotted close to the background trend on the A-B crossplot will not show a large separation (distance from the trend). However, such

an event will show up as a large anomaly based on polarization angle and related attributes.

The proposed attributes resulting from this methodology are:

- (1) the polarization angle
- (2) the polarization angle difference
- (3) the AVO strength (distance from origin in A-B plane)
- (4) the product of strength and polarization angle difference
- (5) the linear-correlation coefficient

1.4 Outline of the Dissertation

This dissertation comprises eight chapters.

Chapter 1 is the introduction that covers the importance of AVO attributes, the discussion on conventional AVO attributes, and the benefit of polarization attributes.

Chapter 2 discusses the concept of seismic energy partitioning at a boundary between two isotropic media. The Snell's law is introduced. Then, the P-wave reflection coefficient and its relationship to the angle of incidence are presented through derivations from Knott-Zoeppritz equations.

In Chapter 3, the most used AVO attributes are presented. The main derivations and equations underlying these attributes are shown. The conventional attributes mentioned are: (1) intercept, A ; (2) gradient, B ; (3) product, $A \times B$; (4) sum, $A + B$;

(5) difference, $A - B$; (6) fluid factor, ΔF . Other AVO attributes, less frequently used, are also discussed.

Chapter 4 introduces the notion of AVO hodogram as well as the construction of the hodogram. The attributes related to the AVO hodogram such as the polarization angle and the polarization angle difference are discussed. The formulation of these attributes is derived.

In Chapter 5, the other polarization attributes are introduced. These attributes are the strength, the product of strength and polarization angle difference, and the linear-correlation coefficient. The methodology used for the computation of the attributes is presented.

In Chapter 6, the window size for the analysis is tested on synthetic data generated from a flat-layered model. In addition, the wave propagation and processing effects on polarization attributes are simulated by taking into consideration (1) phase shift, (2) loss of frequency bandwidth, and (3) superposition of the previous two effects on far-offset traces or gradient trace.

Chapter 7 is a case study done on real seismic gathers from NW Shelf, Australia to investigate the methodology.

Chapter 8 presents the conclusions drawn from the novel AVO attributes.

Chapter 2

SEISMIC ENERGY PARTITIONING IN ISOTROPIC MEDIA

The preliminary concept of seismic energy partitioning at a boundary between two isotropic media is introduced. Snell's law is recalled. Then, the P-wave reflection coefficient and its relationship to the incidence angle are presented through derivations from Knott-Zoeppritz equations.

2.1 Seismic Wave Partitioning at a Boundary

Despite the fact that there is no isolated boundary, but a series of layers or boundaries in exploration geophysics, the separation of seismic energy at an interface is better understood when dealing with such a boundary. This separation of plane wave energy, known as energy partitioning, is fundamental to AVO analysis.

2.1.1 *Snell's Law*

A compressional plane wave (P-wave) impinges the interface of two semi-infinite elastic isotropic homogeneous media at an angle of incidence θ_1 as depicted in Figure 2.1. Due to mode conversion, at any angle other than the normal incidence angle, the incident P-wave produces:

- (1) a transmitted P-wave,
- (2) a transmitted S-wave,
- (3) a reflected P-wave, and
- (4) a reflected S-wave.

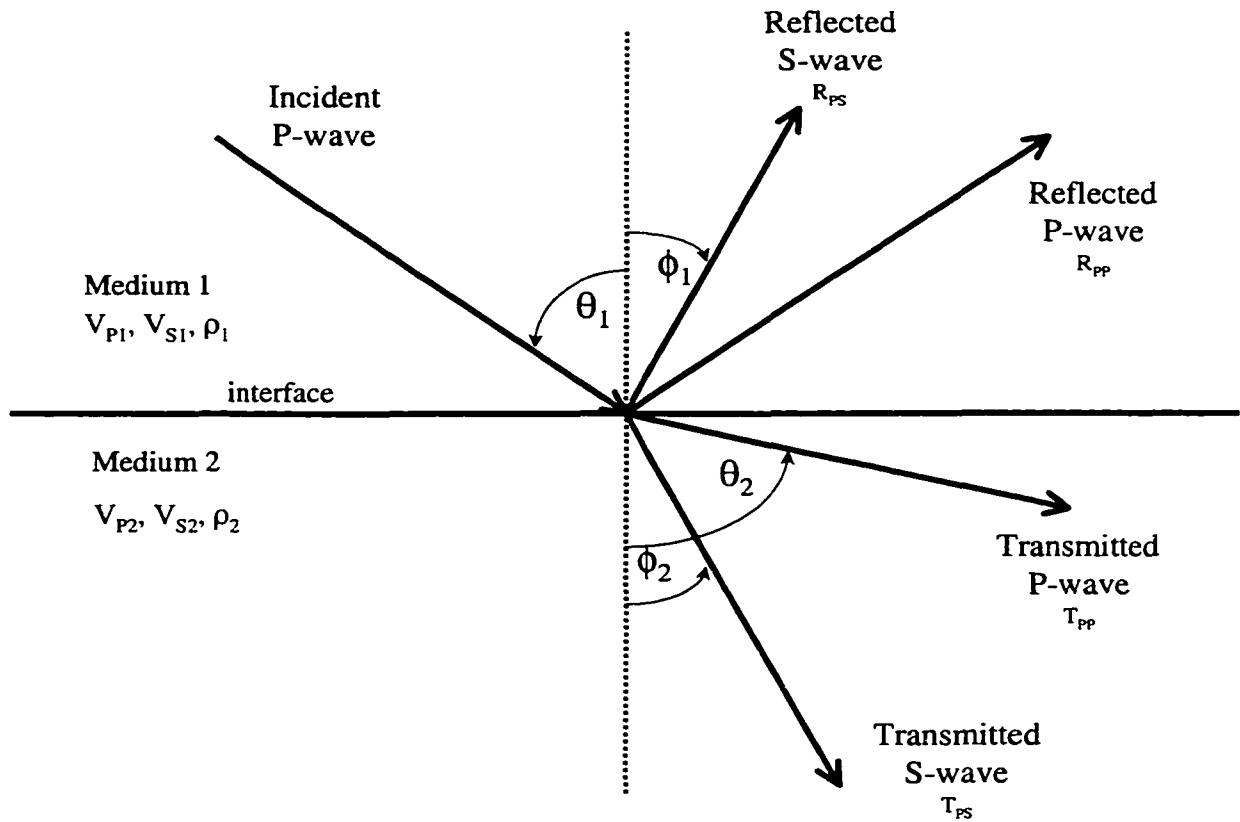


Figure 2.1. Partitioning of seismic wave at a boundary between two infinite isotropic media (Modified from Castagna, 1993).

The incidence angle and the related transmission and reflection angles at the interface are expressed according to Snell's law,

$$p = \frac{\sin \theta_1}{V_{P1}} = \frac{\sin \theta_2}{V_{P2}} = \frac{\sin \phi_1}{V_{S1}} = \frac{\sin \phi_2}{V_{S2}} \quad (2.1)$$

where

V_{P1} is P-wave velocity in medium 1,
 V_{P2} is P-wave velocity in medium 2,
 V_{S1} is S-wave velocity in medium 1,
 V_{S2} is S-wave velocity in medium 2,
 θ_1 is incident P-wave angle,
 θ_2 is transmitted P-wave angle,
 ϕ_1 is reflected S-wave angle,
 ϕ_2 is transmitted S-wave angle, and

is ray parameter.

2.2 Knott and Zoeppritz Equations

In the isotropic case, the Zoeppritz equations (Sheriff, 1991) give the reflection and transmission coefficients for plane waves as a function of angle of incidence and six independent elastic parameters, which are P- and S-wave velocities and densities on both sides of the interface between the two media.

By definition, the P-wave reflection coefficient as a function of incidence angle, $R_{PP}(\theta_1)$, is the ratio of the amplitude of the reflected P-wave to that of the incident P-wave. Similarly, the P-wave transmission coefficient, $T_{PP}(\theta_1)$, is the ratio of the amplitude of the transmitted P-wave to that of the incident P-wave. In addition, $R_{PS}(\theta_1)$

is the ratio of the amplitudes of reflected S-wave and incident P-waves, and $T_{PS}(\theta_1)$ is the ratio of transmitted S-wave and incident P-waves amplitudes.

There is no mode conversion at normal incidence, and the P-wave reflection coefficient R_p is given by:

$$R_p = \frac{I_{P2} - I_{P1}}{I_{P2} + I_{P1}} \approx \frac{1}{2} \frac{\Delta I_p}{I_{PA}} \quad (2.2)$$

where

I_p is the continuous P-wave impedance profile,

I_{P1} is impedance of medium 1 = $\rho_1 * V_{P1}$,

ρ_1 is density of medium 1,

I_{P2} is impedance of medium 2 = $\rho_2 * V_{P2}$

ρ_2 is density of medium 2,

I_{PA} is average impedance across the interface = $(I_{P2} + I_{P1})/2$, and

$\Delta I_p = I_{P2} - I_{P1}$.

The P-wave transmission coefficient at normal incidence, T_p , is given by:

$$T_p = 1 + R_p \quad (2.3)$$

The variation of reflection and transmission coefficients relative to the angle of incidence (or corresponding increasing offset) is the fundamental basis for AVO analysis.

For all non-normal incidence angles, Knott (1899) and Zoeppritz (1919) described the continuity of displacement and stress at the reflecting interface as boundary conditions to solve for the reflection and transmission coefficients in the direction of

wave propagation as a function of incident angle and the media elastic properties such as densities, bulk and shear moduli. The complexity of these equations revealed little physical insight, and it was not until the use of digital computers that these equations were applied to exploration (Young and Braile, 1976; Cerveny and Ravindra, 1971). Aki and Richards (1980) and Waters (1981) gave an easy to solve form to the equations:

$$Q = P^{-1}R \quad (2.4)$$

where Q , P , and R are given in Appendix A.

The density and the P-and S-wave velocities of each medium determine completely the coefficients R_{PP} , R_{PS} , T_{PP} , and T_{PS} at any given incident angle θ_1 for an interface between elastic media.

2.2.1 Derivation of the Knott and Zoeppritz equations

Reflection coefficient series at oblique angle of incidence can be obtained from the Knott-Zoeppritz equations that are derived below following Ewing et al. (1957).

Consider two semi-infinite media with different acoustic impedances in contact. A wave incident at this interface will generally produce reflected and converted compressional and shear waves (see Figure 2.2). The disturbance produced by an incident plane compressional wave can be represented by:

$$\begin{aligned}
\varphi &= A_1 \exp[ik(ct - x + az)] + A_2 \exp[ik(ct - x - az)] \\
\psi &= B_2 \exp[ik(ct - x - bz)] \\
\varphi' &= A' \exp[ik(ct - x + a'z)] \\
\psi' &= B' \exp[ik(ct - x + b'z)]
\end{aligned}
\tag{2.5}$$

where

$$\begin{aligned}
a &= \tan E = \sqrt{c^2/\alpha^2 - 1}, & c > \alpha \\
b &= \tan F = \sqrt{c^2/\alpha^2 - 1}, & c > \beta \\
a' &= \tan E' = \sqrt{c^2/\alpha'^2 - 1}, & c > \alpha' \\
&= -i\sqrt{1 - c^2/\alpha'^2}, & c < \alpha' \\
b' &= \tan F' = \sqrt{c^2/\beta'^2 - 1}, & c > \beta' \\
&= -i\sqrt{1 - c^2/\beta'^2}, & c < \beta'
\end{aligned}
\tag{2.6}$$

and

$$k = \frac{\omega}{c} \tag{2.7}$$

with

$$c = \frac{\alpha}{\cos E} = \frac{\beta}{\cos F} = \frac{\alpha'}{\cos E'} = \frac{\beta'}{\cos F'} \tag{2.8}$$

where α , β , α' , β' , are the compressional and shear wave velocities and E , F , E' , F' are the angles shown in Figure 2.2.

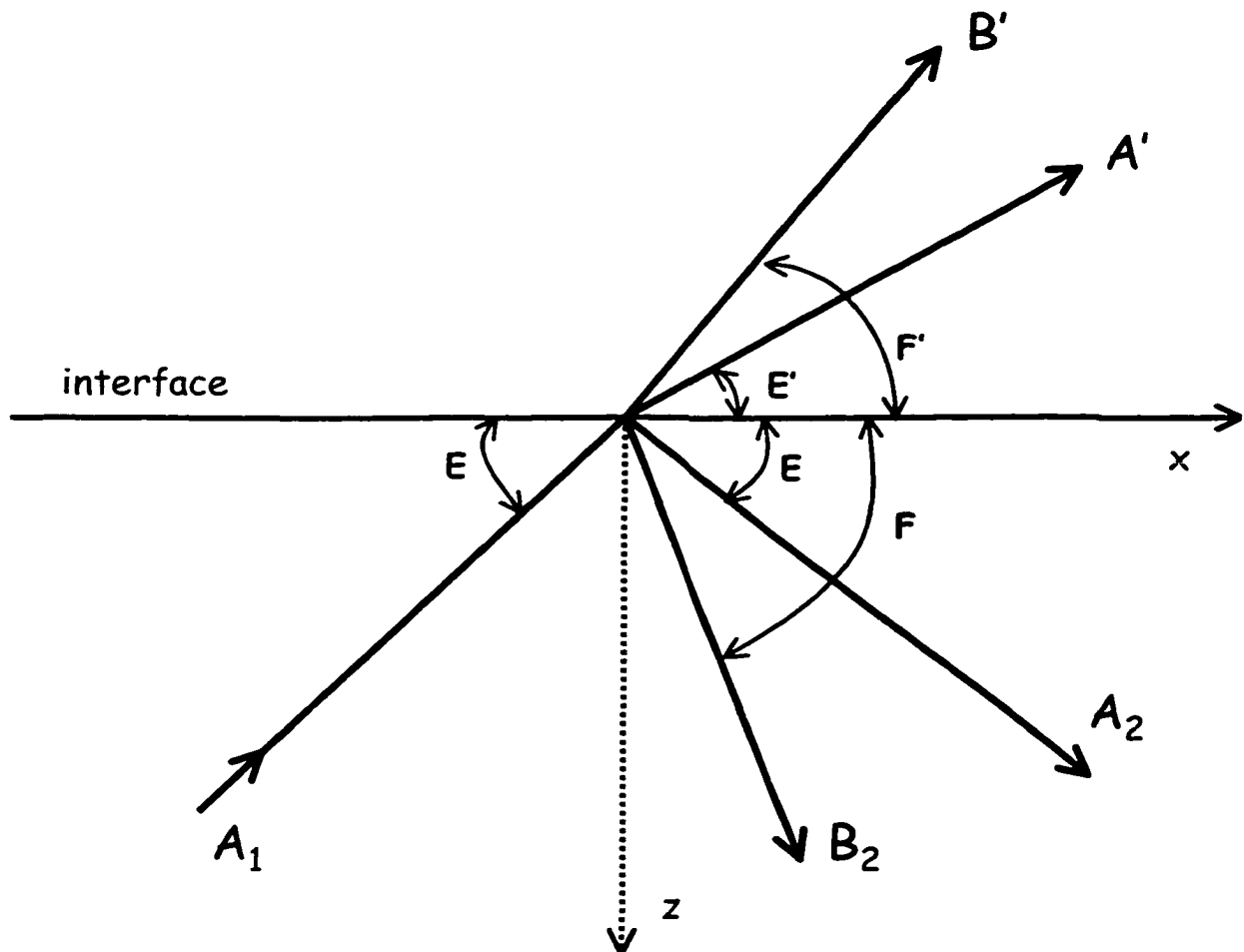


Figure 2. 1. Reflection of compressional waves (P waves) at an interface between two elastic media. If A_1' is the amplitude of the incident compressional then A_2 and B_2 are the amplitude of the reflected P and SV waves and A' and B' are the amplitudes of the refracted (transmitted) P and SV waves (Adapted from Castagna, 1997- 2001).

Four boundary conditions are imposed: the first two are related to the continuity of two displacement components, and the last two to the continuity of two stresses.

For the first component of displacement

$$u = \frac{\partial \varphi}{\partial x} - \frac{\partial \psi}{\partial z} = u' = \frac{\partial \varphi'}{\partial x} - \frac{\partial \psi'}{\partial z} \quad (2.9)$$

By considering $z = 0$ from Equations 2.5, substituting in Equation 2.9, and rearranging common terms, it gives

$$(A_1 + A_2) + bB_2 = A' + b' B' \quad (2.10)$$

This is the first Knott-Zoeppritz equation.

For the second component of displacement

$$w = \frac{\partial \varphi}{\partial z} + \frac{\partial \psi}{\partial x} = w' = \frac{\partial \varphi'}{\partial z} + \frac{\partial \psi'}{\partial x} \quad (2.11)$$

By considering $z = 0$ from Equations 2.5, substituting in Equation 2.11, and rearranging common terms, it gives

$$a(A_1 - A_2) - B_2 = a' A' - B' \quad (2.12)$$

This is the second Knott-Zoeppritz equation.

For the second component of stress we have at $z = 0$

$$p_{zz} = \lambda \nabla^2 \varphi + 2\mu \left(\frac{\partial^2 \varphi}{\partial z^2} + \frac{\partial^2 \psi}{\partial x \partial z} \right) = p_{zz}' = \lambda' \nabla'^2 \varphi' + 2\mu' \left(\frac{\partial^2 \varphi'}{\partial z'^2} + \frac{\partial^2 \psi'}{\partial x' \partial z'} \right) \quad (2.13)$$

where

$$\nabla^2 \varphi = \frac{\partial^2 \varphi}{\partial x^2} + \frac{\partial^2 \varphi}{\partial z^2} \quad (2.14)$$

and

$$\mu = \rho \beta^2 \quad (2.15)$$

$$\lambda = \alpha^2 \rho - 2\mu$$

By considering $z = 0$ from Equations 2.5, substituting in Equation 2.13, and canceling common terms, it gives

$$(A_1 + A_2)(-\lambda - \lambda a^2 - 2\mu a^2) - 2\mu b B_2 = A'(-\lambda' - \lambda' a'^2 - 2\mu' a'^2) + 2\mu' b' B' \quad (2.16)$$

Some algebraic manipulation is required to put Equation 2.16 into the form given by Ewing et al. (1957). First collecting the terms in a^2 , next using Equations 2.6 and 2.15, then factoring out ρ

$$\rho(A_1 + A_2)(2\beta^2 - c^2) - 2\mu b B_2 = \rho' A'(2\beta'^2 - c^2) + 2\mu' b' B' \quad (2.17)$$

From Equation 2.6, it is evident that

$$2\beta^2 - c^2 = \beta^2(1 - b^2) \quad (2.18)$$

$$2\beta'^2 - c^2 = \beta'^2(1 - b'^2)$$

Substituting in Equation 2.17 and rearranging gives

$$\rho\beta^2(-(b^2 - 1)(A_1 + A_2) - 2bB_2) = \rho'\beta'^2(-(b'^2 - 1)A' + 2b'B') \quad (2.19)$$

which is in the form given by Ewing et al. (1957) with $B_1 = 0$.

This is the third Knott-Zoeppritz equation.

For the first stress component at $z = 0$

$$p_{zx} = \mu \left(2 \frac{\partial^2 \varphi}{\partial x \partial z} + \frac{\partial^2 \psi}{\partial x^2} - \frac{\partial^2 \psi}{\partial z^2} \right) = p'_{zx} = \mu' \left(2 \frac{\partial^2 \varphi'}{\partial x \partial z} + \frac{\partial^2 \psi'}{\partial x^2} - \frac{\partial^2 \psi'}{\partial z^2} \right) \quad (2.20)$$

By considering $z = 0$ from Equations 2.5, substituting in Equation 2.20, canceling common terms, and rearranging gives

$$\rho\beta^2(2a(A_1 - A_2) + (b^2 - 1)B_2) = \rho'\beta'^2(2a'A' + (b'^2 - 1)B') \quad (2.21)$$

This is the fourth and final Knott-Zoeppritz equation.

2.2.2 Approximations to the Knott-Zoeppritz equations

Due to the complexity of the Knott-Zoeppritz equations, many approximations have been developed for practical applications, particularly in revealing the information contained in the amplitude behavior.

By assuming small changes in layer properties, Bortfeld (1961) linearized the Zoeppritz equations:

$$R_{pp}(\theta_1) \approx \frac{1}{2} \ln \left[\frac{V_{p2} \rho_2 \cos \theta_1}{V_{p1} \rho_1 \cos \theta_2} \right] + \left(\frac{\sin \theta_1}{V_{p1}} \right)^2 (V_{s1}^2 - V_{s2}^2) \times \left[2 + \frac{\ln \left(\frac{\rho_2}{\rho_1} \right)}{\ln \left(\frac{V_{s2}}{V_{s1}} \right)} \right] \quad (2.22)$$

This same linearization approach was used by Richards and Frasier (1976) and Aki and Richards (1980) to derive a relationship that is only a function of the variations in density, P-wave velocity, and S-wave velocity across the boundary:

$$R_{pp}(\theta) \approx \frac{1}{2} (1 - 4p^2 V_{sa}^2) \left(\frac{\Delta \rho}{\rho_a} \right) + \frac{1}{2 \cos^2(\theta)} \times \frac{\Delta V_p}{V_{pa}} - 4p^2 V_{sa}^2 \frac{\Delta V_s}{V_{sa}} \quad (2.23)$$

where

$$\begin{aligned} \Delta \rho &= \rho_2 - \rho_1, \\ \Delta V_p &= V_{p2} - V_{p1}, \\ \Delta V_s &= V_{s2} - V_{s1}, \\ \rho_a &= (\rho_2 + \rho_1)/2, \end{aligned}$$

$$\begin{aligned}
V_{Pa} &= (V_{P2} + V_{P1})/2, \\
V_{Sa} &= (V_{S2} + V_{S1})/2, \\
\theta &= (\theta_1 + \theta_2)/2
\end{aligned}$$

and p is the ray parameter as defined by Equation 2.1.

Chapman (1976) derived a linearized expression for the reflection coefficient that is accurate and gives an idea of the separate contributions of P-wave impedance changes (ΔZ_p), S-wave modulus change (ΔG), and P-wave velocity changes (ΔV_p):

$$\begin{aligned}
R_p(\theta) = & \frac{1}{2} \left[\frac{\Delta Z_p}{Z_p} \right] + \frac{1}{2} \left[\frac{\Delta V_p}{V_p} - \left(\frac{2\bar{V}_s}{V_p} \right)^2 \frac{\Delta G}{G} \right] \sin^2(\theta) \\
& + \frac{1}{2} \left[\frac{\Delta V_p}{V_p} \right] \tan^2(\theta) \sin^2(\theta)
\end{aligned} \tag{2.24}$$

where

$Z_p = \rho V_p$ is the P-wave impedance,

$G = \rho V_s^2$ is the shear modulus,

The bar on the top of the variable stands for average value from upper and lower medium.

The approximations are most valid for small contrasts of elastic properties:

$$\left| \frac{\Delta V_p}{V_p} \right| \ll 1, \tag{2.25a}$$

$$\left| \frac{\Delta V_s}{V_s} \right| \ll 1, \tag{2.25b}$$

and

$$\left| \frac{\Delta\rho}{\rho} \right| \ll 1, \quad (2.25c)$$

which is usually a good assumption.

Another form of the Aki and Richards (1980) approximation was presented by Shuey (1985) to parameterize in terms of the changes in density, P-wave velocity, S-wave velocity, and Poisson's ratio:

$$R_{pp}(\theta_1) \approx R_p + \left(A_0 R_p + \frac{\Delta\sigma}{(1-\sigma)^2} \right) \sin^2 \theta_1 + \frac{1}{2} \frac{\Delta V_p}{V_{pa}} (\tan^2 \theta_1 - \sin^2 \theta_1) \quad (2.26)$$

where

R_p is the normal incidence reflection coefficient,
 A_0 is given by

$$A_0 = B_0 - 2(1 + B_0) \left(\frac{1-2\sigma}{1-\sigma} \right) \quad (2.27)$$

and

$$B_0 = \frac{\frac{\Delta V_p}{V_{Pa}}}{\frac{\Delta V_p}{\Delta V_{Pa}} + \frac{\Delta \rho}{\Delta \rho_a}} \quad (2.28)$$

σ is the Poisson's ratio and is related to V_p/V_s ratio by

$$\sigma = \frac{\frac{1}{2} \left(\frac{V_p}{V_s} \right)^2 - 1}{\left(\frac{V_p}{V_s} \right)^2 - 1} \quad (2.29)$$

The main advantage of this linearization is that each term describes a different angular of the offset curve. The first term is the normal incidence reflection coefficient, the second term is significant for intermediate angles, and the third term predominates as the critical angle is approached.

Koefoed (1955) used the Zoeppritz equations to compute reflection coefficients as a function of Poisson's ratio changes on each side of the interface between the two media. The importance of Koefoed's result was to develop a better understanding of the physical properties of rocks, such as Poisson's ratio, that could affect noticeably reflection coefficients. Koefoed recognized that Poisson's ratio values published in the literature show a sufficiently wide variation that one could expect that the change in reflection coefficient with angle of incidence would be of practical significance in seismic prospecting. Table 2.1, modified from Ross (1992) and Domenico (1984), shows that Poisson's ratio varies not only with lithology but also with compaction and pore fluid.

Gas-charged pore fluid sediments (gas sands) have very low Poisson's ratio, which generally increases the Poisson's ratio contrast with the surrounding sediments, for example shales. In contrast, coals have large Poisson's ratio, which also produce large Poisson's ratio contrast if the surrounding sediments are consolidated sandstones for example. Poisson's ratio varies with the amount of clay minerals, properties of the reservoir fluid, pore pressure, porosity, temperature, and degree of compaction. For isotropic materials, Poisson's ratio generally ranges from 0 to 0.5 (for liquids).

Table 2. 1. Typical values of Poisson's ratio in several types of rocks.

Lithology / Pore Fluid	Poisson's Ratio
Unconsolidated shale	0.38 - 0.45
Consolidated shale	0.28 - 0.34
Unconsolidated Sandstone (brine)	0.30 - 0.35
Consolidated Sandstone	0.17 - 0.26
High Porosity Sandstone (brine)	0.35 - 0.42
Low Porosity Sandstone (tight)	0.17 - 0.26
Gas-Saturated Sandstone	0.10 - 0.16
Coal	0.37 - 0.45
Limestone	0.29 - 0.33
Dolomite	0.27 - 0.29
Salt	0.24 - 0.28

Chapter 3

CONVENTIONAL AVO ATTRIBUTES

In this chapter, the most used AVO attributes are presented. The main derivations and equations underlying these attributes are shown.

3.1. AVO Attributes

The conventional attributes related to the amplitude variation with offset analysis are the intercept (A) and the gradient (B). The intercept corresponds to the near-offset traces. For restricted angles of incidence, higher order terms of $\sin^2 \theta_i$ can be neglected and Equation 2.26 becomes linear in $\sin^2 \theta_i$:

$$R_{pp} \approx R_p + B \sin^2 \theta_i \quad (3.1)$$

where

R_p is the normal incidence reflection coefficient known as the “AVO intercept” or A . B is called the “AVO gradient” or “AVO slope” and is given by:

$$B = A_0 R_p + \frac{\Delta \sigma}{(1 - \sigma)^2} \quad (3.2)$$

For small angles, Wiggins et al.(1983) showed that if V_p/V_s ratio is nearly 2 then

$$B \approx R_p - 2R_s \quad (3.3)$$

where R_S is the normal incidence shear-wave reflectivity.

The above approximation is very useful because it simplifies AVO interpretations. In practice, AVO analysis is performed from measurements of seismic amplitudes, as opposed to direct reflection coefficient measurements.

Based on the sign of the intercept and gradient and their magnitude, a classification scheme for gas sands, shown in Figure 3.1, was developed by Rutherford and Williams (1989), then modified by Ross and Kinman (1995) and Castagna and Swan (1997). The relative positions of these Classes on an AVO crossplot (intercept-gradient plane) are depicted on Figure 3.2.

Some of the attributes result from linear combination of the intercept and gradient (Wroldstad, 1988; and Nelson, 1989). Among those attributes are:

- the AVO product that is the intercept times the gradient: (A * B),
- the AVO sum that is the sum of the intercept and the gradient: (A + B), sometimes known as the scaled Poisson's ratio (Hampson-Russell AVO)¹,
- the AVO difference that is the difference between the intercept and the gradient (Castagna et al., 1994): (A – B). It is also called the scaled S-wave reflectivity (Hampson-Russell AVO)¹.

Another commonly used attribute in AVO interpretation is the fluid factor (ΔF) defined by Smith and Gidlow (1987):

$$\Delta F = \frac{\Delta V_P}{V_{Pa}} - 1.16 \left(\frac{V_S}{V_P} \right) \frac{\Delta V_S}{V_{Sa}} \quad (3.4)$$

where V_S/V_P is the background S-wave to P-wave velocity ratio.

The use of range-limited stacks or partial stacks is also common. Near-offset, mid-offset, and far-offset stacks are displayed as attributes. The near-offset traces are related to the AVO intercept, whereas the mid- to far-offset traces correspond to the AVO gradient.

These AVO attributes are displayed as stacks (seismic plots) so that seismic anomalies can be identified and qualified. These attributes are found in most software packages at today leading edge of seismic technology such Hampson-Russell AVO or ProMAX².

3.2. Other AVO Attributes

Despite the good applicability and robustness of conventional attributes, there are other AVO attributes that can enhance seismic anomalies or help in the interpretation of amplitude variation with offset of pre-stack data. Some of the attributes are related to the intercept and the gradient either by their signs or by their magnitudes. The others are derived parameters from the estimation of the intercept (A) and the gradient (B). These AVO attributes are:

- the intercept times the sign of the gradient: $(A * \text{sign}(B))$,
- the sign of the intercept times the gradient: $(\text{sign}(A) * B)$,
- the angle of crossover,
- the Poisson's ratio reflectivity.

¹ Hampson-Russell AVO is a registered trademark of Hampson-Russell Software Services Inc.

² ProMAX is a registered trademark of Landmark Graphics Corporation

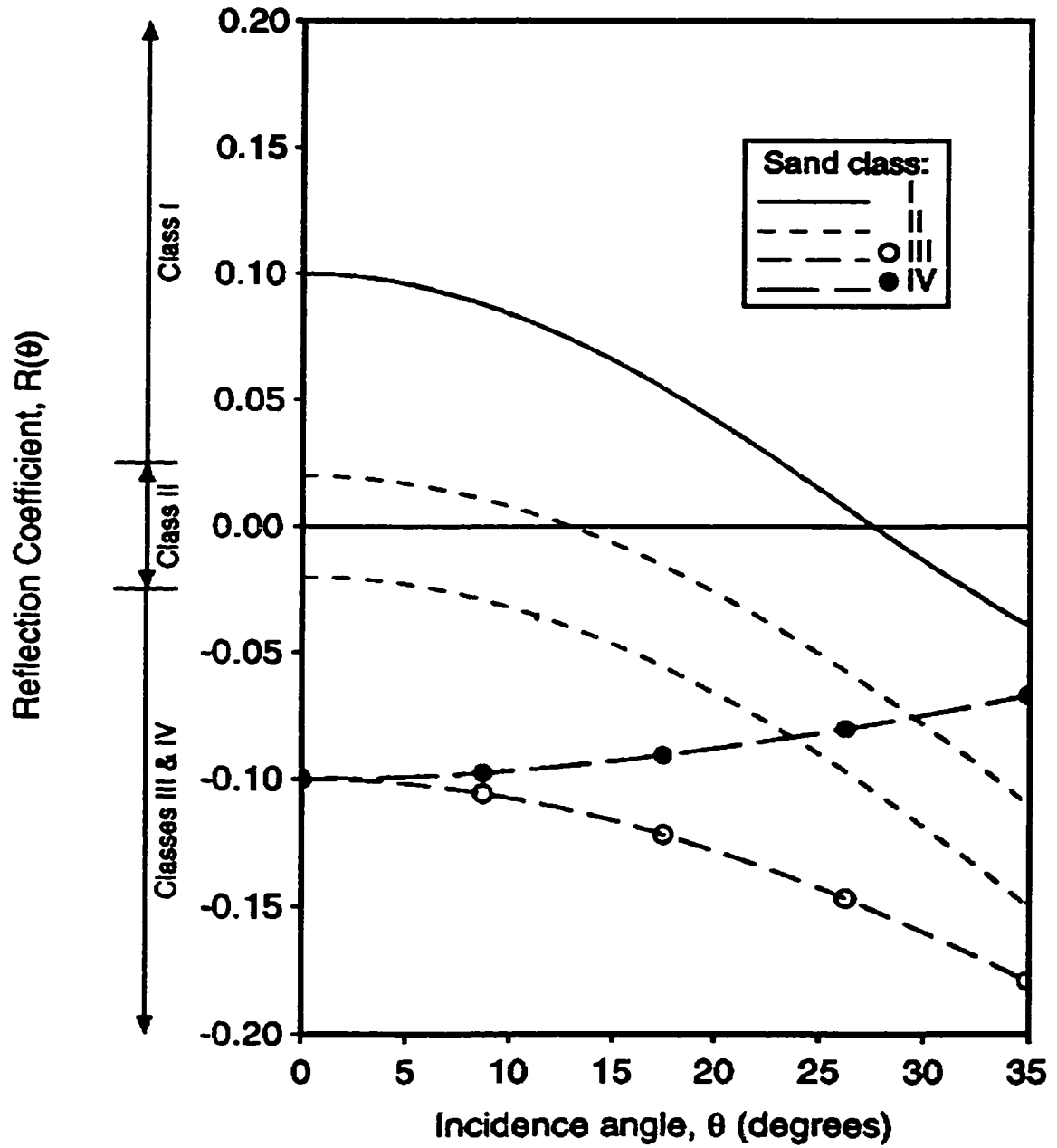


Figure 3.1. Plane-wave reflection coefficients at the top of each gas sand (Modified from Castagna et al., 1998).

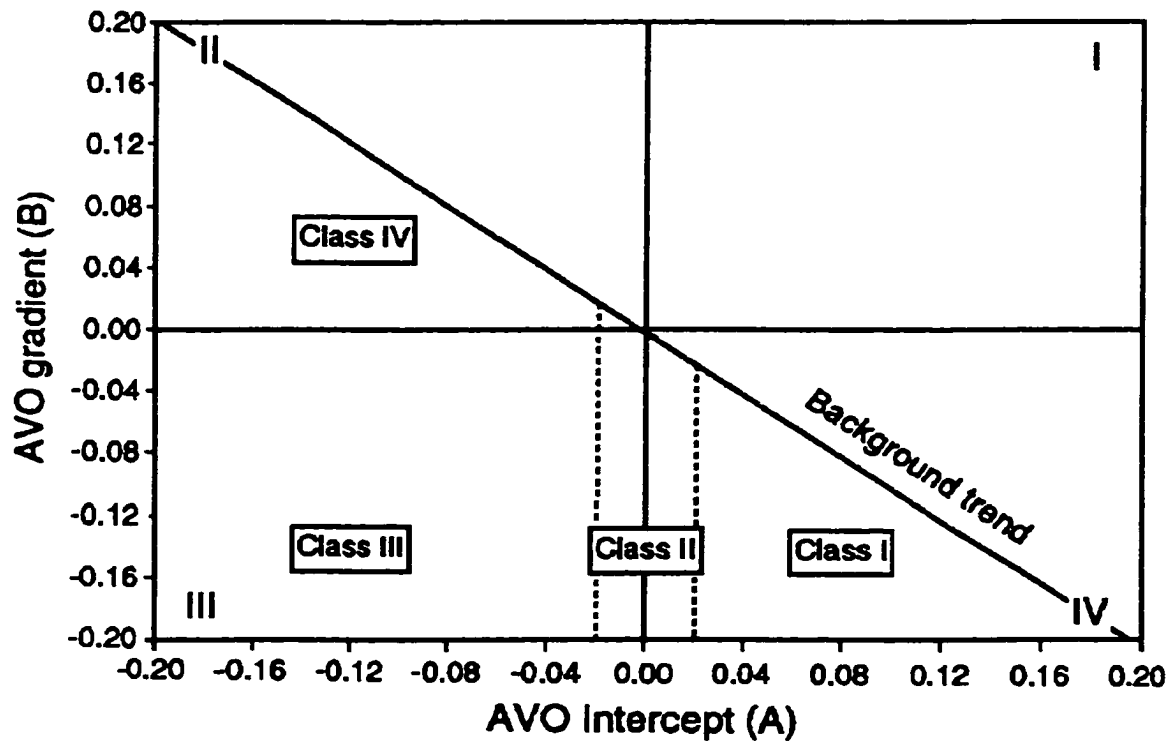


Figure 3.2. AVO intercept (A) versus gradient (B) crossplot showing four possible quadrants and the relative positions of the gas sand classes. The brine-saturated sandstones and shales tend to fall along a well-defined background trend (From Castagna et al. ,1998).

Chapter 4

AVO HODOGRAMS AND POLARIZATION ANGLE

In this chapter, the notion of AVO hodogram (Keho, 2000) is presented. In addition, the construction of the hodogram is discussed. Moreover, the parameters or attributes related to the hodogram are introduced. Such attributes are (1) the polarization angle and (2) the polarization angle difference.

4.1. AVO Hodograms

The AVO hodogram displays the terminus of a moving vector as a function of intercept (A), gradient (B), and time. Each sample of the data is shown on the hodogram as a plot point. Within a time window, the pre-stack seismic data (A and B traces) has a direction of maximum amplitude as well as a preferred orientation that exhibits a linear trend (Figure 4.1). In most cases, due to wave propagation and processing effects, the linear trend is distorted (Dong, 1998 and 1996). As a result, an elliptical trend is obtained.

From section 3.1, the intercept (A) and the gradient (B), extracted after a gradient analysis is performed on the CDP gathers, are derived from Shuey's approximation (Shuey, 1985) of the Zoeppritz's equations. That approximation provides a simple relationship between the P-wave reflection coefficients and the incidence angle:

$$R_{pp}(\theta) = A + B \sin^2 \theta + C \sin^2 \theta \tan^2 \theta \quad (4.1)$$

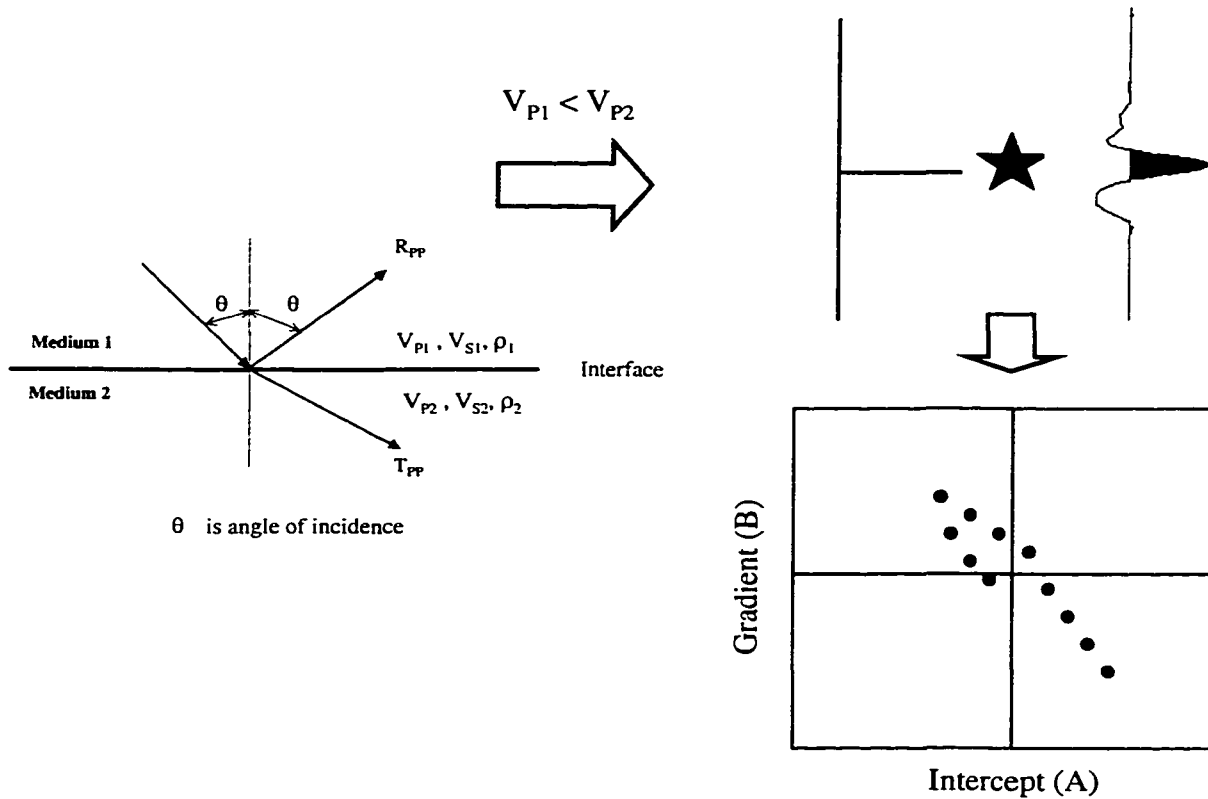


Figure 4.1. Schematic diagram of reflection at a boundary between two media. The reflectivity series is convolved with a wavelet and the resulting A and B traces are crossplotted. Note that the points are spread across all the quadrants to define a preferred orientation.

with

$$A = \frac{1}{2} \left(\frac{\Delta V_p}{V_p} + \frac{\Delta \rho}{\rho} \right) \quad (4.2)$$

$$B = \left(\frac{\Delta V_p}{2V_p} - 4 \frac{V_s^2}{V_p^2} \frac{\Delta V_s}{V_s} - 2 \frac{V_s^2}{V_p^2} \frac{\Delta \rho}{\rho} \right) \quad (4.3)$$

$$C = \frac{1}{2} \frac{\Delta V_p}{V_p} \quad (4.4)$$

where V_p , V_s , and ρ are the average values across the boundary for P-wave velocity, S-wave velocity, and density respectively.

4.2. AVO Hodogram Construction

The construction of the AVO hodogram is obtained by crossplotting the intercept (A) and the gradient (B) traces, or the near (N) and the far (F) traces. The near and far traces result from partial stacking of near or far offset or angle θ ranges, respectively.

The main advantage of the AVO hodogram is that it provides a preferred orientation of a seismic event in the A-B plane within a time window instead of a deviation or separation from any well-defined trend. Thus, an anomalous event embedded in a “background” trend (Figure 4.2) can show up as a large anomaly based on hodogram-derived attributes.

When the sample points from A and B traces or partial stacks are crossplotted, the preferred orientation corresponds to the “background” trend for non-anomalous events; whereas, the polarization at angles different from the “background” trend may be considered as anomalous AVO responses.

Some equations and principles related to AVO hodograms are determined by analogy from three-component VSP (vertical seismic profile) data analyses (DiSiena et al., 1981; and Esmersoy, 1984).

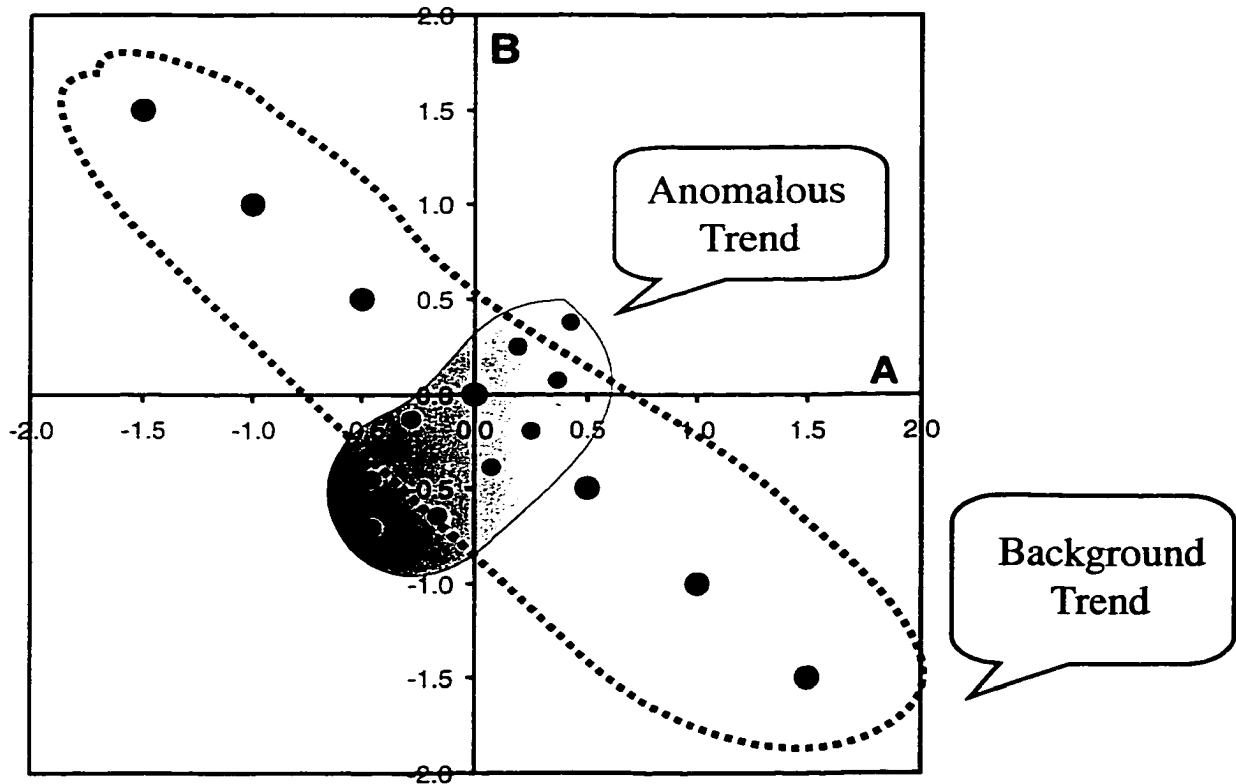


Figure 4.2. Intercept-Gradient crossplot showing an anomalous trend that is embedded in a background trend.

4.3. Polarization Angle

The polarization characteristics of a seismic event change in time. Therefore, the angle of polarization is characterized by the preferred orientation within a time window for a given time sample point (Figure 4.3). The polarization angle can be determined by eigenvector analysis as suggested by Keho (2000) for AVO hodograms and Esmersoy (1984) for polarization analysis of three-component VSP. The formulation is derived from the correlation matrix R_m that is used to compute the eigenvectors (Esmersoy, 1984):

$$R_m = \frac{1}{2N+1} \sum_{i=-N}^N r(i)r^T(i) \quad (4.5)$$

where N is half of the length of the time window (in sample points) and $r(i)$ represents the observed data in the time window of interest. The subscript m is the center sample point of the time window $[-N, N]$.

The matrix R_m from Equation 4.5 can be expanded in the A-B plane as:

$$R_m = \frac{1}{2N+1} \begin{pmatrix} \sum_{i=-N}^N A_{t+i}^2 & \sum_{i=-N}^N A_{t+i} B_{t+i} \\ \sum_{i=-N}^N A_{t+i} B_{t+i} & \sum_{i=-N}^N B_{t+i}^2 \end{pmatrix} \quad (4.6)$$

where

A_{t+i} is the AVO intercept value at time sample t ,
 B_{t+i} is the AVO gradient value at time sample t .

R_m is a 2 x 2 symmetric matrix and its eigenanalysis can be done efficiently.

The eigenvalues are obtained by solving the equation

$$|R_m - \lambda I| = 0 \quad (4.7)$$

where λ represents the eigenvalues or characteristic roots and I is the unity matrix:

$$I = \begin{pmatrix} 1 & 0 \\ 0 & 1 \end{pmatrix} \quad (4.8)$$

The eigenvectors corresponding to the characteristic roots (λ) are found. The two vectors are orthogonal and the components of one of the vectors (see Appendix B) are:

$$\begin{pmatrix} P_x \\ P_y \end{pmatrix} = \begin{pmatrix} \frac{\sqrt{2}}{[1+D]^{\frac{1}{2}}} \frac{\sum_i A_{t+i} B_{t+i}}{\sqrt{4\left(\sum_i A_{t+i} B_{t+i}\right)^2 + \left(\sum_i A_{t+i}^2 - \sum_i B_{t+i}^2\right)^2}} \\ \frac{\sqrt{2}}{2} [1+D]^{\frac{1}{2}} \end{pmatrix} \quad (4.9)$$

where

$$D = \frac{\left(\sum_i A_{t+i}^2 - \sum_i B_{t+i}^2 \right)}{\sqrt{4 \left(\sum_i A_{t+i} B_{t+i} \right)^2 + \left(\sum_i A_{t+i}^2 - \sum_i B_{t+i}^2 \right)^2}} \quad (4.10)$$

with $i = -N, \dots, N$

The polarization angle, ϕ , is determined within a sliding time window in which all the computations are done. The size of the time window can be from one-half to a wave period (Keho, 2000). For any given window, the angle of polarization at a time sample is:

$$\phi = \tan^{-1} \left(\frac{P_y}{P_x} \right) \quad (4.11)$$

where

P_x and P_y are the components of the eigenvector (see Equation 4.9).

The values of the polarization angle range from -90 degrees to $+90$ degrees.

4.4 Polarization Angle Difference

The polarization angle difference ($\Delta\phi$) is directly related to the angle of polarization. It is the difference between the polarization angle and the ‘background’ angle or trend angle:

$$\Delta\phi = \phi - \phi_{trend} \quad (4.12)$$

where

ϕ is the polarization angle

ϕ_{trend} is the background polarization angle.

The background polarization angle or trend angle is computed from a larger time window that can be several hundred milliseconds long. We should note that as the V_P/V_S ratio decreases with depth (or two-way time) and as wave propagation effects accumulate or the signal-to-noise ratio varies, the background trend could change (Castagna et al., 1998). By analogy, we could have small variation of the background angle.

The polarization angle difference attribute could magnify any anomaly, thus enhancing any seismic amplitude anomaly. The attribute values can vary from -180 degrees to $+180$ degrees.

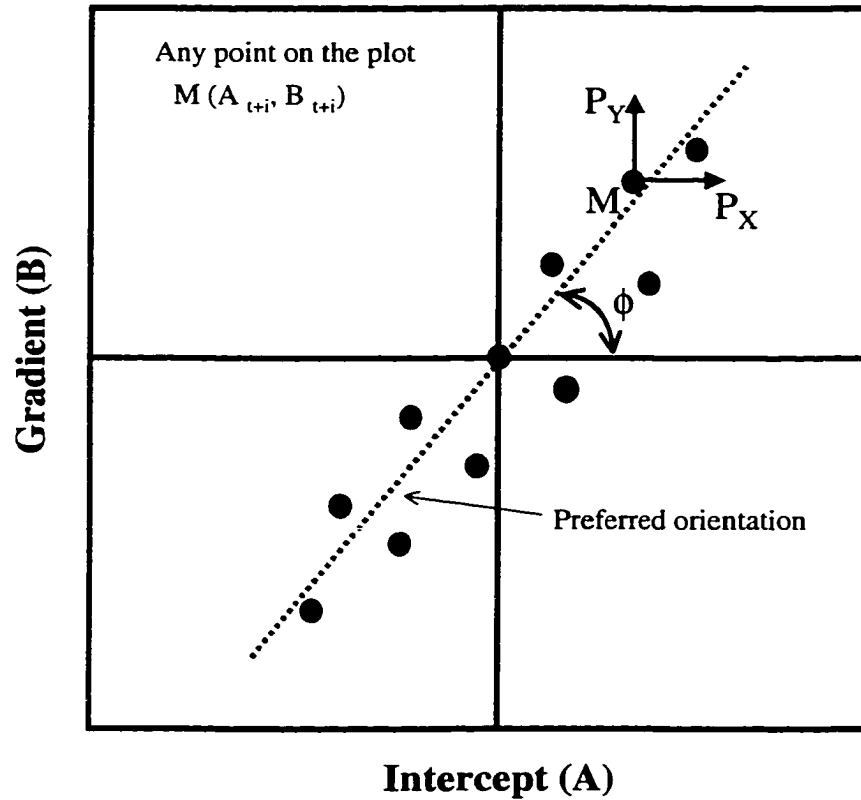


Figure 4.3. Angle of polarization definition. ϕ is measured counter-clockwise from the point and the horizontal axis. At any point M on the hodogram, a unit polarization vector $P (P_X, P_Y)$ can be computed. The polarization direction is the preferred orientation in the time window $[-N, N]$.

Chapter 5

POLARIZATION ATTRIBUTES

In this Chapter, the other polarization attributes are introduced. These attributes are the AVO strength, the product of strength and polarization angle difference, and the linear-correlation coefficient. The methodology used for the computation of the attributes is presented.

These attributes are used in conjunction with the polarization angle to characterize the seismic trace events.

5.1 The AVO Strength

The strength is the measure of the distance of the hodogram points from the origin within the time window of the analysis. The sample points, from the intercept (A) and the gradient (B) traces, on the plot can be considered as a cloud of points of a certain length (Figure 5.1). The strength, L , is defined as:

$$L = L_{\min} + L_{\max} \quad (5.1)$$

with

$$L_{\min} = \sqrt{A_{\min}^2 + B_{\min}^2} \quad (5.2)$$

and

$$L_{\max} = \sqrt{A_{\max}^2 + B_{\max}^2} \quad (5.3)$$

where

A_{\min} is the minimum value within the time window of the analysis of A and B_{\min} is the corresponding B at A_{\min} .

A_{\max} is the maximum value within the time window of the analysis of A and B_{\max} is the corresponding B at A_{\max} .

Where there is no data, $L = 0$. For weak seismic events with small values of AVO gradient, the value is very small. The stronger the event with large gradient value, the larger L is.

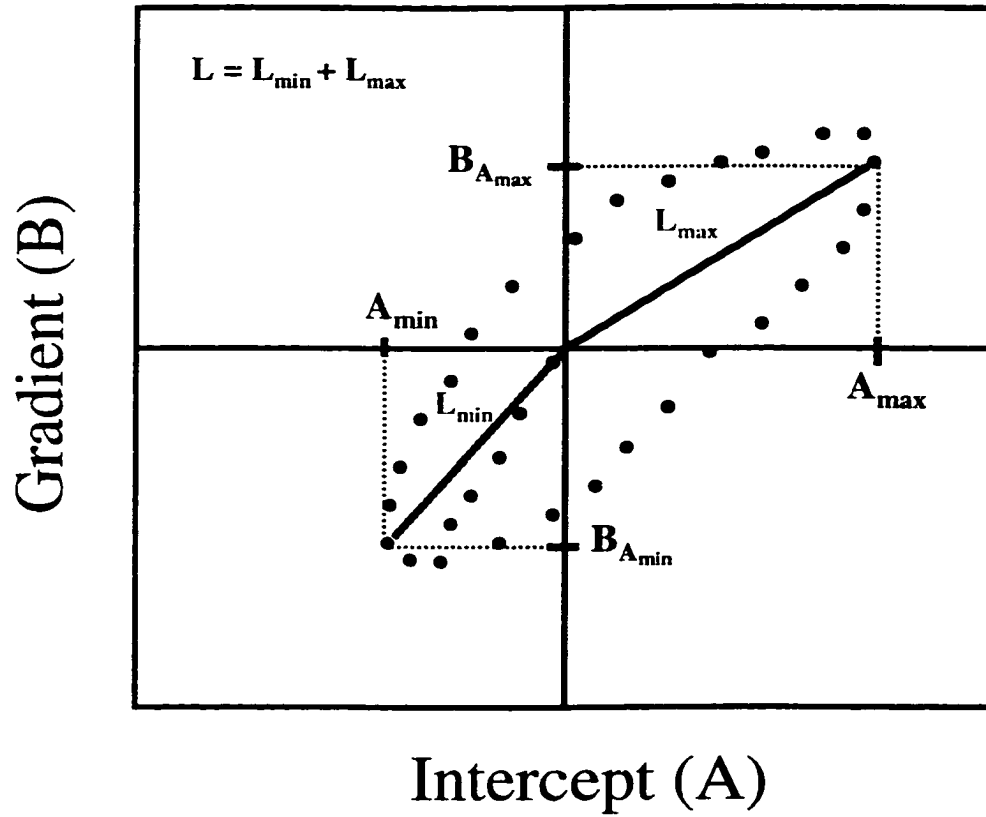


Figure 5.1. Definition of the strength attribute, L , as is related to the minimum and maximum values of the intercept (A) and gradient (B).

5.2 The Linear-Correlation Coefficient

The linear-correlation coefficient of the polarization analysis is the measure of the scattering of the hodogram data points within the time window as depicted in Figure 5.2.

The linear-correlation coefficient, r , is defined as (Rawlings et al., 1998):

$$r^2 = \frac{(Cov(A_{t+i}, B_{t+i}))^2}{Var(A_{t+i}) * Var(B_{t+i})} \quad (5.4)$$

where Cov and Var are the covariance and the variance, respectively.

By expanding Equation 5.4, the linear-correlation coefficient expression becomes (Bevington, 1969):

$$r^2 = \frac{\left(n \sum_i A_{t+i} B_{t+i} - \sum_i A_{t+i} \sum_i B_{t+i} \right)^2}{\left(n \sum_i A_{t+i}^2 - \left(\sum_i A_{t+i} \right)^2 \right) \left(n \sum_i B_{t+i}^2 - \left(\sum_i B_{t+i} \right)^2 \right)} \quad (5.5)$$

where

n is the number of sample points within the time window.

In our context we remove the sign of r by using r^2 . Then values of r range from 0, when there is very high scattering of hodogram points, to 1, when there is no scattering of hodogram points about the polarization trend within the analysis window.

5.3 The Product of AVO Strength and Polarization Angle Difference

The product of AVO strength and polarization angle difference, also called the polarization product, is the measure of the magnitude of the AVO effect along the trace. Large seismic amplitude anomalies will exhibit large values, whereas small values will be related to non-anomalous events. This attribute, $L\Delta\phi$, can be used to identify AVO anomalies of significant magnitude within a given time window.

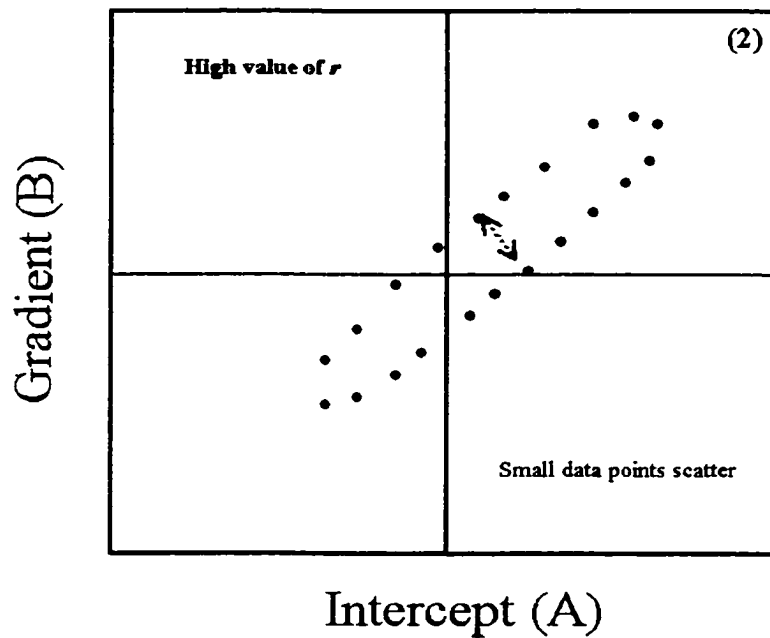
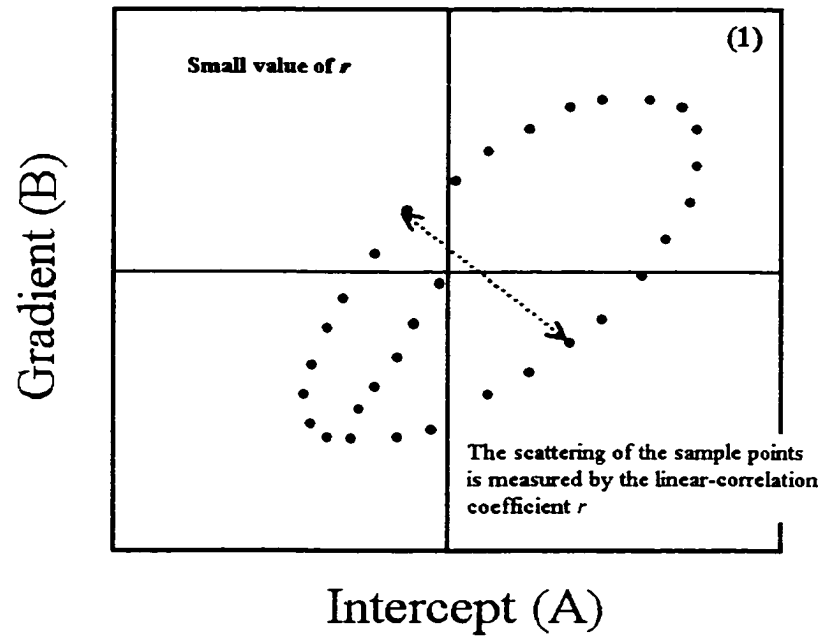


Figure 5.2. Linear-correlation coefficient attribute (r) and sample points scattering. (1) Small values of r are related to high scattering of data points within the analysis window. (2) High values of r correspond to small scattering of data points.

Chapter 6

MODELING EXAMPLES

An important parameter of the polarization attributes is the time window size for the computation. The window size is tested on a synthetic data generated from a flat-layered model. Different windows are used and the related polarization attributes are computed. Moreover, the wave propagation and processing effects on polarization attributes are simulated by considering (1) phase shift, (2) loss of frequency bandwidth, and (3) superposition of the previous two effects between the near-offset or intercept traces and far-offset or gradient traces. In addition, the polarization attributes are calculated for a thin-layered model, a model with layers below tuning thickness.

6.1. Model

A flat-layered model, made of a succession of gas- and water-saturated sand units encased in shale or silt units, is shown in Figure 6.1. Overall, the layer thickness of the sand intervals is chosen so that seismic temporal (vertical) resolution is satisfied. That is, the thickness is greater than the approximate tuning thickness (Z_{tuning}):

$$Z_{tuning} = \frac{V_{int}}{4f_d} \quad (6.1)$$

where

V_{int} is the interval velocity of the layer
 f_d is the dominant frequency of the seismic data

The B Sand, C Sand, I Sand, and M Sand are the gas sands. The D Sand, G1 Sand, and L sand are water-saturated sands. The G Sand is tight gas sand. The model elastic parameters, compiled from well log data from the Gorgon field, NW Shelf of Australia, are presented in Table 6.1.

Table 6.1. Elastic parameters of the flat-layered model.

Layer	Name	Thickness (ft)	V _P (m/s)	V _S (m/s)	ρ (g/cc)	Poisson's ratio
1	Barrow Group	1000	3640	2000	2.45	0.33
2	B	300	3530	2390	2.27	0.10
3	Shale/Silt	200	3610	2040	2.42	0.30
4	C	200	3625	2235	2.35	0.10
5	Shale/Silt	200	3450	1900	2.30	0.31
6	D	200	3915	2540	2.40	0.25
7	Shale/Silt	200	3615	2025	2.49	0.30
8	G	250	3985	2435	2.45	0.20
9	Shale/Silt	175	3755	2020	2.47	0.30
10	G1	250	3830	2425	2.37	0.20
11	Shale/Silt	200	3740	2125	2.45	0.30
12	I	300	3550	2415	2.33	0.10
13	Silt	200	3960	2080	2.45	0.30
14	L	200	4140	2555	2.43	0.20
15	Shale/Silt	200	3995	2140	2.40	0.28
16	M	300	3830	2540	2.33	0.10
17	Shale/Silt	350	4320	2460	2.50	0.30

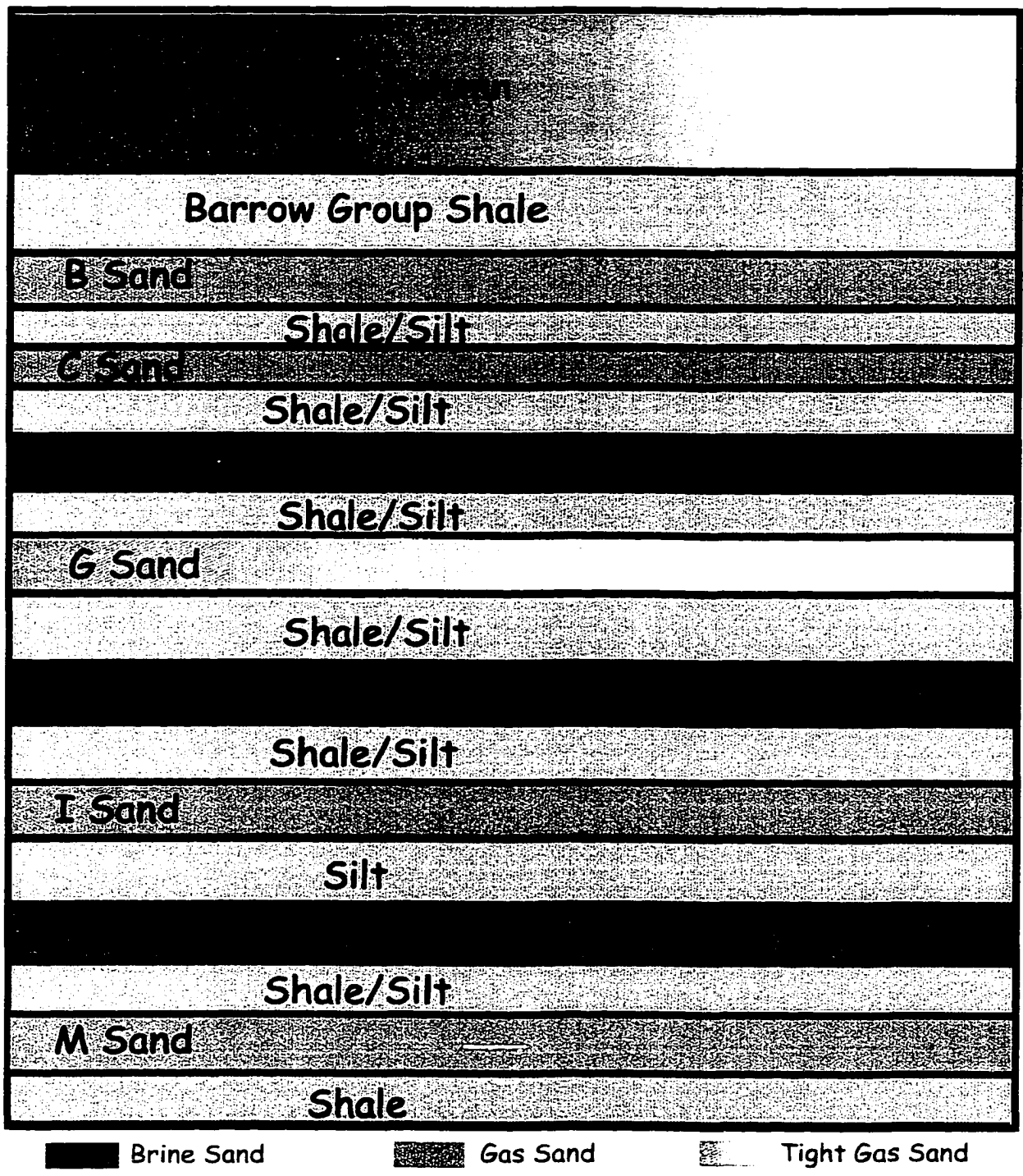


Figure 6.1. Schematic diagram of the flat-layered model used for synthetic gather generation. The vertical scale has been exaggerated.

A synthetic gather, shown in Figure 6.2, is generated using a full elastic wave algorithm of the AVO Modeling module of the AVO Hampson-Russell Software. A zero-phase Ricker wavelet, with a dominant frequency (f_d) of 40 Hz and a length of 200 ms is used. The range of offsets modeled varies from 0 to 16,405 ft.

A gradient analysis is performed to extract the intercept (A) and the gradient (B) traces of a fitted line relating seismic amplitudes of the synthetic gather to $\sin^2(\theta)$ as defined in Equation 3.1. The angle range considered for the analysis is from 2 to 32 degrees. This angle restriction is important as it helps improve the gradient extraction. The resulting intercept and gradient traces are depicted in Figure 6.3.

6.2. Window Size Analysis

The size of the time window is very important in computing the polarization attributes. There is an optimum size that gives a good temporal resolution of seismic events. For a given preferred orientation or polarization direction, the magnitude of the attribute will have the maximum value. The polarization attributes resulting from very small windows are noisy, whereas attributes from very large windows do not represent temporally the seismic reflections. The size of the time window should be one-half to a wave period for the polarization angle computation (Keho, 2000).

Four window sizes 10 ms, 20 ms, 50 ms, and 200 ms are used to compute the polarization attributes from the synthetic data of the flat-layered model. The comparison between the analysis window size and the seismic wave period is presented in Table 6.2. The wave period of the synthetic seismic data is 25 ms, since the dominant frequency of the data is 40 Hz.

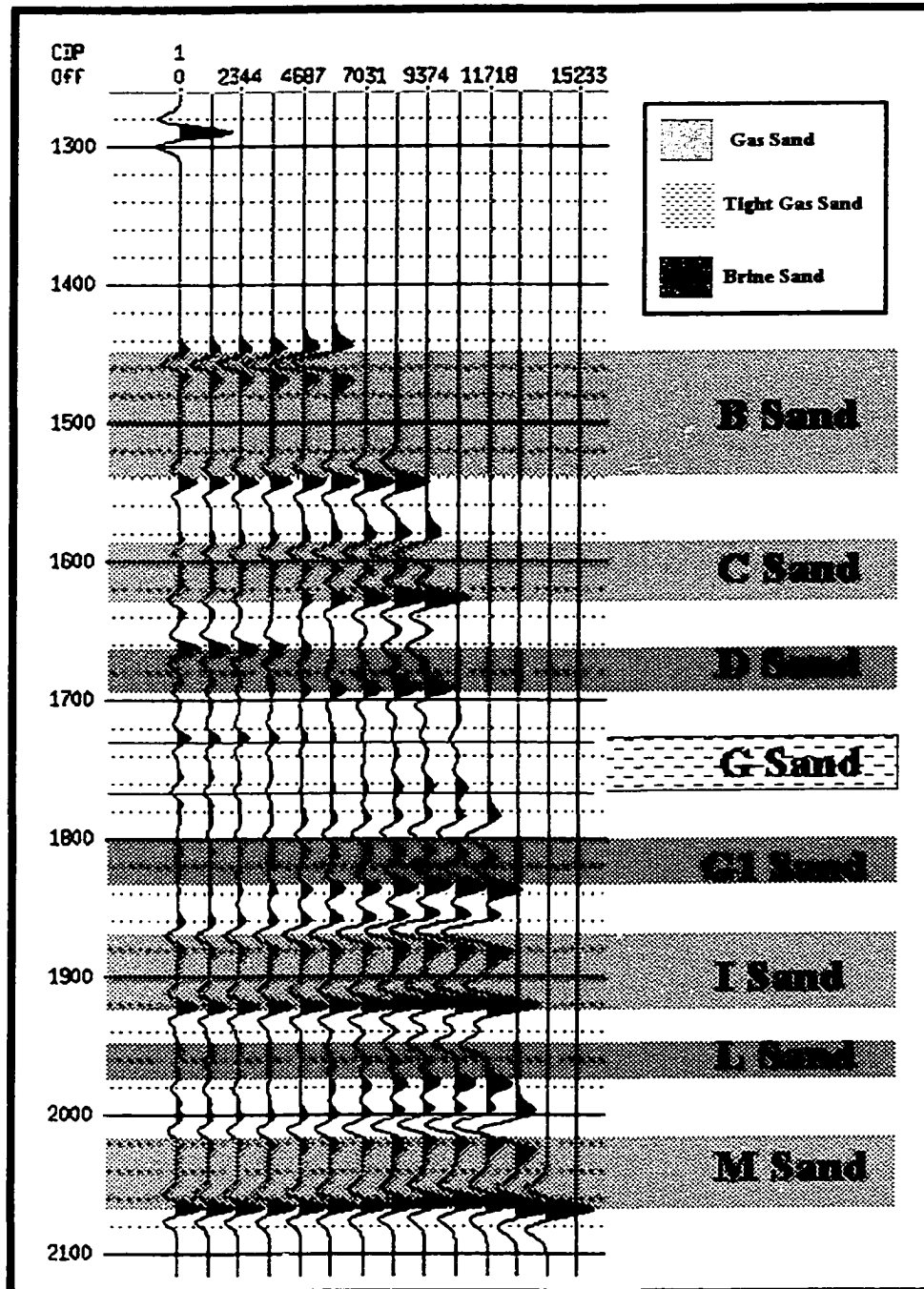


Figure 6.2. Synthetic NMO-corrected CDP gather generated from the flat-layered model. A 40 Hz Ricker wavelet is used for the modeling. The color overlay represents the two-way time calculated from Table 6.1.

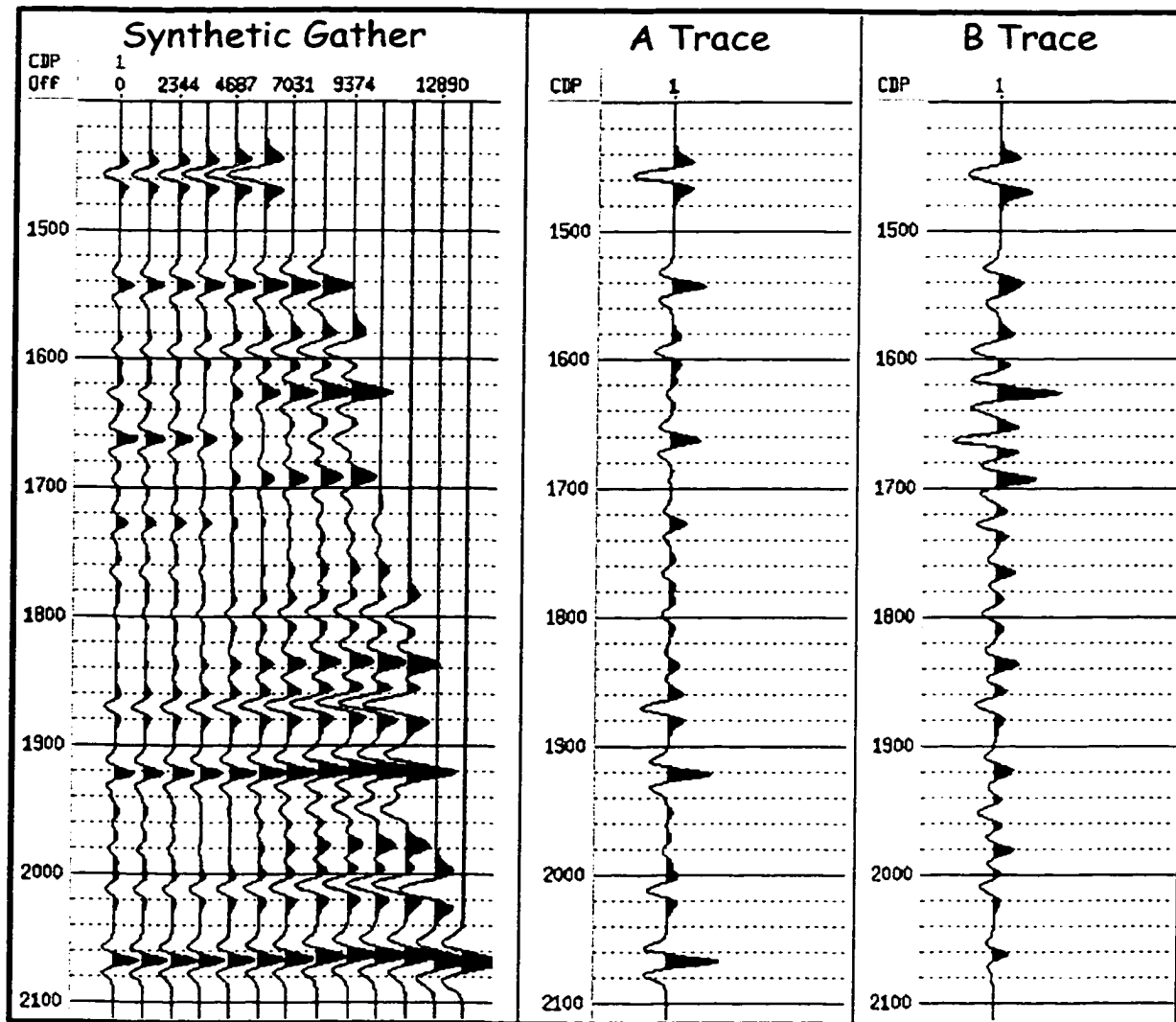


Figure 6.3. Extracted intercept (A) and gradient (B) traces along with the synthetic CDP gather. The first event shown around 1450 ms is the top of B Sand reflection.

From the polarization angle and the strength displays, the optimum window size is 20 ms that is comprised between 12.5 ms and 25 ms (the seismic wave period), as depicted in Figures 6.4 – 6.5. The linear-correlation coefficient is representative of the data temporally for window size of 20 ms and 50 ms (Figure 6.6). Polarization attributes computed from large analysis windows, a 200 ms-window for example, do not resolve temporally the seismic reflections. However, attributes from the 50 ms window still show the events with less resolution.

Representative hodograms of events corresponding to the top of B Sand, D Sand, G1 Sand, and I Sand are shown in Figure 6.7.

Table 6.2. Time equivalence between the window size and the wave period. The period (T) of the seismic data is 25 ms.

Window Size in ms	Equivalence to Wave Period (T)
10	$\frac{2}{5}T = 0.4T$
20	$\frac{4}{5}T = 0.8T$
50	2T
200	8T

It is crucial to choose an optimum window size prior to extracting a polarization attribute for a good and realistic representation of the seismic data. Table 6.3 shows the

optimum window size that highlights well the seismic events of the synthetic data. Note that the recommended window size for the polarization angle can be different from that of the linear-correlation coefficient.

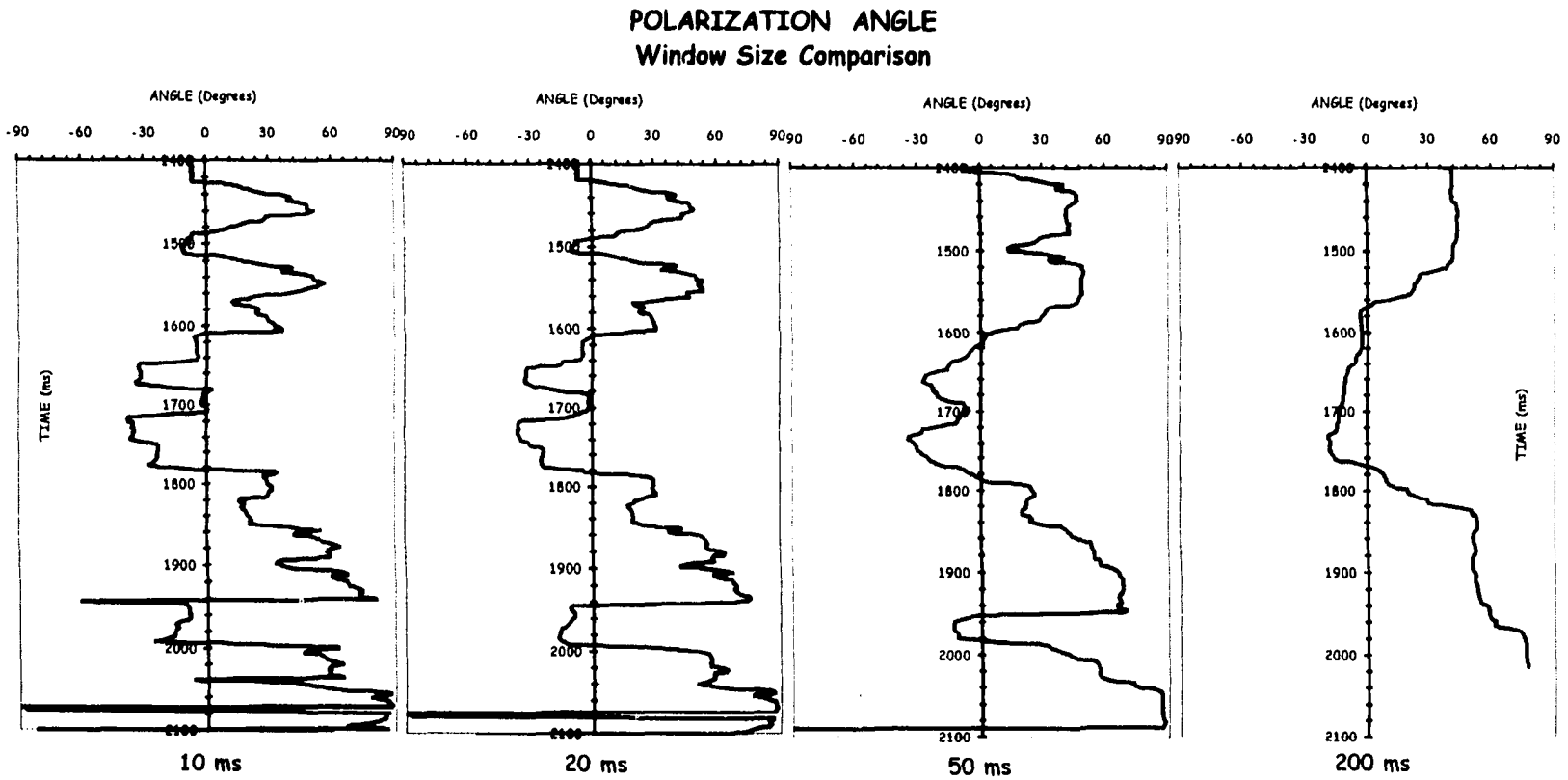


Figure 6.4a. Display of the synthetic gather polarization angle for different analysis window sizes: 10 ms, 20 ms, 50 ms, and 200 ms.

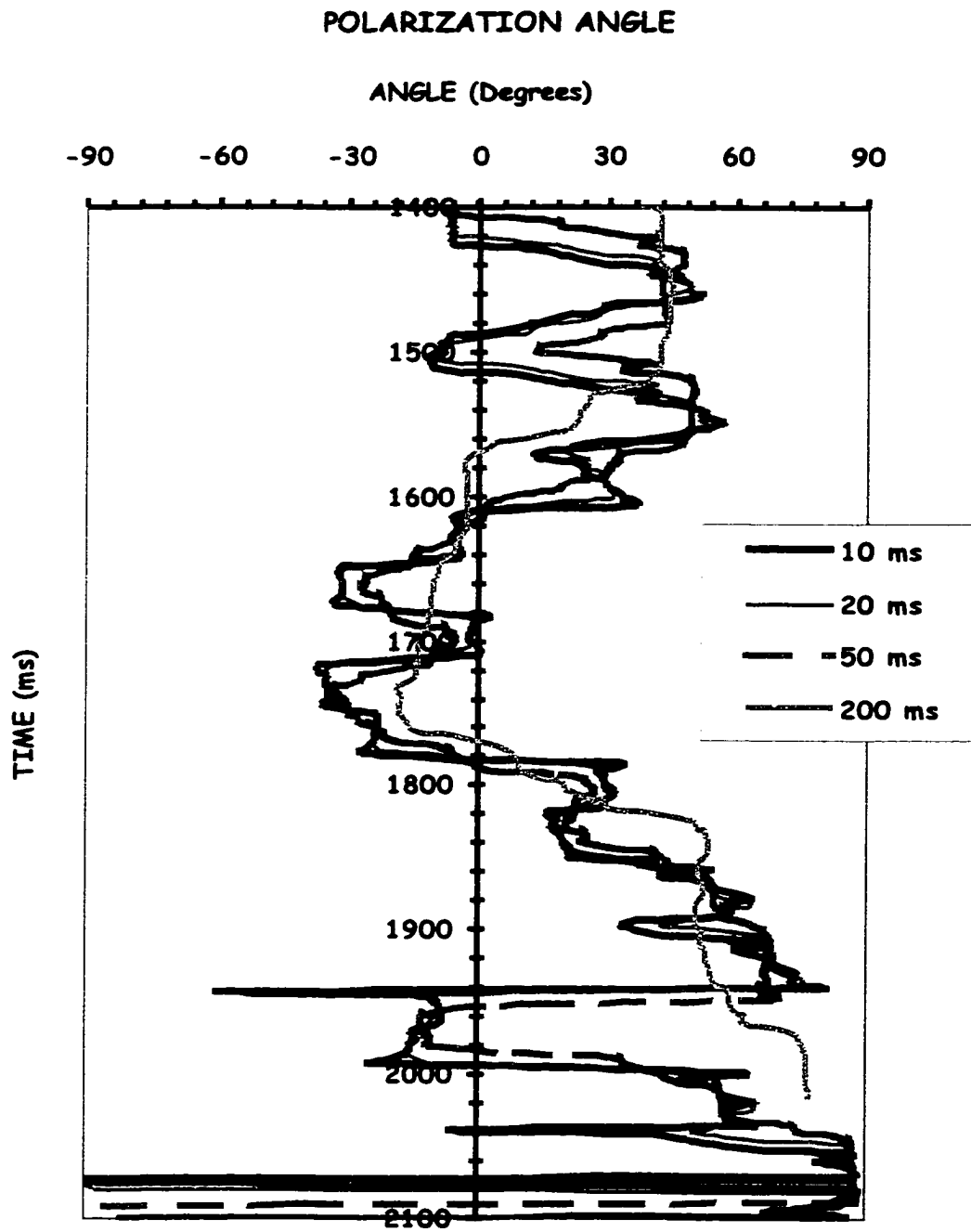


Figure 6.4b. Overlay of the synthetic gather polarization angle computed using different time window sizes: 10 ms, 20 ms, 50 ms, and 200 ms. The optimum window size that gives the best representation of the seismic data is 20 ms.

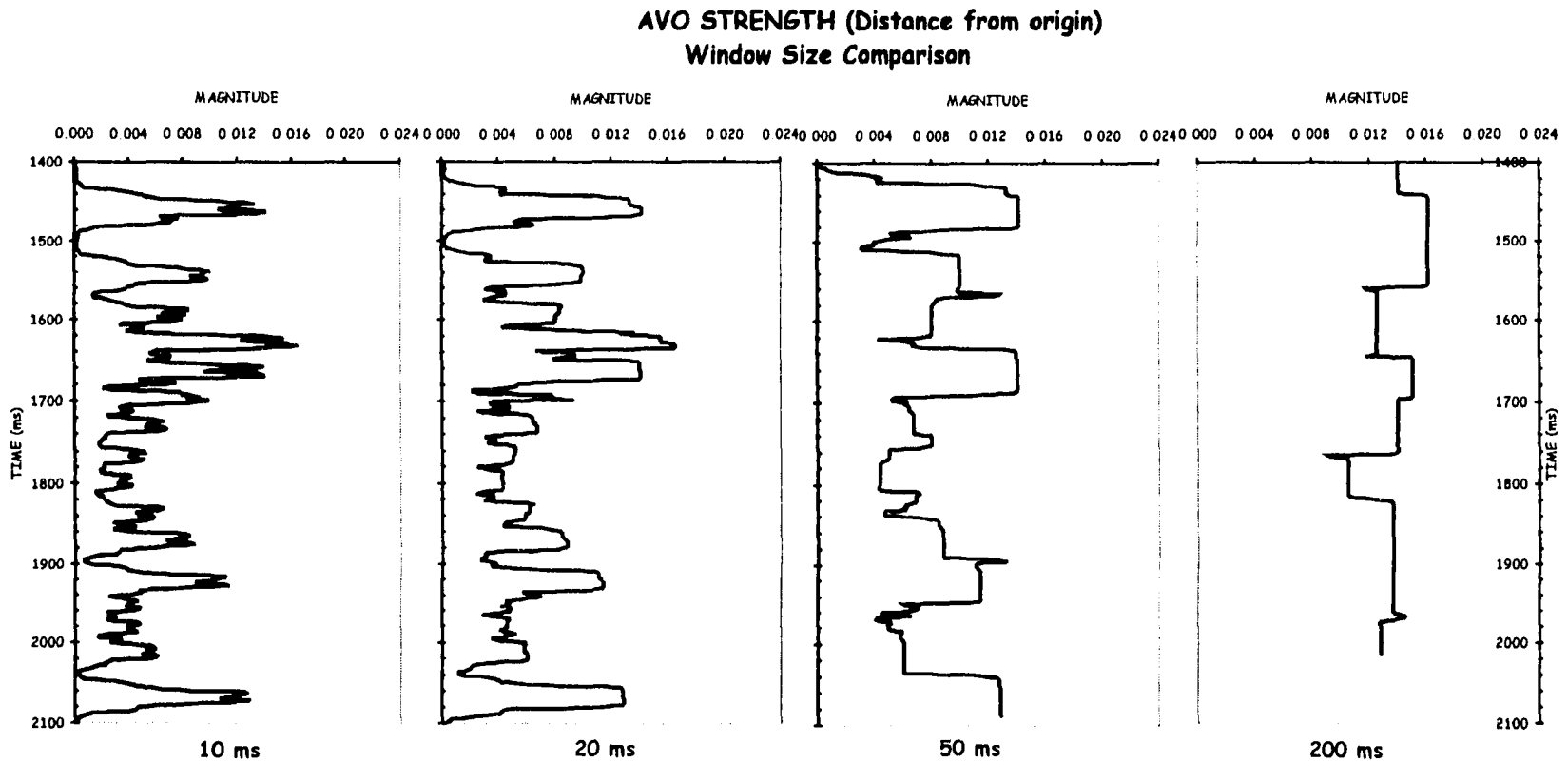


Figure 6.5a. Display of the synthetic gather AVO strength for different analysis window sizes: 10 ms, 20 ms, 50 ms, and 200 ms.

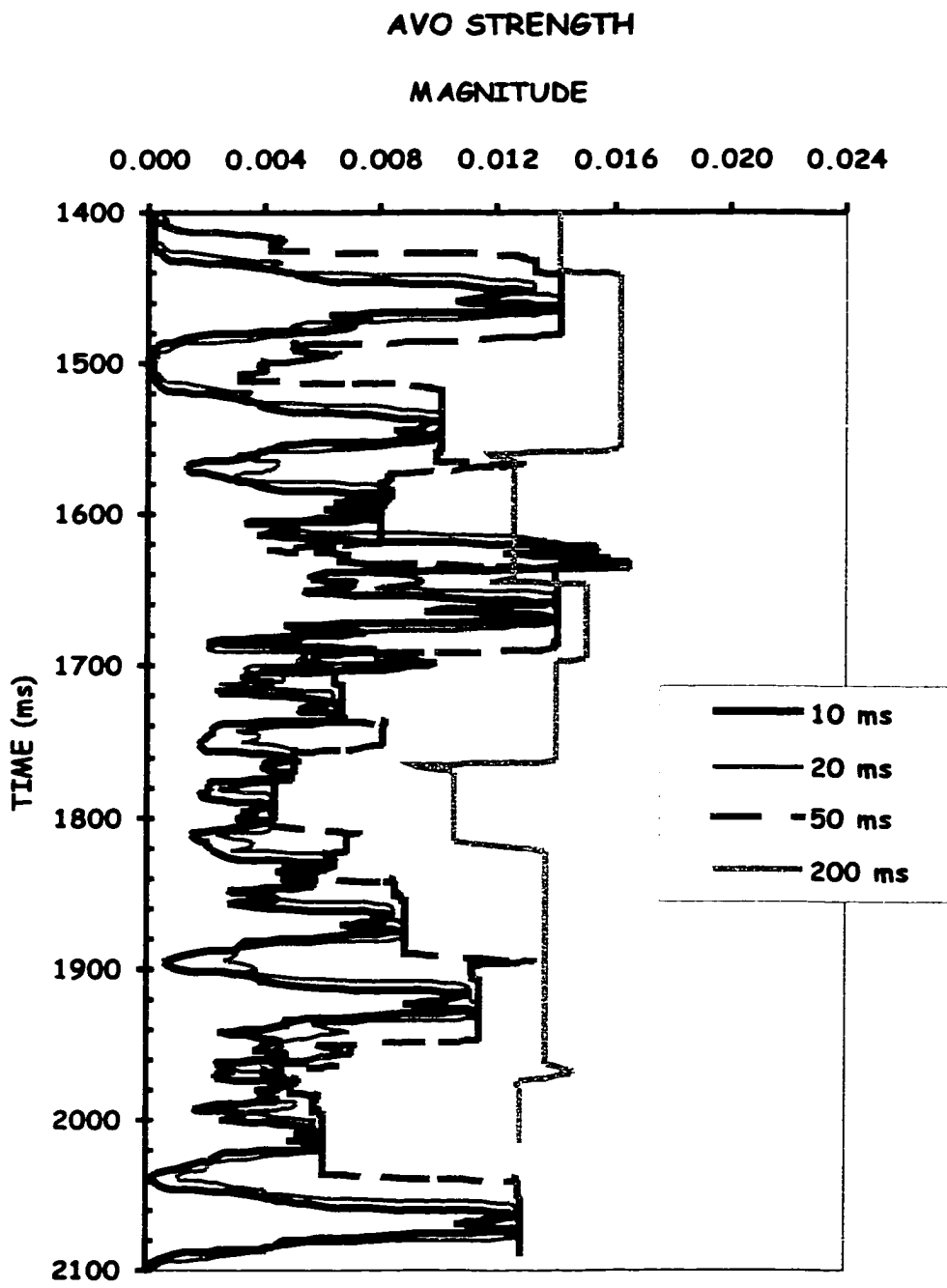


Figure 6.5b. Overlay of the synthetic gather AVO strength attribute computed using different time window sizes: 10 ms, 20 ms, 50 ms, and 200 ms. The window size that gives the best representation of the seismic data is 20 ms.

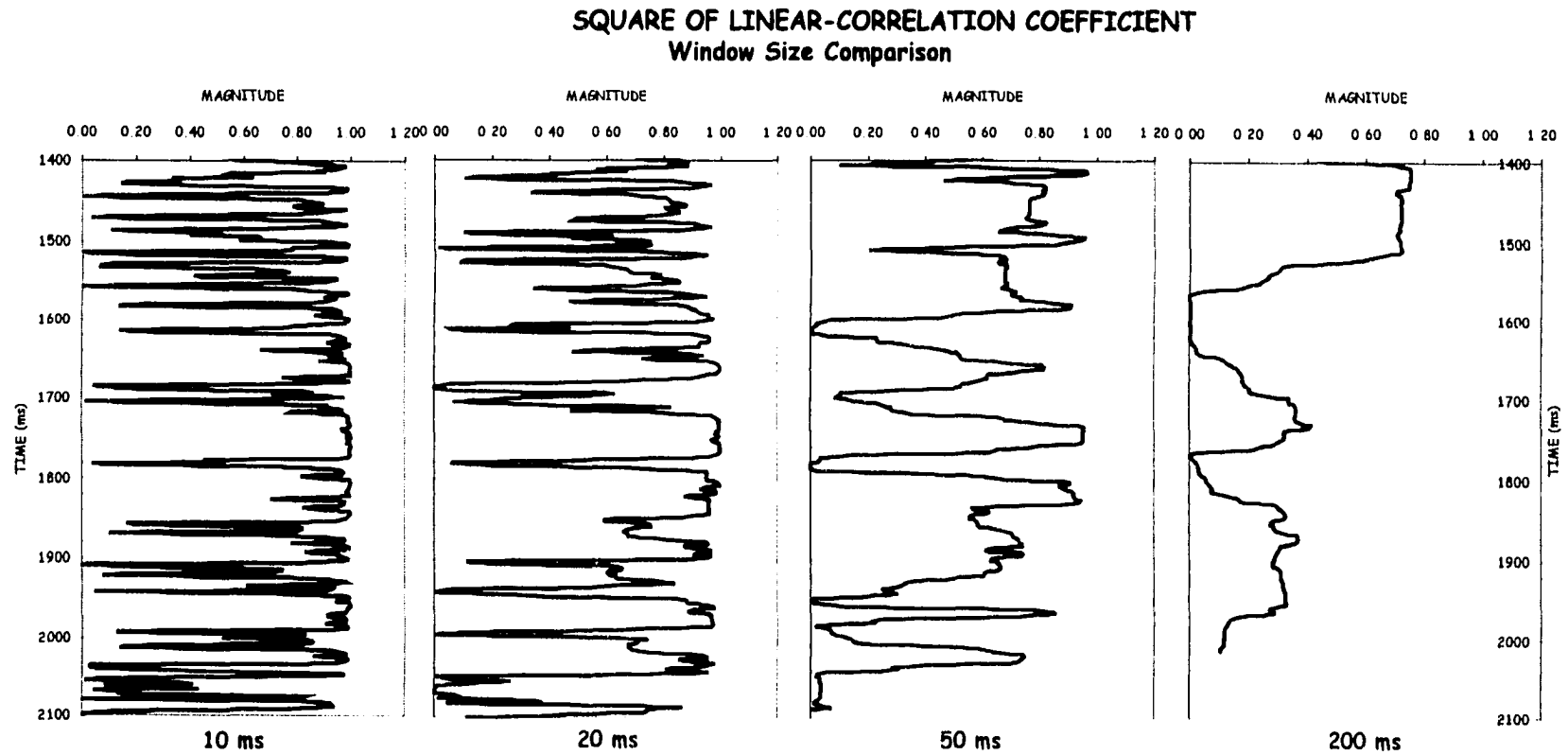


Figure 6.6a. Display of the synthetic gather squared linear-correlation coefficient attribute for different analysis window sizes: 10 ms, 20 ms, 50 ms, and 200 ms.

SQUARE OF LINEAR-CORRELATION COEFFICIENT

MAGNITUDE

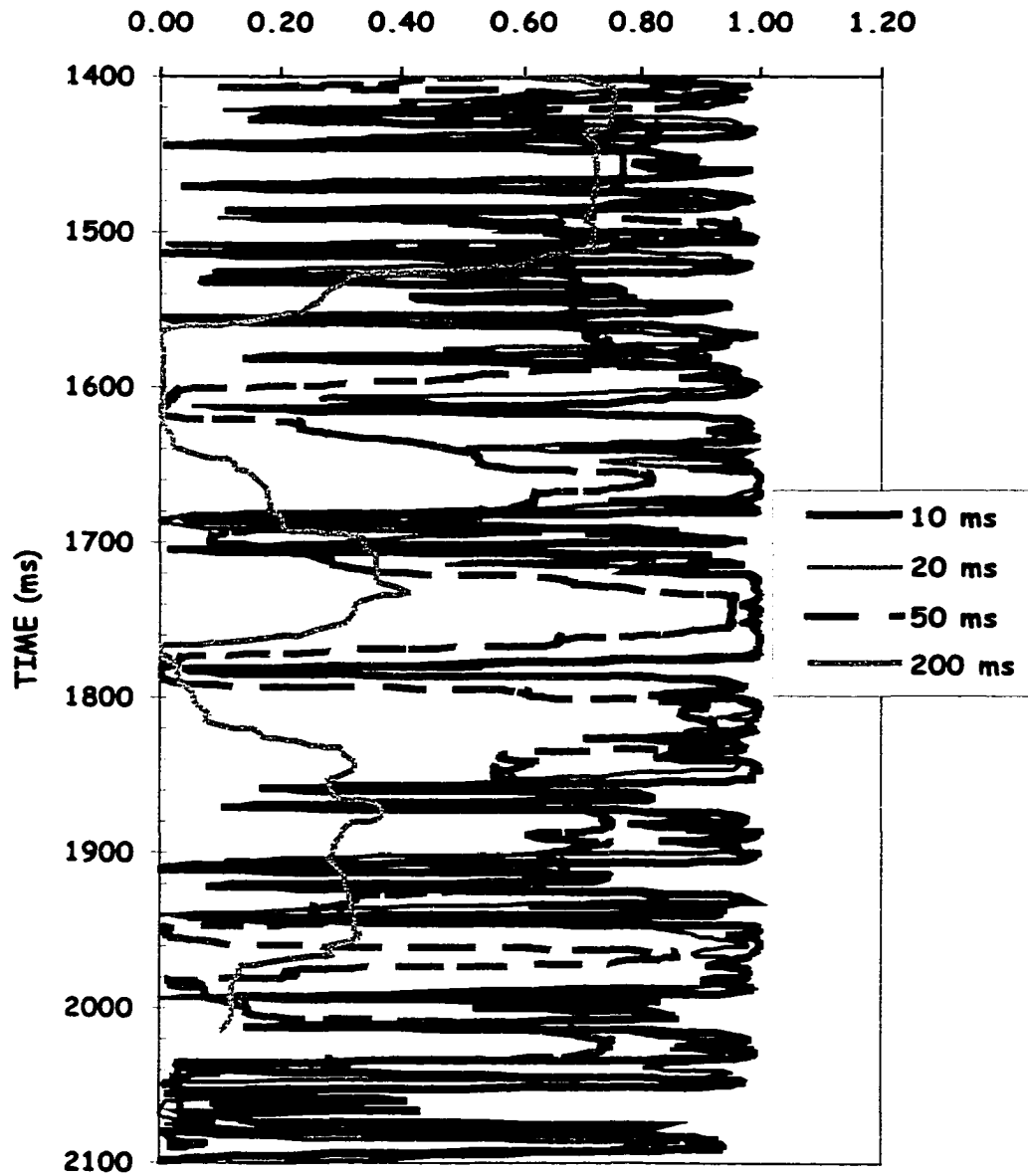


Figure 6.6b. Overlay of the synthetic gather square of linear-correlation coefficient attribute computed using different time window sizes: 10 ms, 20 ms, 50 ms, and 200 ms. The optimum window size is 50 ms.

AVO HODOGRAM OF THE TOP EVENT FOR B SAND, D SAND, G1 SAND, and I SAND

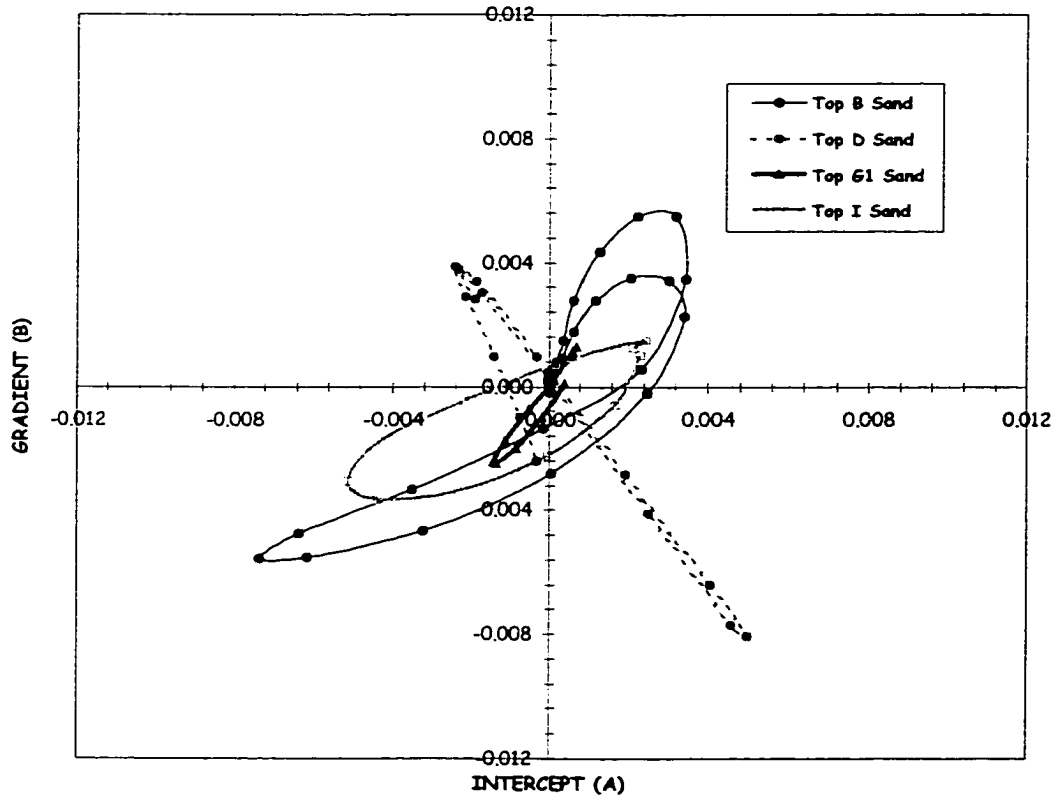


Figure 6.7. AVO hodogram of the event for the top of B Sand, D Sand, G1 Sand, and I Sand. B Sand and I Sand are gas sands; whereas, D Sand and G1 Sand are brine sands.

Table 6.3. Optimum window size for the computation of polarization attributes of the synthetic data.

Polarization Attributes	Optimum Window Size in ms
Polarization angle / Angle difference	20
Strength	20
Linear-correlation coefficient	50

6.3. Wave Propagation and Processing Effects on Polarization Attributes

The theory of AVO is based on reflection coefficient quantification; however in practice, AVO analysis is performed from seismic amplitude measurements as opposed to direct measurements of reflection coefficients. The aim of seismic processing is to correct for a numbers of factors which affect seismic amplitudes besides reflectivity changes such as geometrical spreading losses, transmission losses, intrabed multiples, source and receiver coupling, source and receiver arrays, tuning, instrument noise, and Fresnel zone aperture.

For a seismic trace to be exactly equal to the reflectivity series, the following conditions must be met: the source wavelet must be removed; noise cannot be present; all multiples must be removed; spherical spreading, transmission losses, and other scaling factors must be removed. It is clear that these requirements will never be completely achieved after seismic data processing. Some of the effects will be partially removed, some will not. A typical example of how the non-related reflectivity factors affect amplitude is the error caused in the inversion of stacked seismic traces to generate impedance profiles, as demonstrated by Cooke and Schneider (1983). On the other hand,

as a result of the different processing steps, artifacts can be present in the data. Such effects have been characterized for AVO intercept (A) and AVO gradient (B) by Dong (1996, 1998). When seismic data is plotted in an A-B plane, the linear trend representative of non-contaminated data is distorted. As a result, an elliptical trend is obtained.

Throughout this dissertation, intercept and gradient traces are extracted from seismic gathers, synthetic or real, that have been processed for relative amplitude recovery and preservation. Phase shift, loss frequency bandwidth, and the superposition of the previous two effects between the near-offset or intercept traces and far-offset or gradient traces are considered to simulate the above-mentioned processing artifacts (Figure 6.8).

The seismic reflection from a single interface is represented on the AVO hodogram by a very narrow cloud of sample points that has a well-defined preferred orientation (polarization) as shown in Figure 6.8a when the intercept and gradient traces have the same frequency content and there is no shift between the two traces. Due to processing effects, a cloud of points defining a seismic reflection becomes wider, increasing the scattering; thus making the polarization angle determination less reliable. The polarization attribute that exhibits well these effects is the linear-correlation coefficient, r .

The seismic event off the top of the B Sand layer, a trough at 1450 ms TWT on the synthetic gather, is used to illustrate the effect added to the far-offset traces or gradient trace of:

- (1) a 20-degree phase shift (Figure 6.8b),

- (2) a frequency bandwidth decrease, from 0-15-50-75 to 0-20-30-50 Hz (Figure 6.8c),
- (3) both a phase shift and a frequency bandwidth decrease (Figure 6.8d).

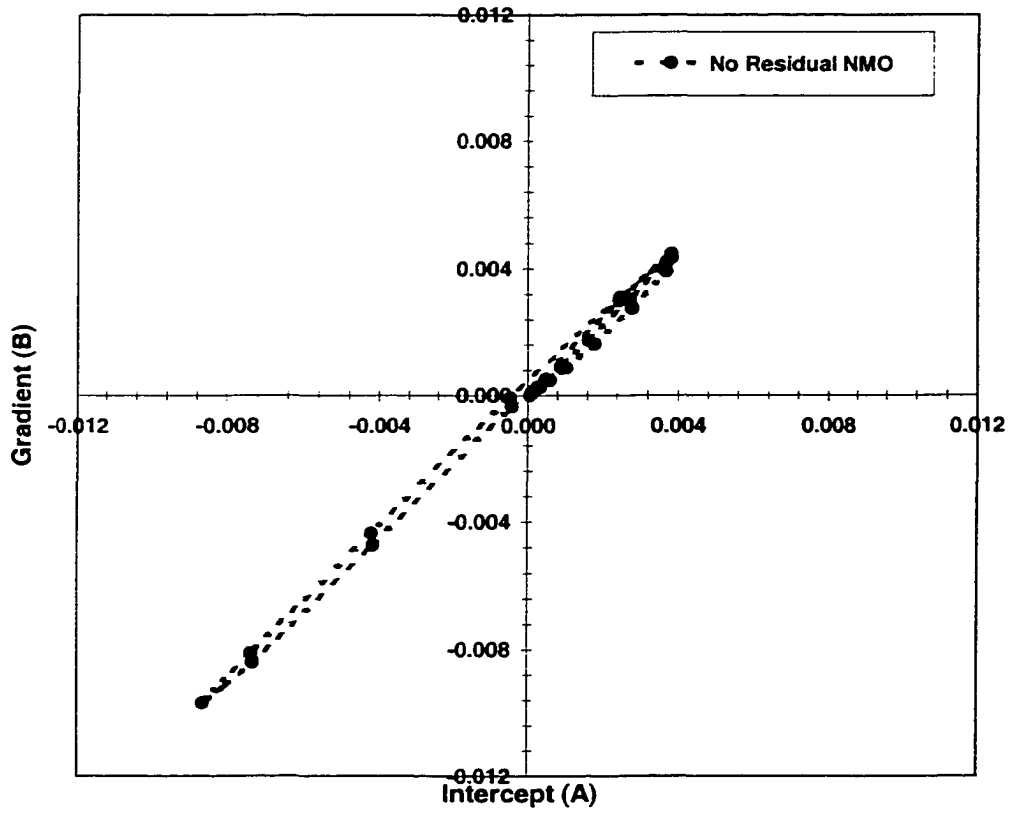
The computed polarization angle and the linear-correlation coefficient for the top B Sand reflection (1430 – 1480 ms TWT) are depicted in Figure 6.9, and their average values between 1430 and 1480 ms are presented in Table 6.4. It can be observed that the largest value of r , 0.99, corresponds to the no-processing artifacts (no residual NMO) case; whereas, the smallest value of r , 0.62, is obtained when the phase shift and the decrease of frequency bandwidth are combined. Note that the polarization angle is almost insensitive to NMO errors.

Table 6.4. Average values for the top B Sand event (1430 - 1480 ms) of the polarization angle and the linear-correlation coefficient.

Processing Effect	Polarization Angle ϕ (degrees)	Linear-Correlation Coefficient r	Figure 6.7
No residual NMO	47.3	0.99	(a)
20-degrees phase shift	47.2	0.89	(b)
Decrease of frequency bandwidth	52.9	0.67	(c)
Phase shift and bandwidth decrease	53.0	0.62	(d)

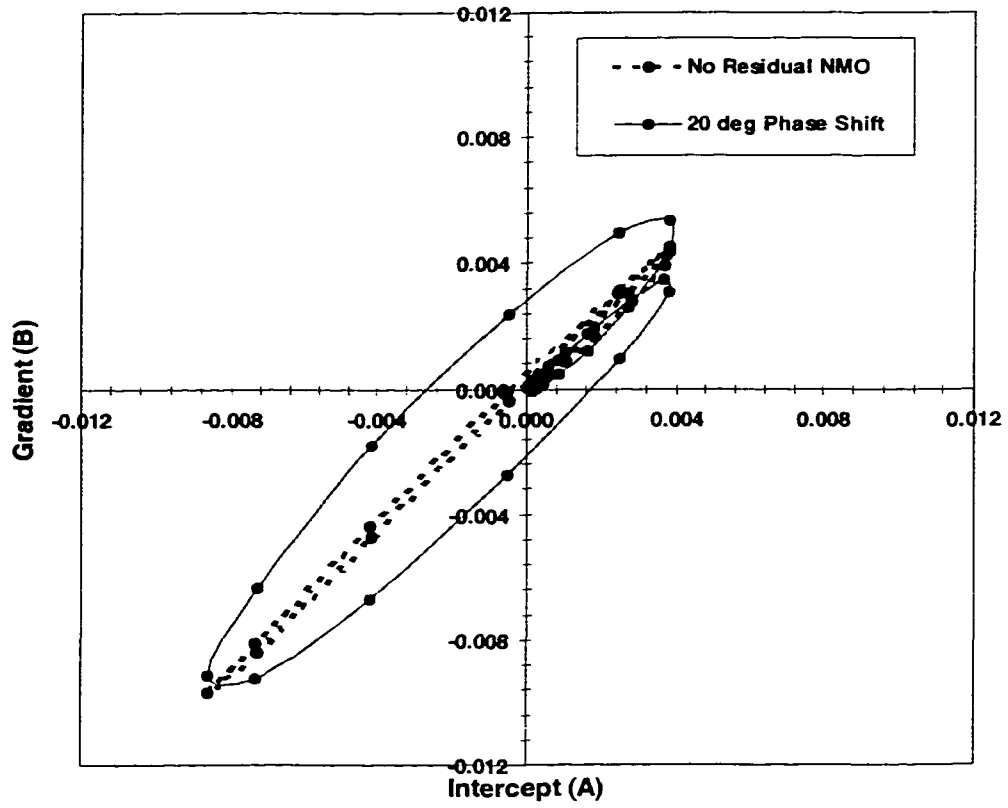
- a -

AVO Hodogram - Top B Sand



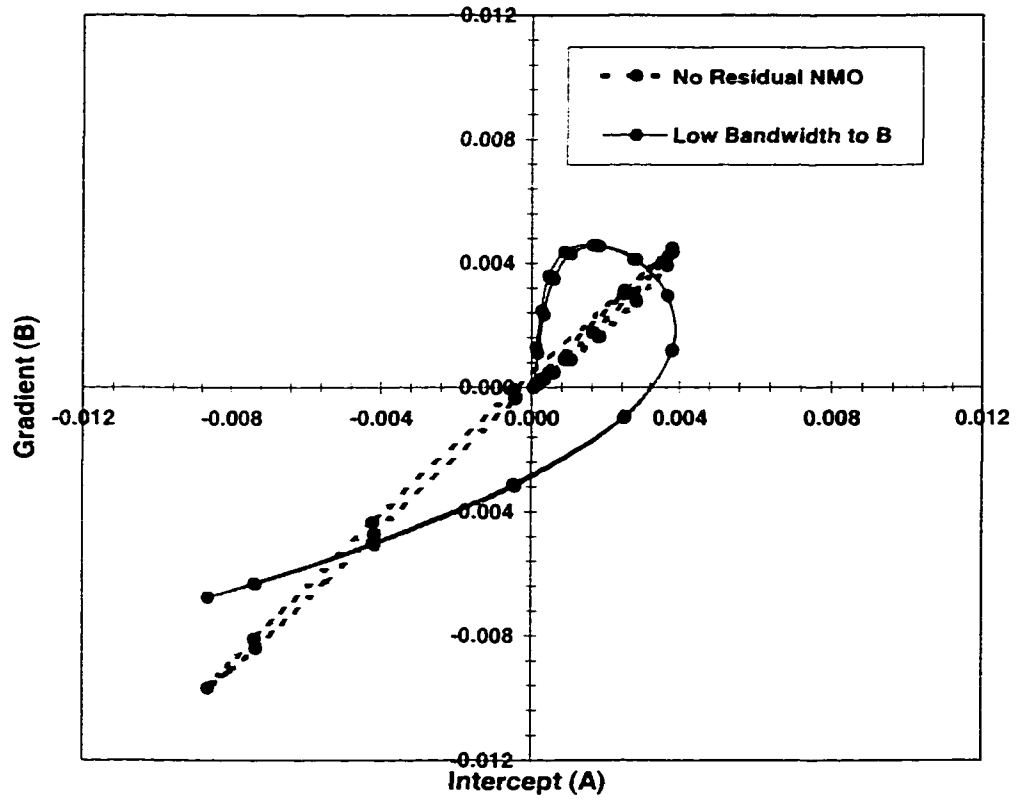
- b -

AVO Hodogram - Top B sand



- C -

AVO Hodogram - Top B Sand



- d -

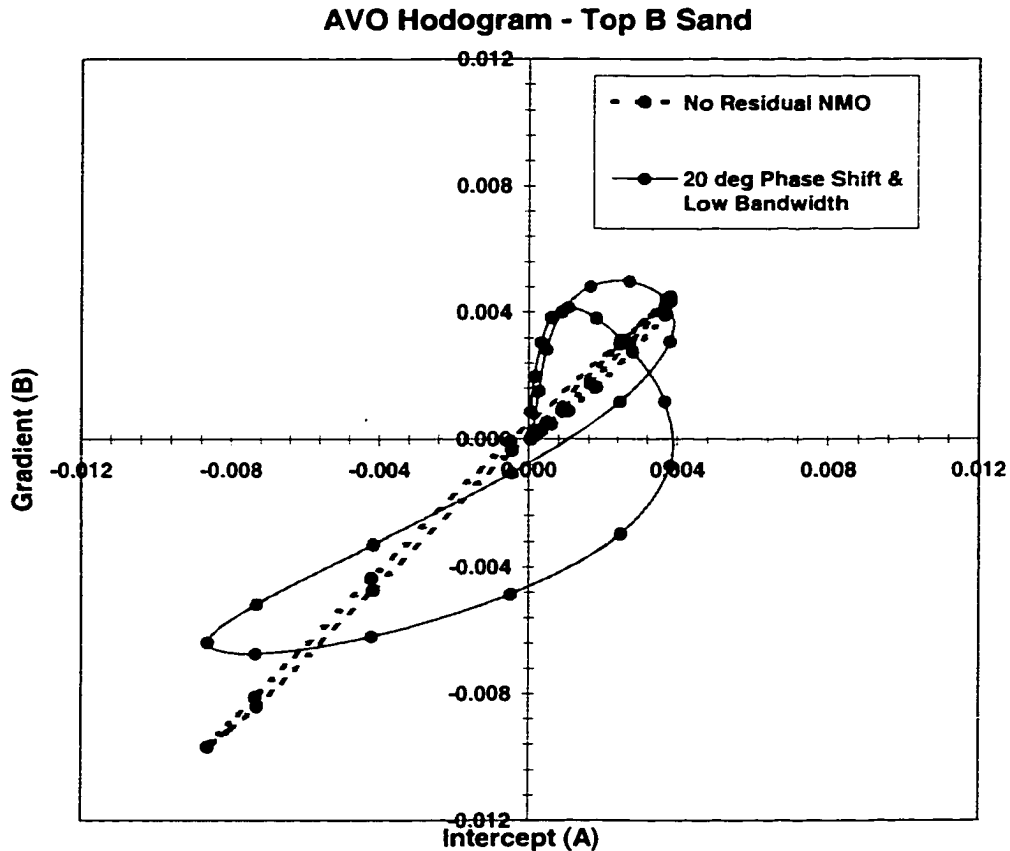


Figure 6.8. Wave propagation and processing effects on the AVO hodogram for the top B Sand reflection. (a) No residual NMO is present on far-offset traces (or gradient trace). (b) A 20-degrees phase shift is added to the far traces. (c) A decrease of frequency bandwidth (bandpass filter: 0-20-30-50 Hz) on the far traces. (d) Superposition of phase shift and decrease of frequency bandwidth. The solid curve corresponds to the hodogram of the case investigated (b, c, and d).

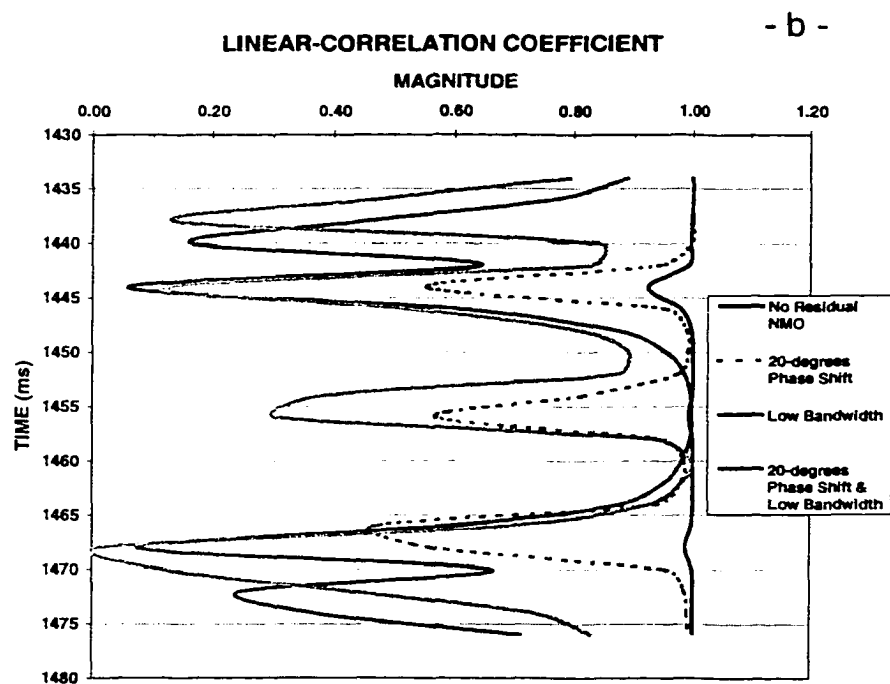
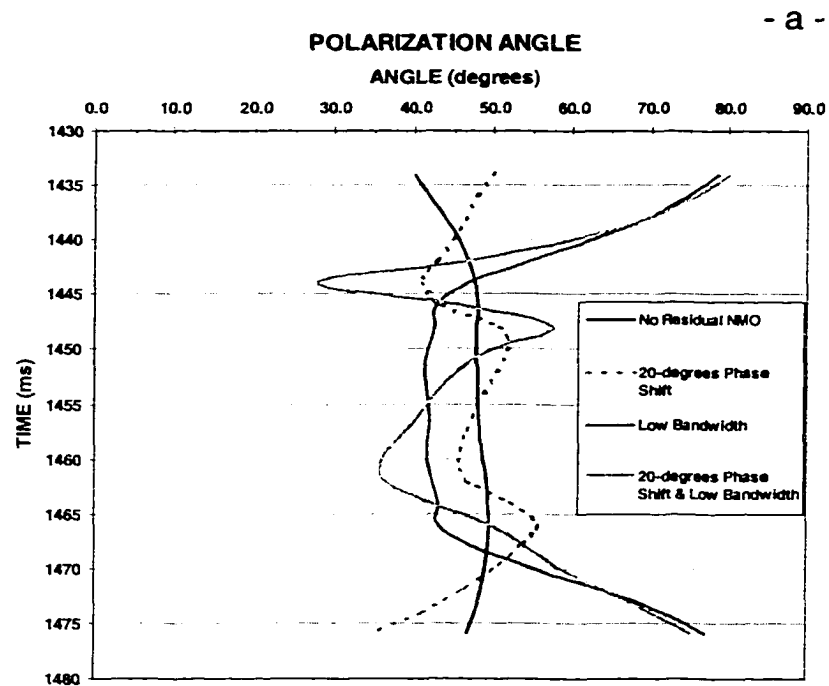


Figure 6.9. Polarization angle and square of linear-correlation coefficient for the top B Sand event. (a) Polarization angle: a fairly constant value between 1445 and 1465 ms for the no residual NMO case (48 degrees) and the low bandwidth case (42 degrees). (b) Linear-correlation coefficient: the no residual NMO exhibits the highest value of r (0.99), inferring that there is no scattering of the data point cloud.

6.4. Thin Layer Modeling

The layer thickness of the model presented in Section 6.1 ranges from 200 ft to 300 ft for all the sand units; values that are greater than the tuning thickness for a given layer. The tuning thickness for each sand layer is determined using its elastic parameters listed on Table 6.1. A dominant frequency of 40 Hz is used for the computation.

The tuning thickness values of the different sand units and their respective thickness used in the thin layer model are shown on Table 6.5. The thickness of the shale/silt layers is kept unchanged.

Table 6.5. Calculated tuning thickness values of the sand units and their respective thickness used in the thin layer model.

Sand Unit	Tuning Thickness $\lambda/4$ (ft)	Thickness Used (ft)
B	72	70
C	74	70
D	80	80
G	74	70
G1	79	75
I	73	70
L	85	80
M	79	75

A synthetic gather is generated using a full elastic wave algorithm of the AVO Modeling of the AVO Hampson-Russell Software. A wavelet with the same

characteristics as the one in Section 6.1 is used. The intercept (A) and the gradient (B) traces are extracted from the synthetic gather (Figure 6.10). The seismic events corresponding to the different sand units occurred at smaller two-way times than the thick-layered model because the layer thickness was reduced. The polarization angle, the polarization angle difference, and the strength are computed using a sliding window of 20 ms. For a better representation of the sample points, a 50-ms window is used to compute the linear-correlation coefficient attribute. A constant background polarization of -20 degrees (Figure 6.11) is used along the entire trace to compute the polarization angle difference as defined in Equation 4.12.

It can be observed that the polarization attributes computed from both models, layers above tuning thickness (Figure 6.12) and thin layers (Figure 6.13) exhibit the different seismic events. However, a finer and detailed representation of the seismic data is obtained for the model with thicker layers.

The synthetic CDP gathers generated from the two models, the product of strength and polarization angle difference, and the linear-correlation coefficient are displayed in Figures 6.14 and 6.15. The computed attributes are reliable where the linear-correlation coefficient has a high value and less reliable where the linear-correlation coefficient is very small. It can be observed that intervals of gas sands exhibit large AVO effects in both cases (thick and thin layers) as measured by these attributes.

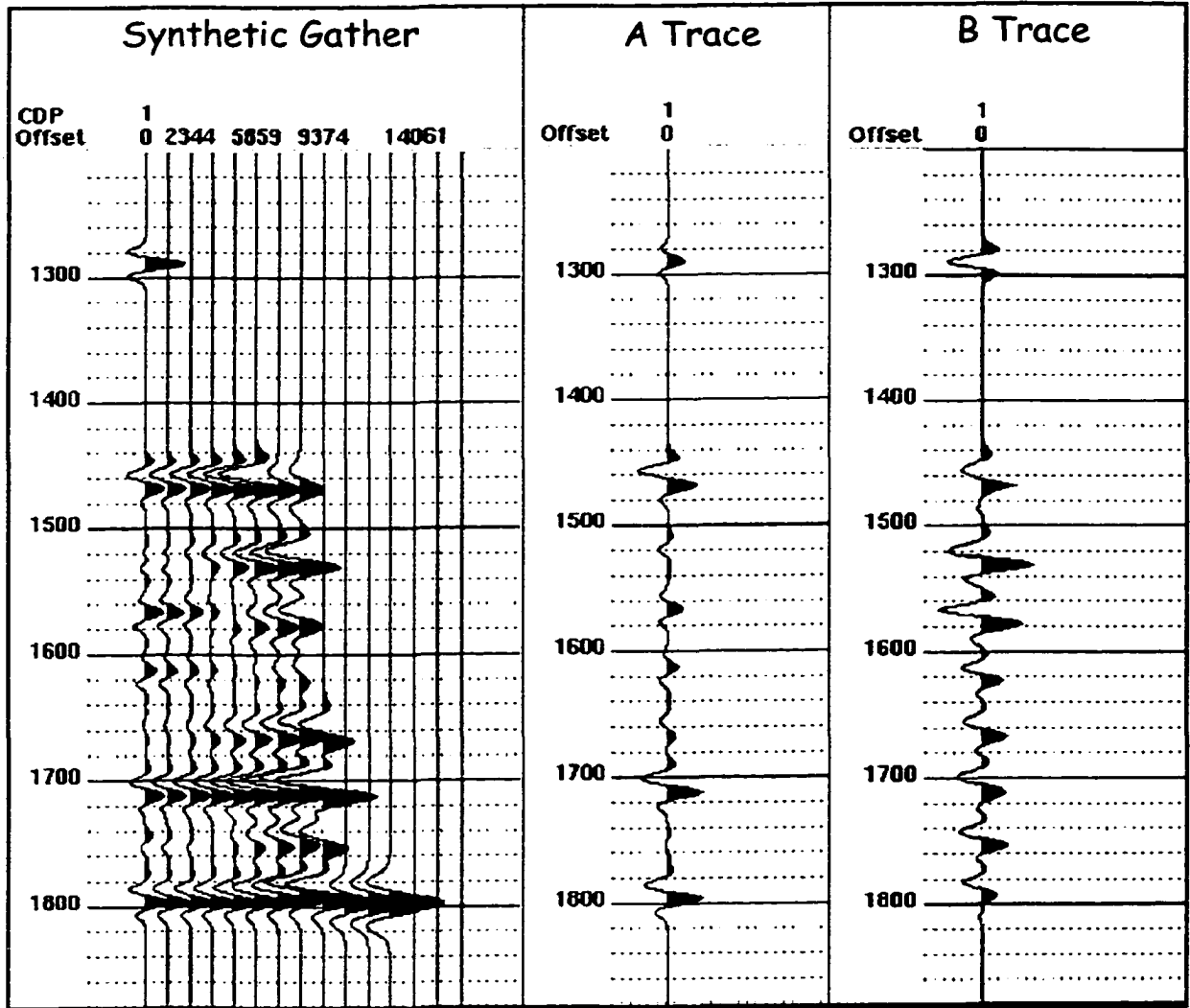


Figure 6.10. Extracted intercept (A) and gradient (B) traces along with the synthetic CDP gather from the thin-layered model. The top B Sand reflection is at 1450 ms.

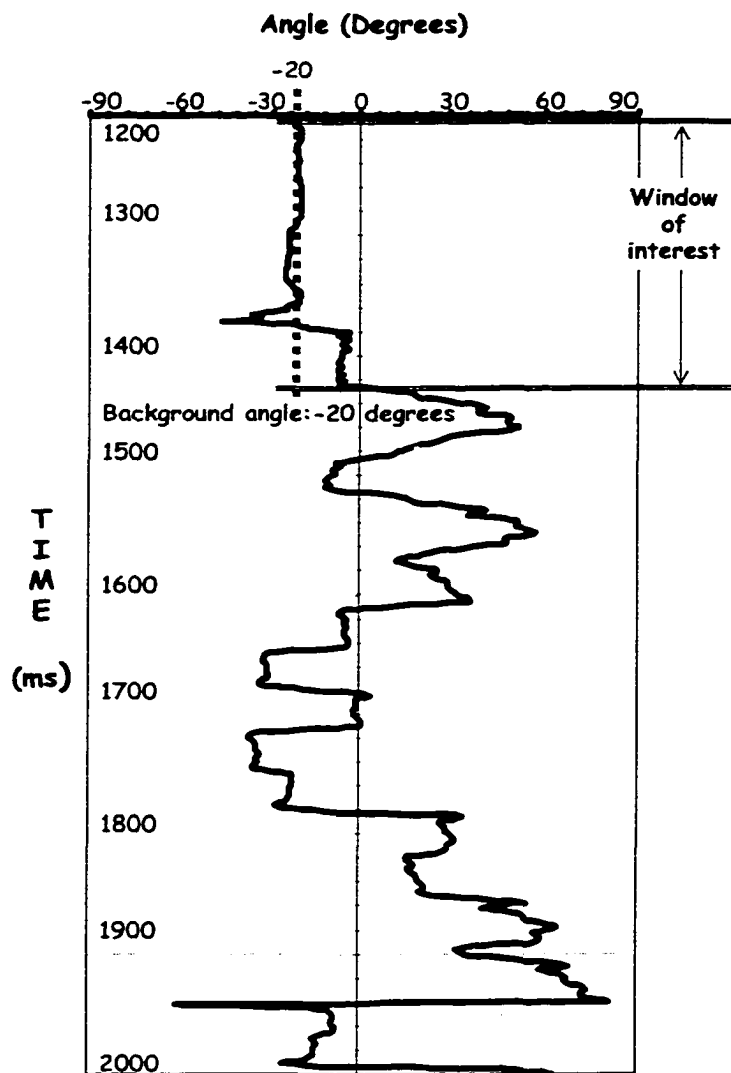


Figure 6. 11. Background polarization angle determination. The background angle is the arithmetical average of the polarization angles between 1200 and 1420 ms.

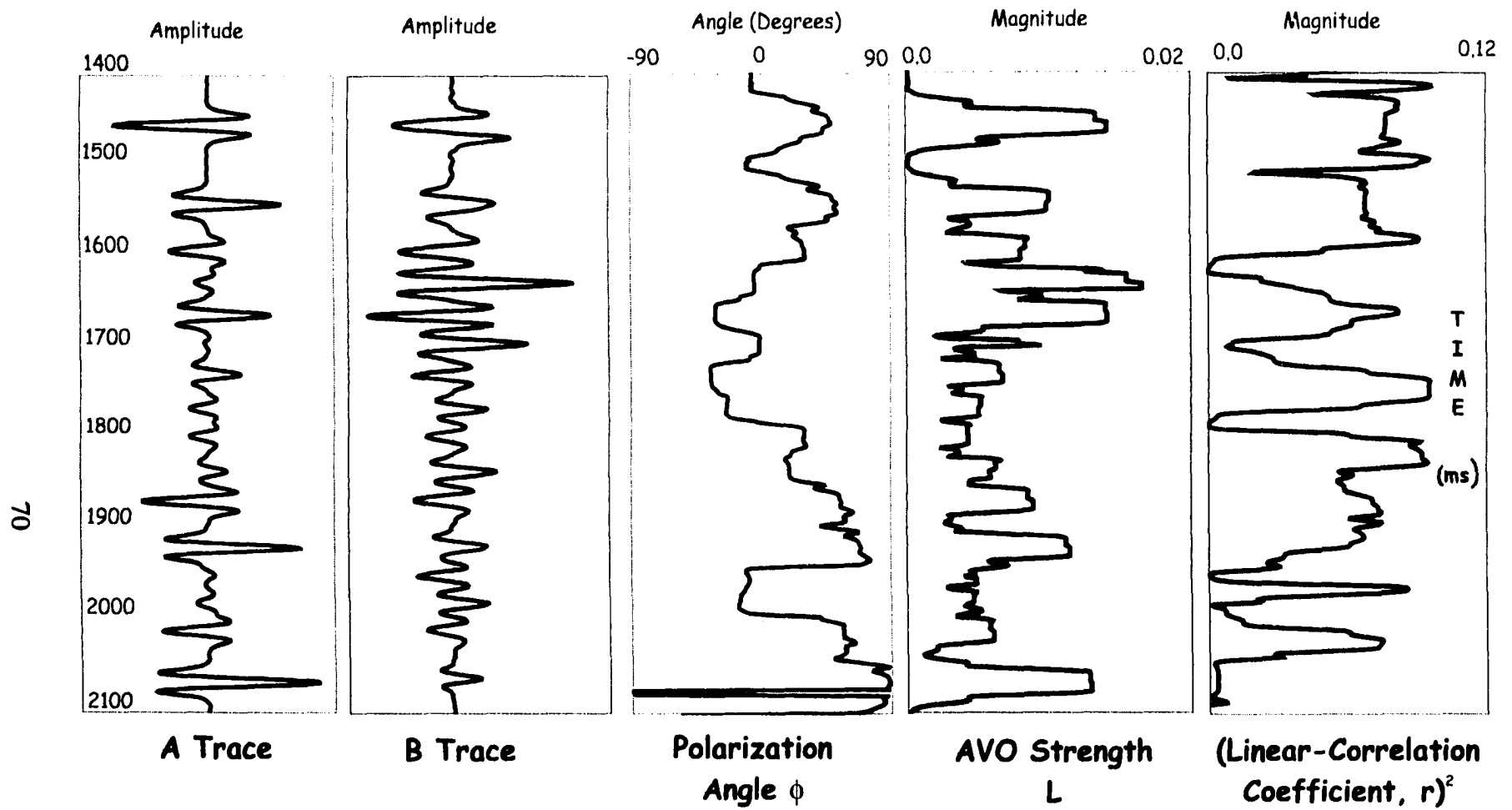


Figure 6.12. Display of intercept (A) trace, gradient (B) trace, polarization angle, AVO strength, and squared linear-correlation coefficient computed from the synthetic gather with layer thickness above the tuning thickness.

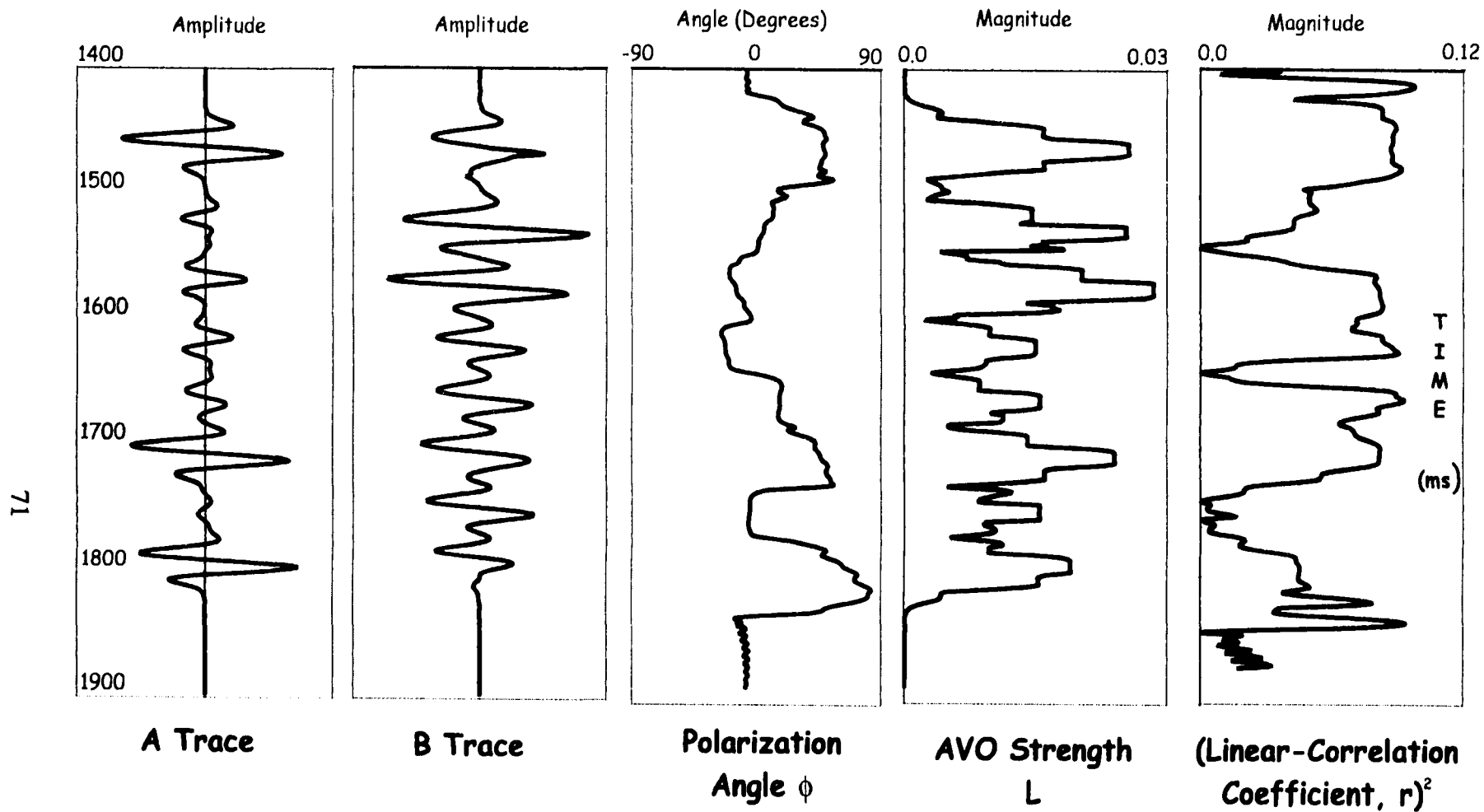


Figure 6.13. Display of intercept (A) trace, gradient (B) trace, polarization angle, AVO strength, and squared linear-correlation coefficient computed from the synthetic gather with thin layers.

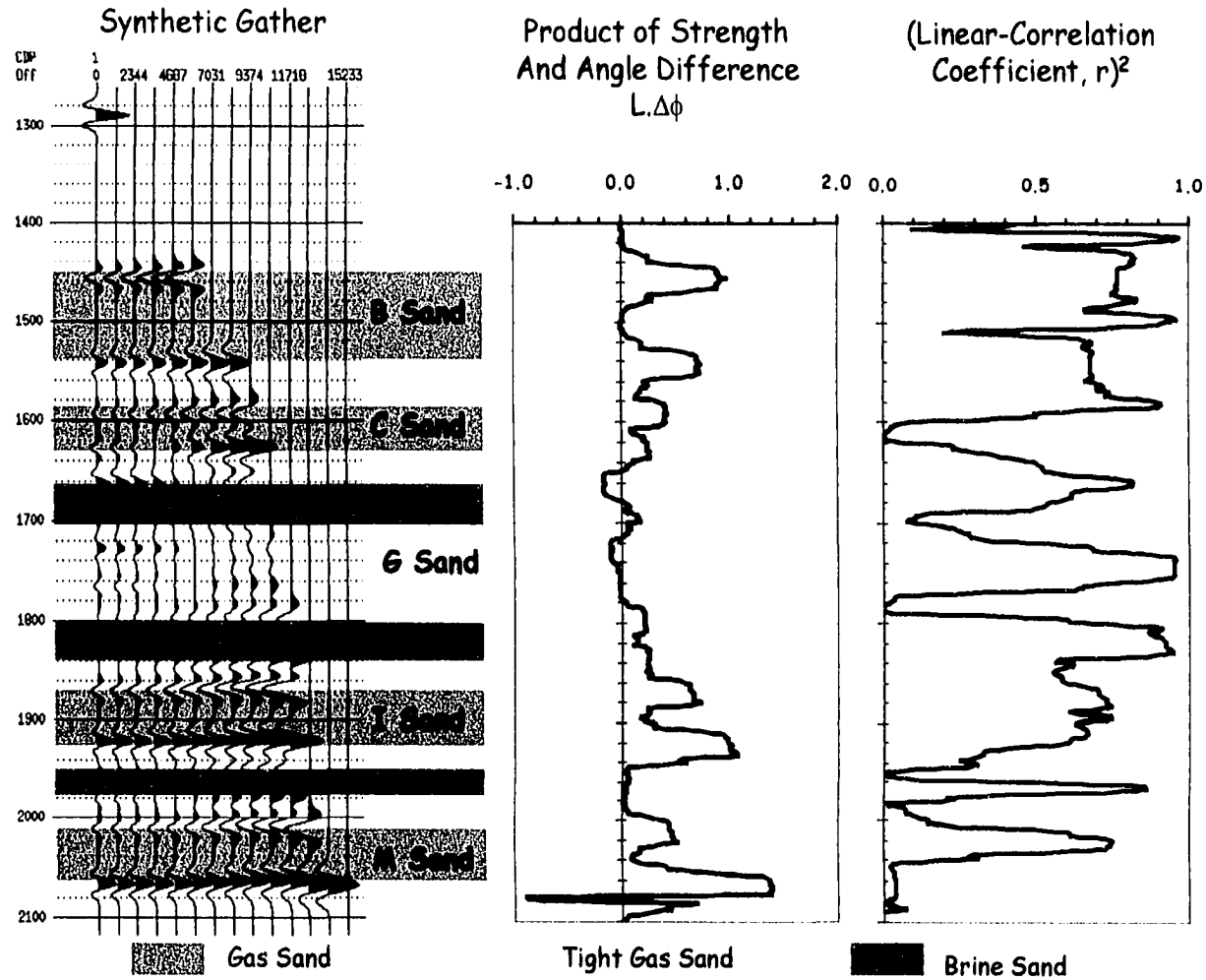


Figure 6.14. Display of the synthetic gather, the product of strength and polarization angle difference, and the squared linear-correlation coefficient for the thick-layered model. The sand units are highlighted: red for the gas sands, blue for the brine sands, and hatched red for tight gas sands.

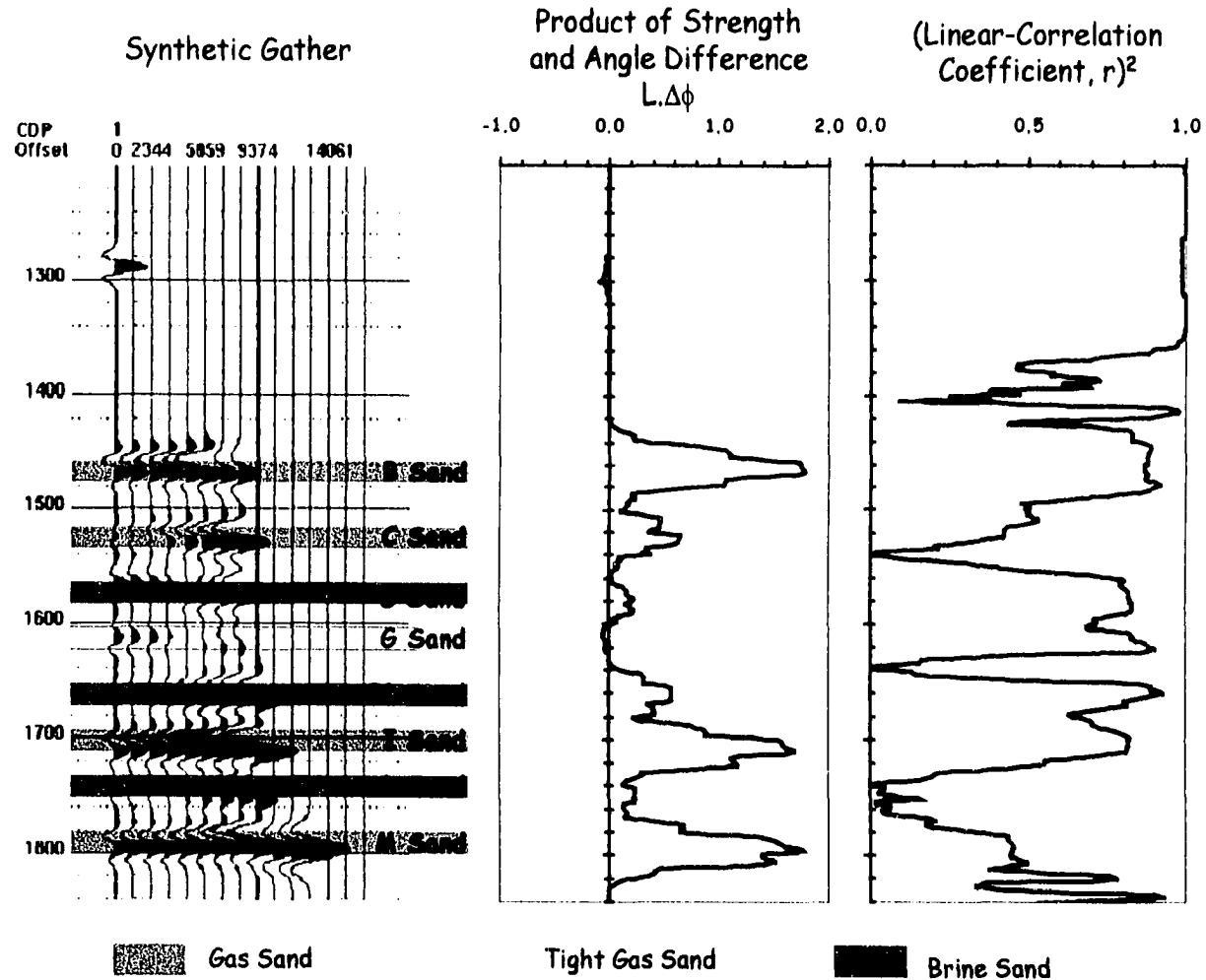


Figure 6.15. Display of the synthetic gather, the product of strength and polarization angle difference, and squared linear-correlation coefficient for the thin-layered model. The sand units are highlighted: red for the gas, blue for the brine sands, and hatched red for tight gas sands.

Chapter 7

A CASE STUDY

To investigate the methodology, the polarization attributes are computed using real seismic data from the Gorgon field of the Northwest Shelf of Australia. The seismic processing sequence performed on the gathers is presented. Then, the resulting polarization attributes are used to identify the known hydrocarbon intervals.

7.1 Study Area

The Gorgon field is a north-northeast trending Triassic horst block, about 65 kilometers long and 5 kilometers wide, which lies in water depths ranging from 200 to 300 meters, about 130 kilometers off the Western Australian coast (Figure 7.1). The structure is at the southern-most end of the Rankin Trend of the northern Carnarvon Basin.

The general stratigraphy and major tectonic events in the Gorgon area are summarized on Figure 7.2. The stratigraphic unit of interest, the Mungaroo Formation, Late Triassic in age is a fluvial sequence of interbedded sandstone and siltstone and claystone, which was deposited regressively over the Locker Shale in the Mid-Late Triassic. The drilled stratigraphic thickness of the Mungaroo Formation in the Gorgon area is about 2000 meters. Fluvial sands of the Mungaroo Formation are the main reservoirs of the Northwest Shelf gas accumulations (e.g. Gorgon field). The average gross thickness of reservoir units is between 75 and 300 meters.

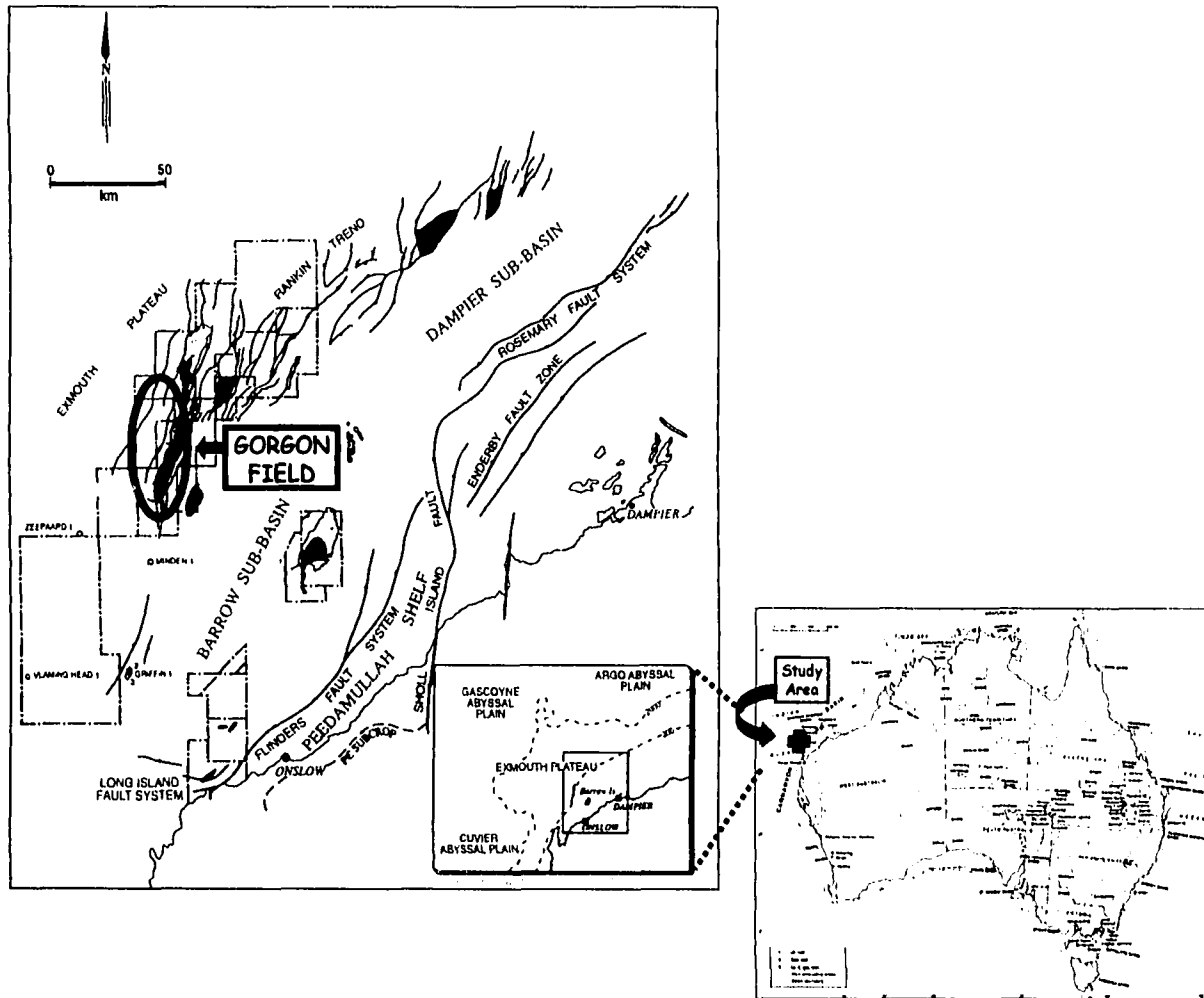


Figure 7.1. Map of the study area, showing the location of the Gorgon field and the Carnarvon Basin, NW Shelf of Australia.

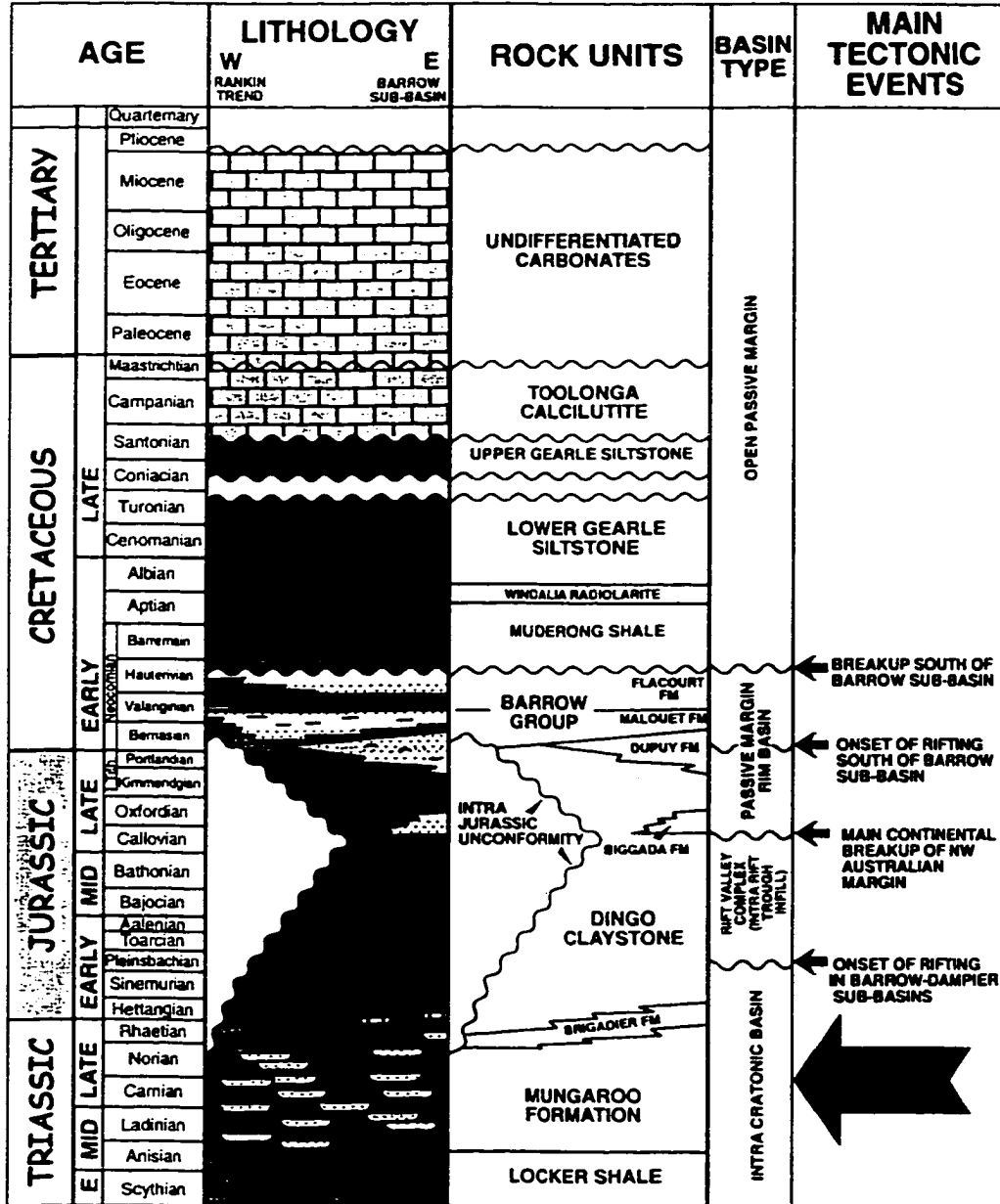


Figure 7.2. Generalized stratigraphy of the Barrow-Dampier sub-basin within the Carnarvon basin. The Gorgon field occurs within the Triassic-Lower Jurassic Mungaroo Formation (large arrow) (Modified after Kopsen and McGann, 1985).

7.2 Seismic Data

The Gorgon 3-D marine survey was acquired by Western Geophysical using the M.V. Western Horizon. The full-fold survey covered an area of 1170 km² totaling 48,500 km of subsurface data. Dual 4000-meter streamers and 1575 cubic inch source arrays were used. Four subsurface lines of nominally 50 fold were acquired at 25-meter line spacing for each sail line.

Data were processed by Western Geophysical and CGG to maintain true relative amplitudes and to increase the signal-to-noise ratio. The processing flow included:

- 1) Minimum phase low cut filter
- 2) Resampling from 2 to 4 ms
- 3) Trace edit (automatic despiking)
- 4) Merging of navigation data and binning
- 5) Instrument dephase
- 6) True amplitude recovery
- 7) Adjacent trace summation
- 8) Q compensation
 - a. Function: 90, 100, 110, 130, 150, 170
- 9) Shot averaged spiking deconvolution
 - a. Operator: 240 ms
 - b. 2 windows: 0 - 3000, 2500 - 4500
- 10) Water layer replacement statics
- 11) Tidal static correction
- 12) NMO correction

- 13) Mute
- 14) Radon anti-multiple: moveout (ΔT) cutoff of 80 ms
- 15) Flexible binning (150 %)
- 16) 3-D DMO
- 17) Pre-stack time migration (PSTM) per offset cube
- 18) NMO correction after 2nd pass picking
- 19) Second pass Radon anti-multiple
- 20) Phase correction to zero phase

Four 2-D lines, picked from the 3-D survey, are used for this study (Figure 7.3). The lines are tie lines at well locations. The dominant frequency of the seismic data is roughly 30 Hz and a theoretical quarter wavelength ($\lambda/4$) tuning thickness is about 30 meters (or 18 milliseconds two-way time) in the Mungaroo reservoir section. Some of the known gas and brine intervals are highlighted on the seismic sections (Figure 7.4).

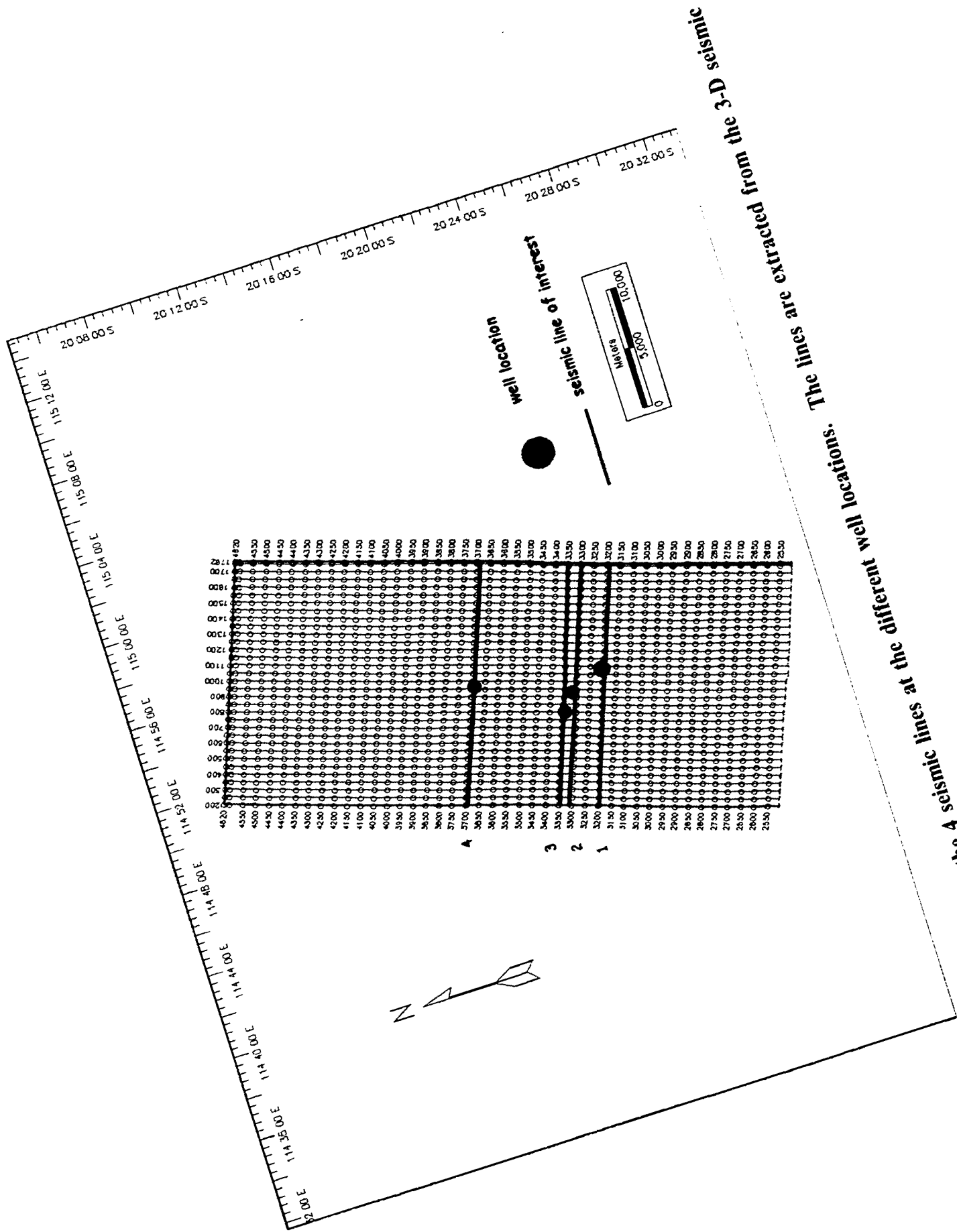


Figure 7.3. Map showing the A seismic lines at the different well locations. The lines are extracted from the 3-D seismic survey.

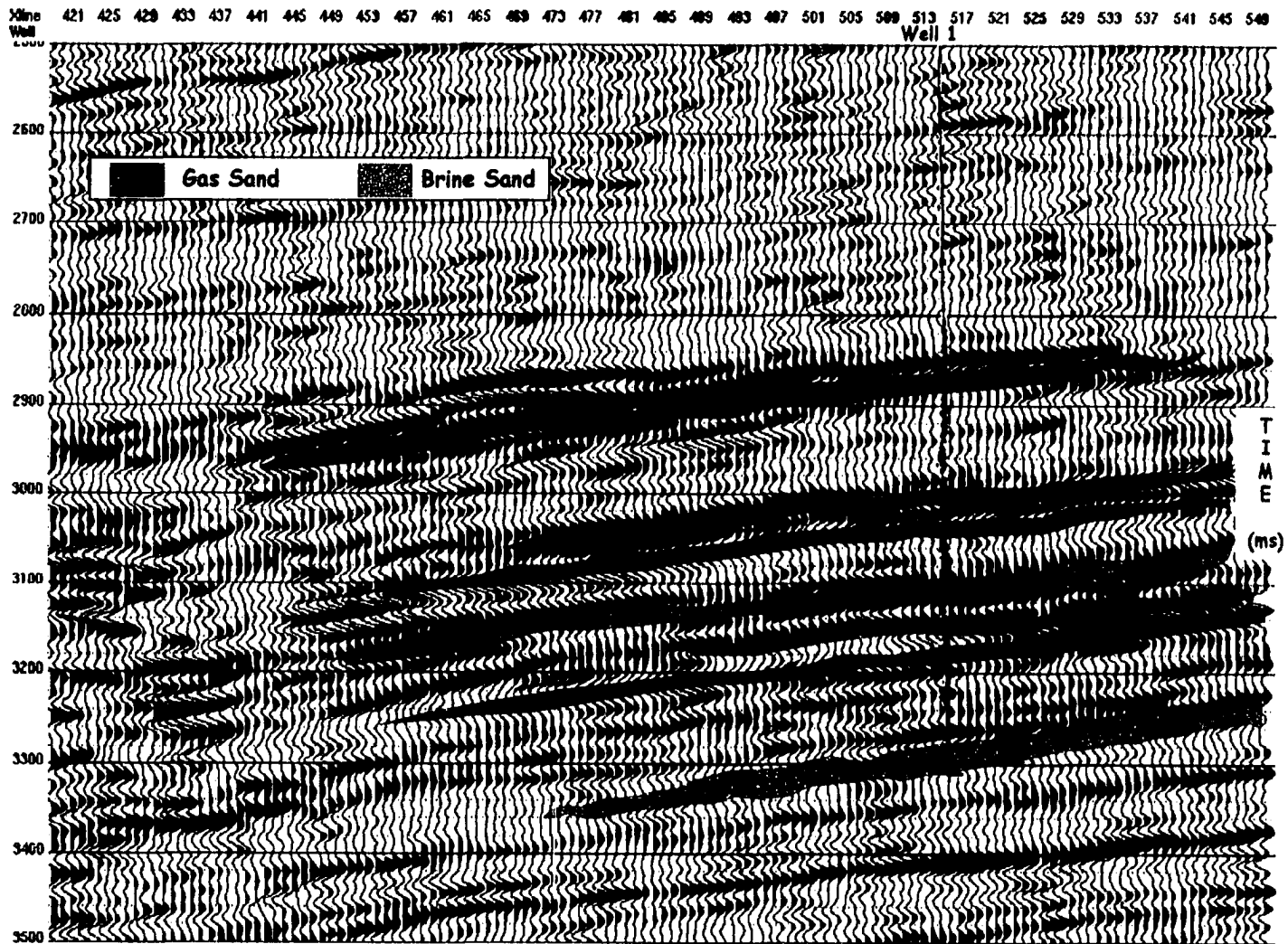


Figure 7.4a. Seismic line 1. The well is roughly at crossline 515. The line runs E-W as shown in Figure 3 and represents a stacked section. Known gas and brine zones are highlighted.

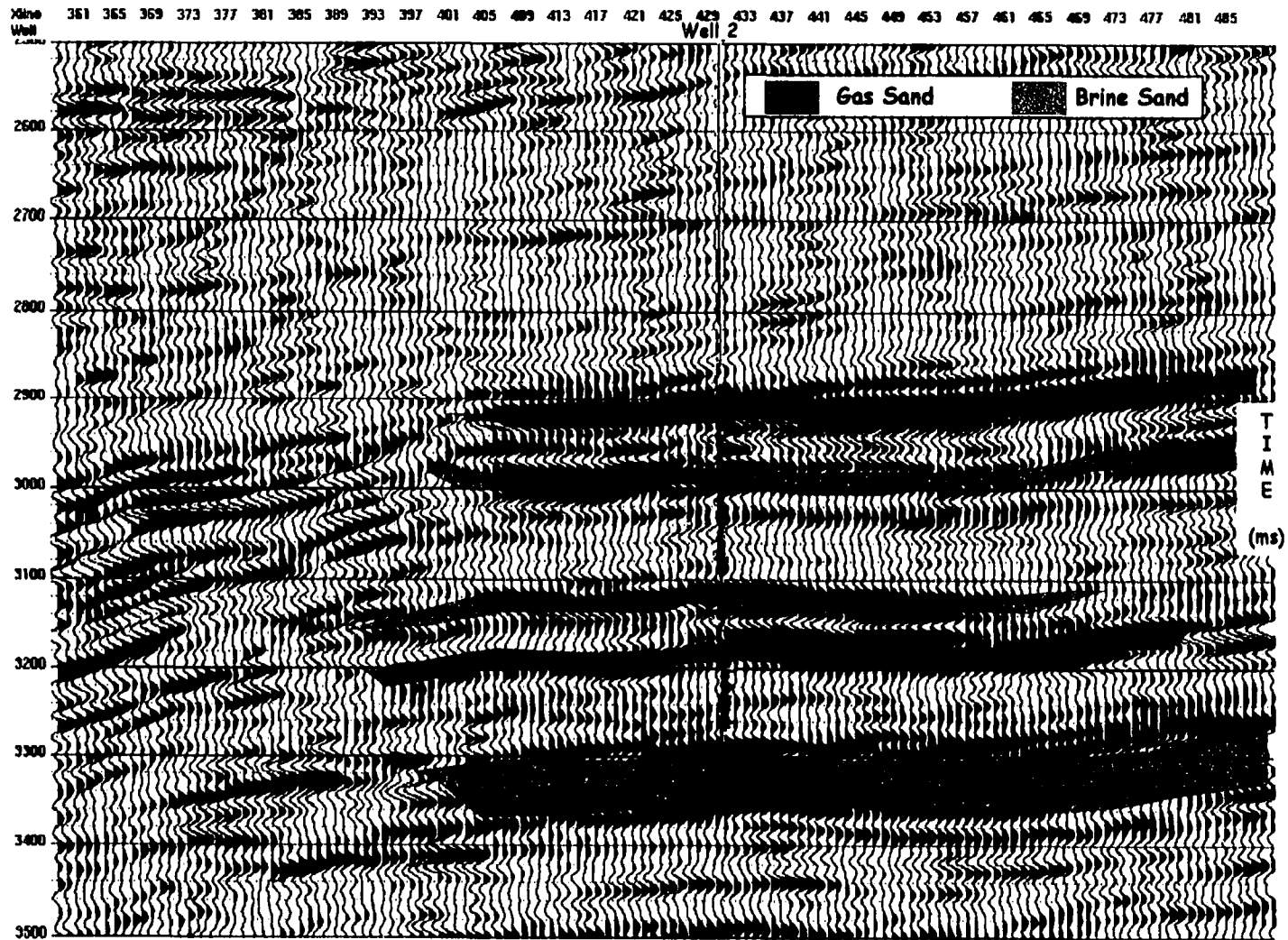


Figure 7.4b. Seismic line 2. The well is approximately at crossline 430. The line runs E-W as depicted in Figure 3 and represents a stacked section. Known gas and brine intervals are highlighted.

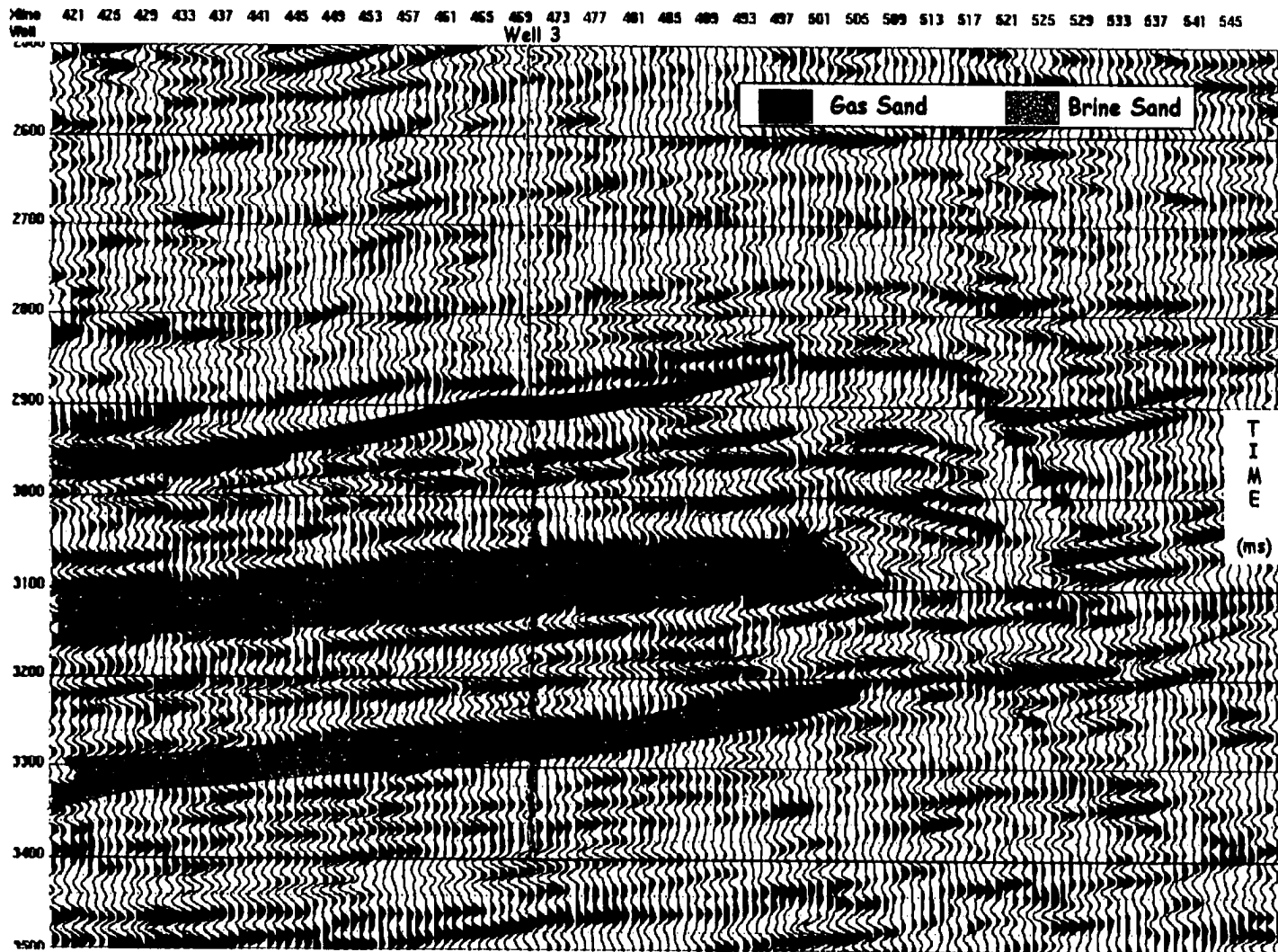


Figure 7.4c. Seismic line 3. The well is approximately at crossline 470. The line runs E-W as depicted in Figure 3 and represents a stacked section. Known gas and brine zones are shown.

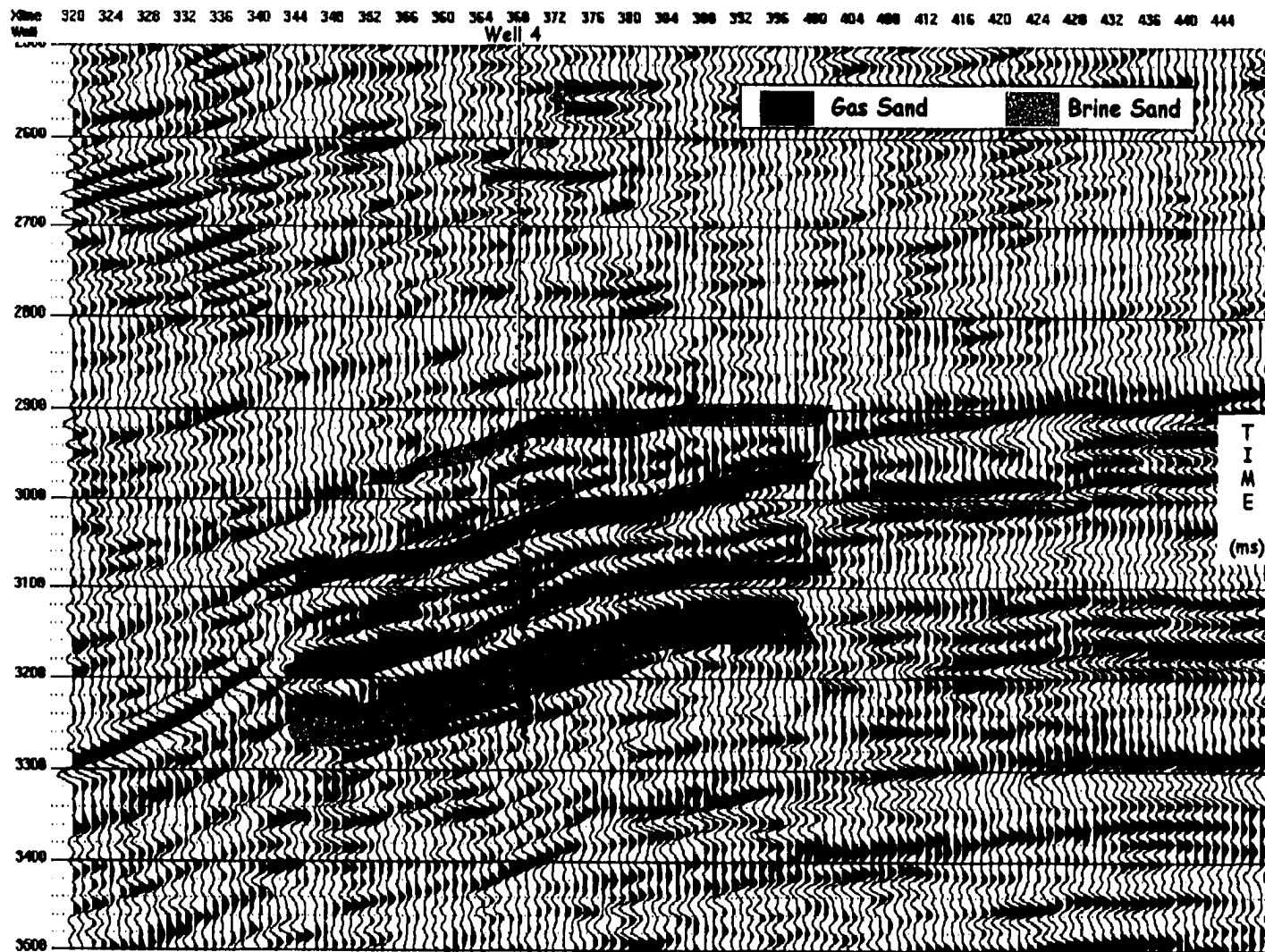


Figure 7.4d. Seismic line 4. The well is approximately at crossline 368. The line runs E-W as shown in Figure 3 and represents a stacked section. Known gas and brine intervals are depicted.

7.3 Conventional AVO Attributes

Prior to extracting the intercept (A) and the gradient (B) traces, bandpass filtering is applied to the pre-stack time migrated (PSTM) gathers that have been phase corrected to zero phase. The characteristics of the trapezoidal filter are 5-10-45-75 Hz.

To perform the gradient analysis, the corrected sonic curve at each well location is used as a velocity function for offset-to-angle transformation. The correction of the sonic curves results from considering time-depth tables. The aim of the analysis is to approximate seismic amplitudes as a function of $\sin^2(\theta)$ in the first order as shown in Equation 3.1. The following constraints are set during the analysis to prevent from getting erroneous extraction results:

- Range of incidence angles: 8 to 32 degrees
- Range of offsets: 280 to 3,160 meters

The resulting intercept, gradient, AVO product, and scaled Poisson's ratio change (or fluid factor) sections for each line are depicted in Figures 7.5–7.8. The known hydrocarbon and brine zones are highlighted and color-coded. Note the porous gas intervals correspond to larger AVO product and fluid factor than the brine sands. However, porous brine sands exhibit also large values.

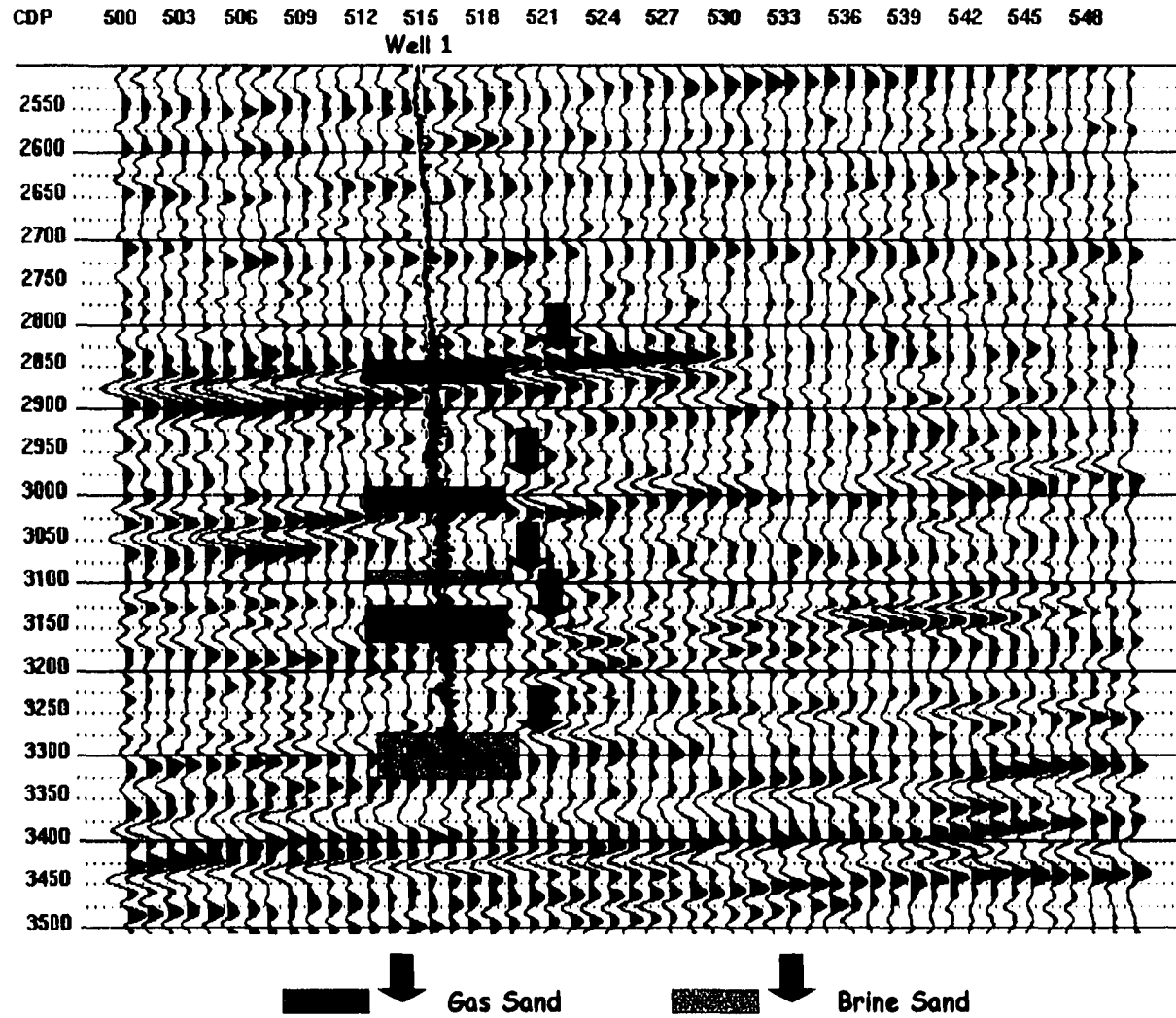


Figure 7.5a. AVO intercept (A) section for seismic line 1. Known gas zones are shown in red, whereas brine intervals are indicated in blue.

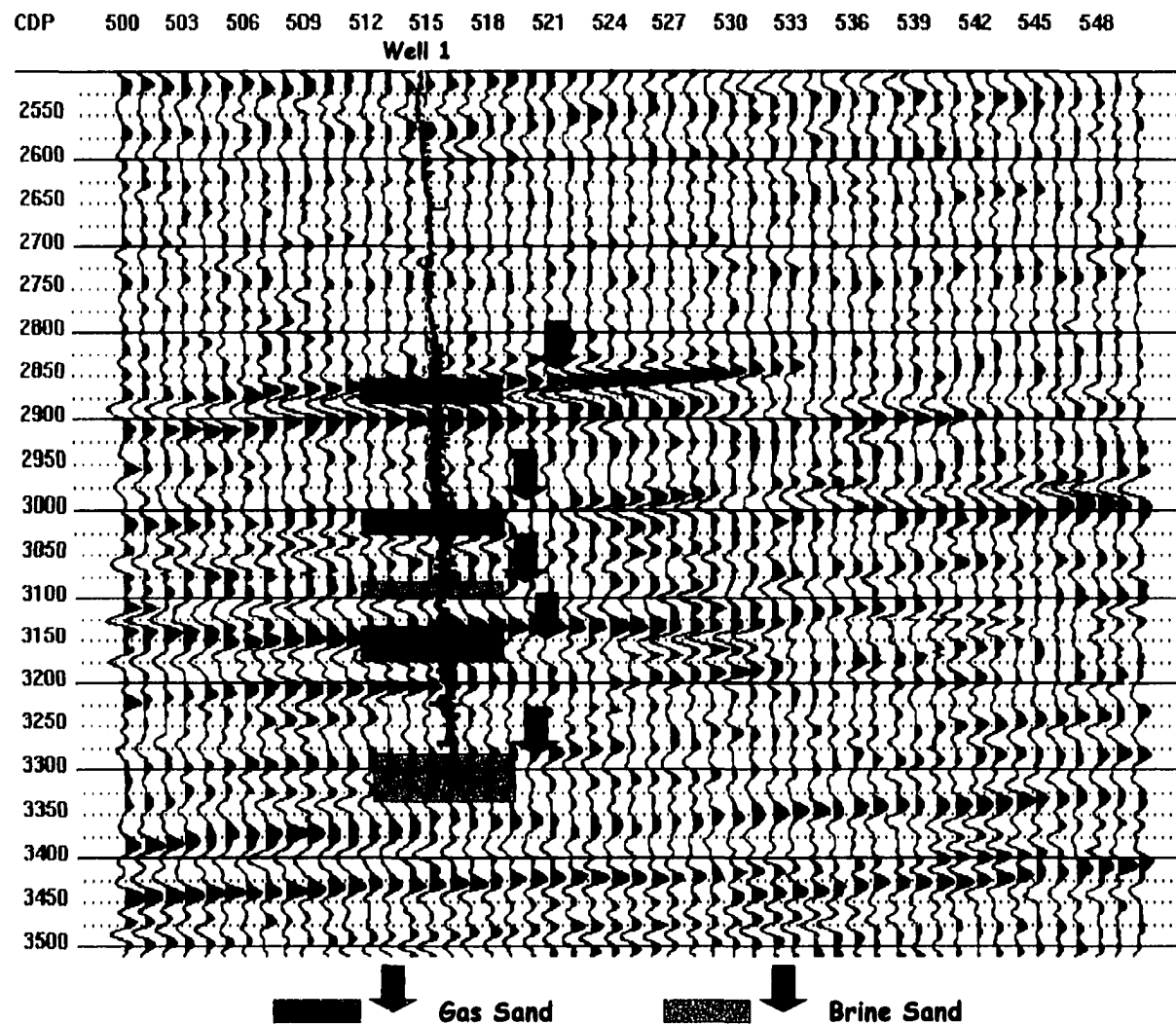


Figure 7.5b. AVO gradient (B) section for seismic line 1. Known brine zones are highlighted in blue, whereas gas intervals are shown in red.

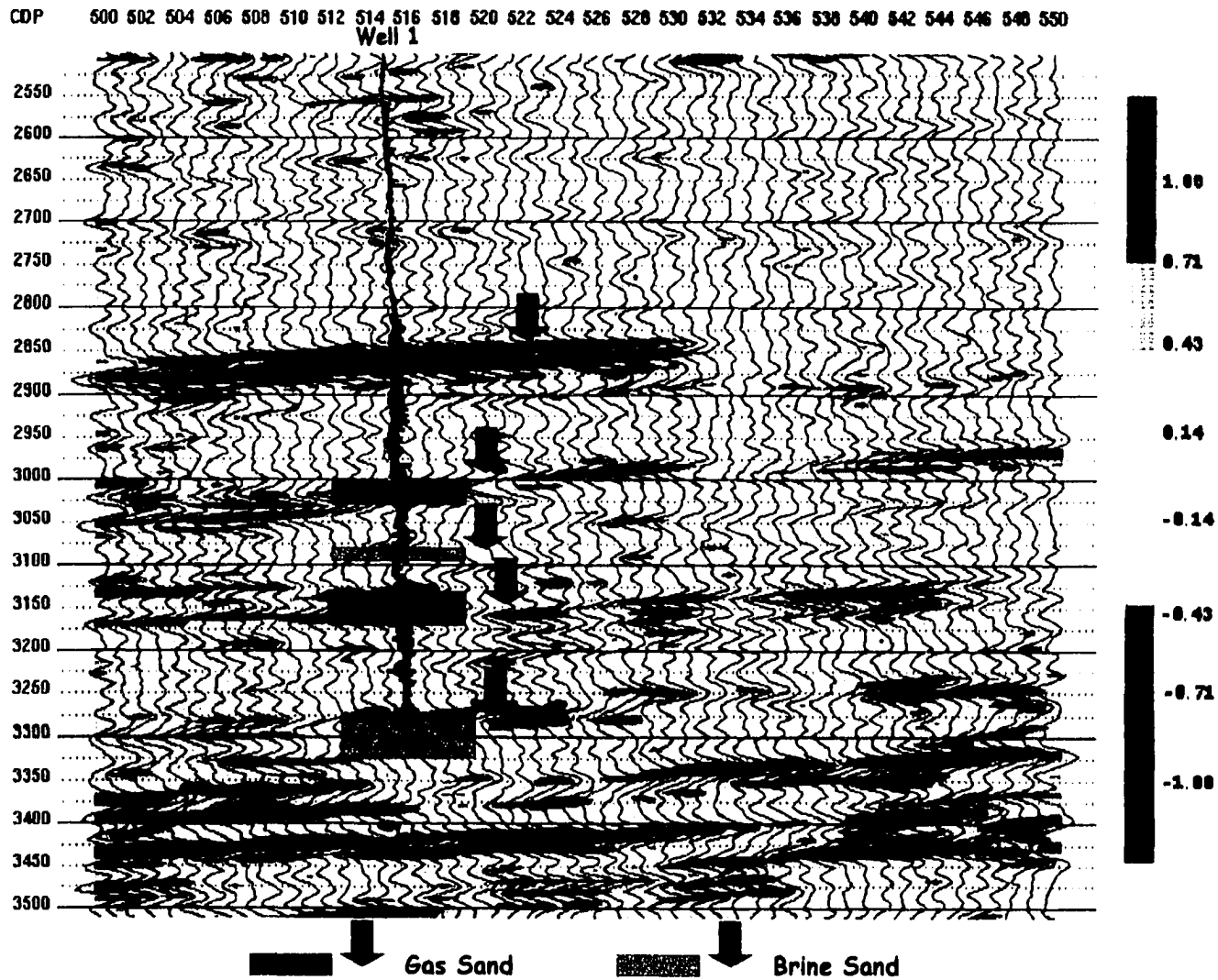


Figure 7.5c. AVO product (A*B) section for seismic line 1. Known gas intervals are indicated in red, whereas brine zones are shown in blue.

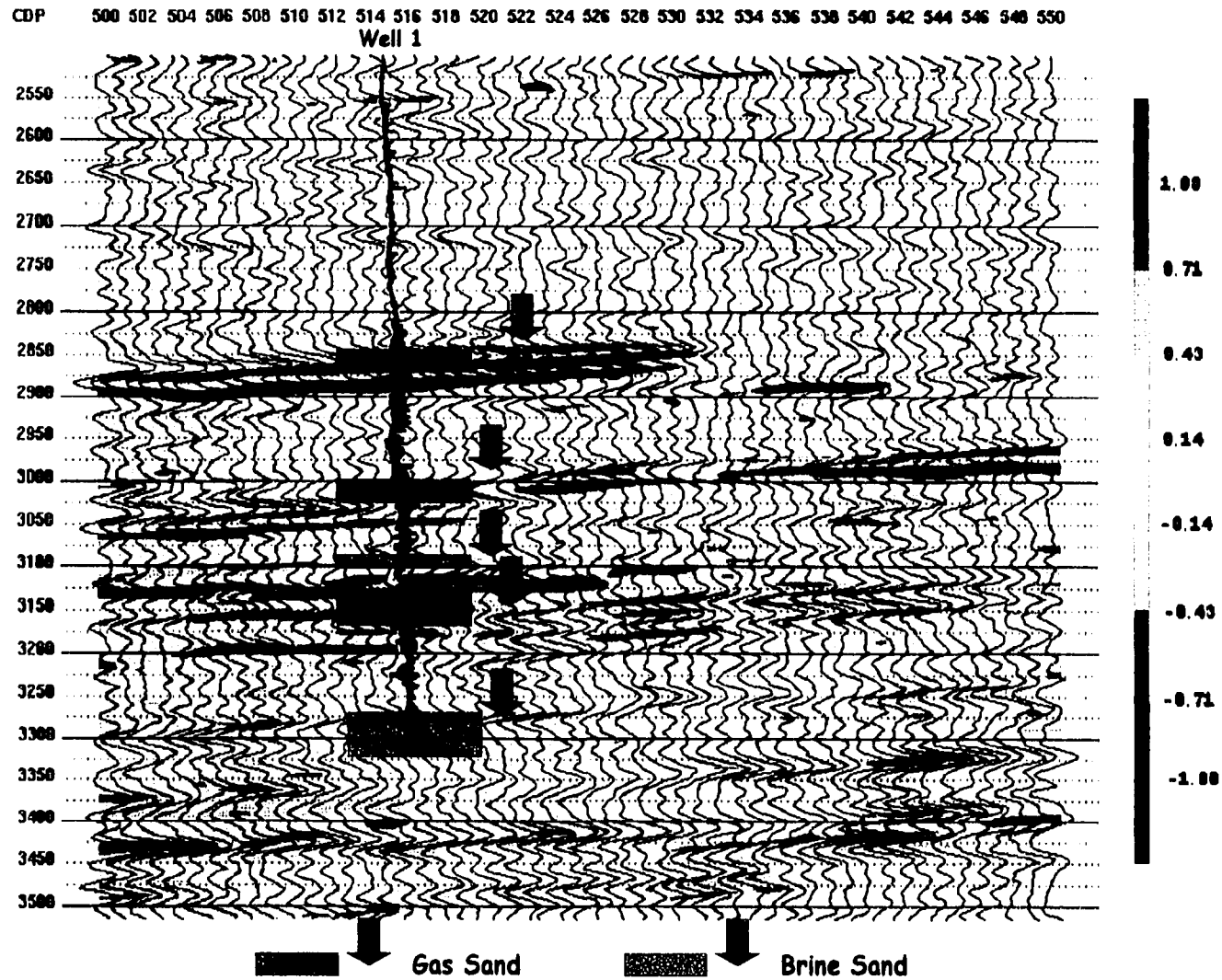


Figure 7.5d. Scaled Poisson's ratio change or fluid factor section for seismic line 1. Known gas zones are indicated in red, whereas brine intervals are shown in blue.

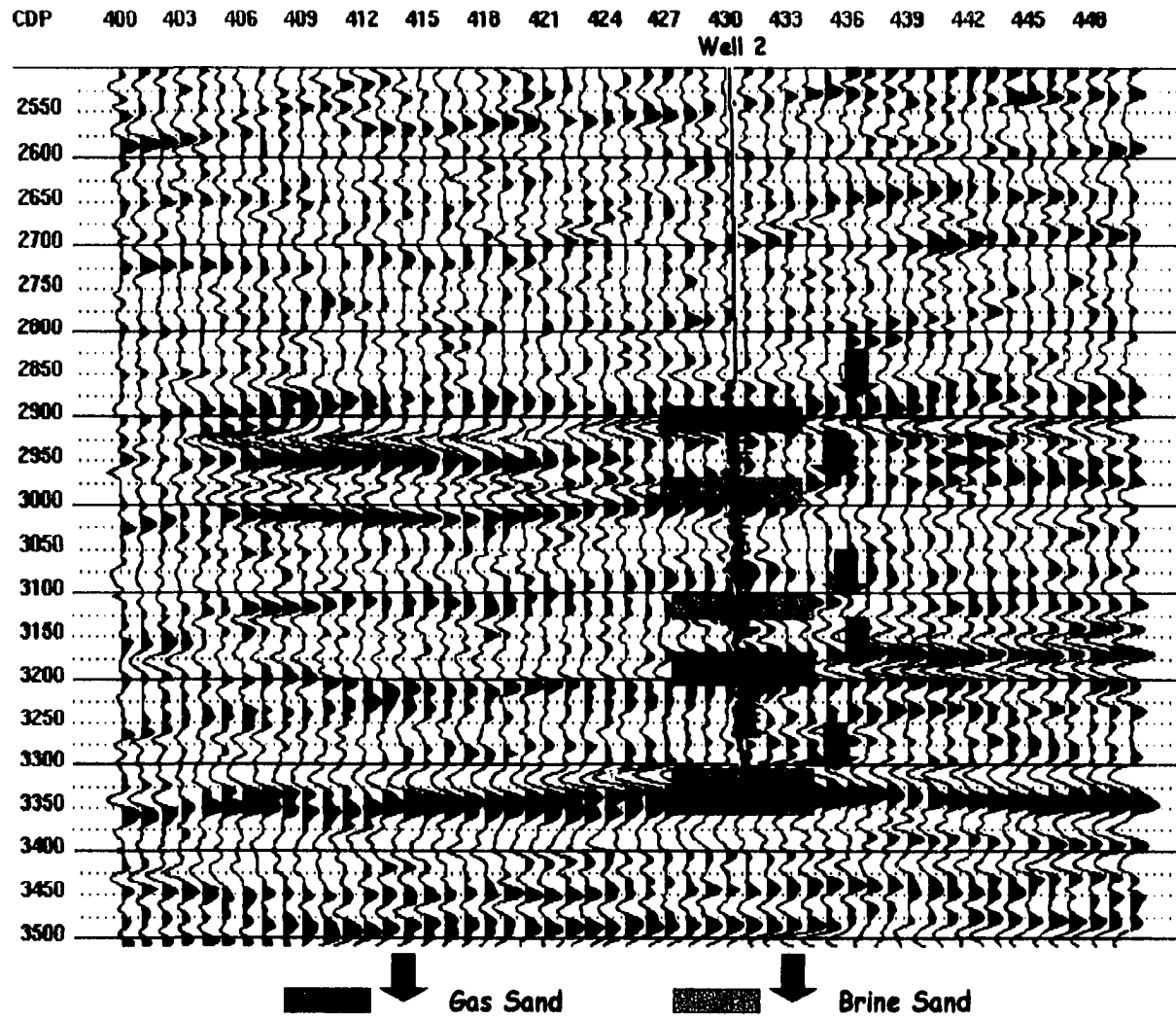


Figure 7.6a. AVO intercept (A) section for seismic line 2. Known gas and brines intervals are indicated in red and blue, respectively.

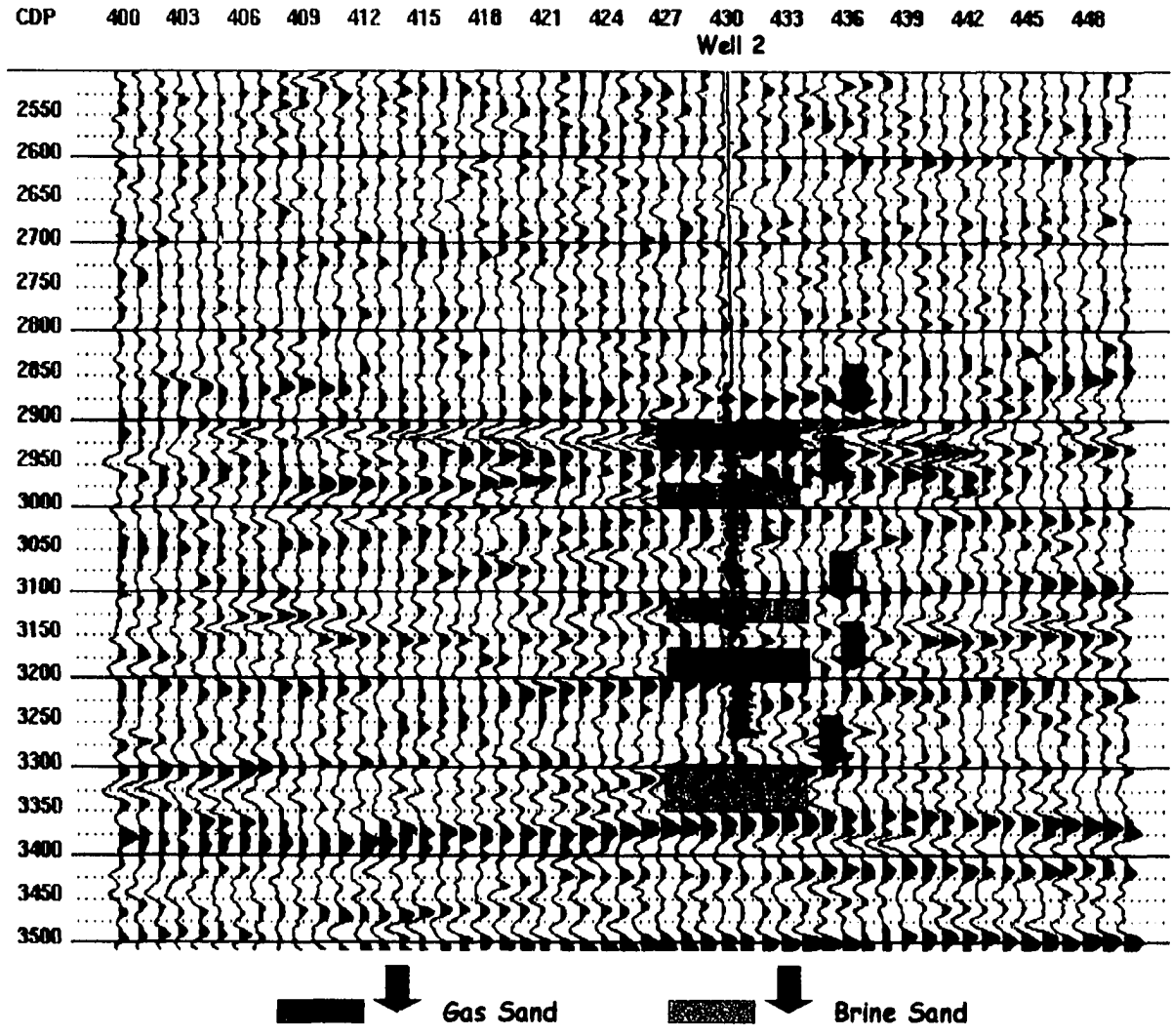


Figure 7.6b. AVO gradient (B) section for seismic line 2. Known gas and brine zones are shown in red and blue, respectively.

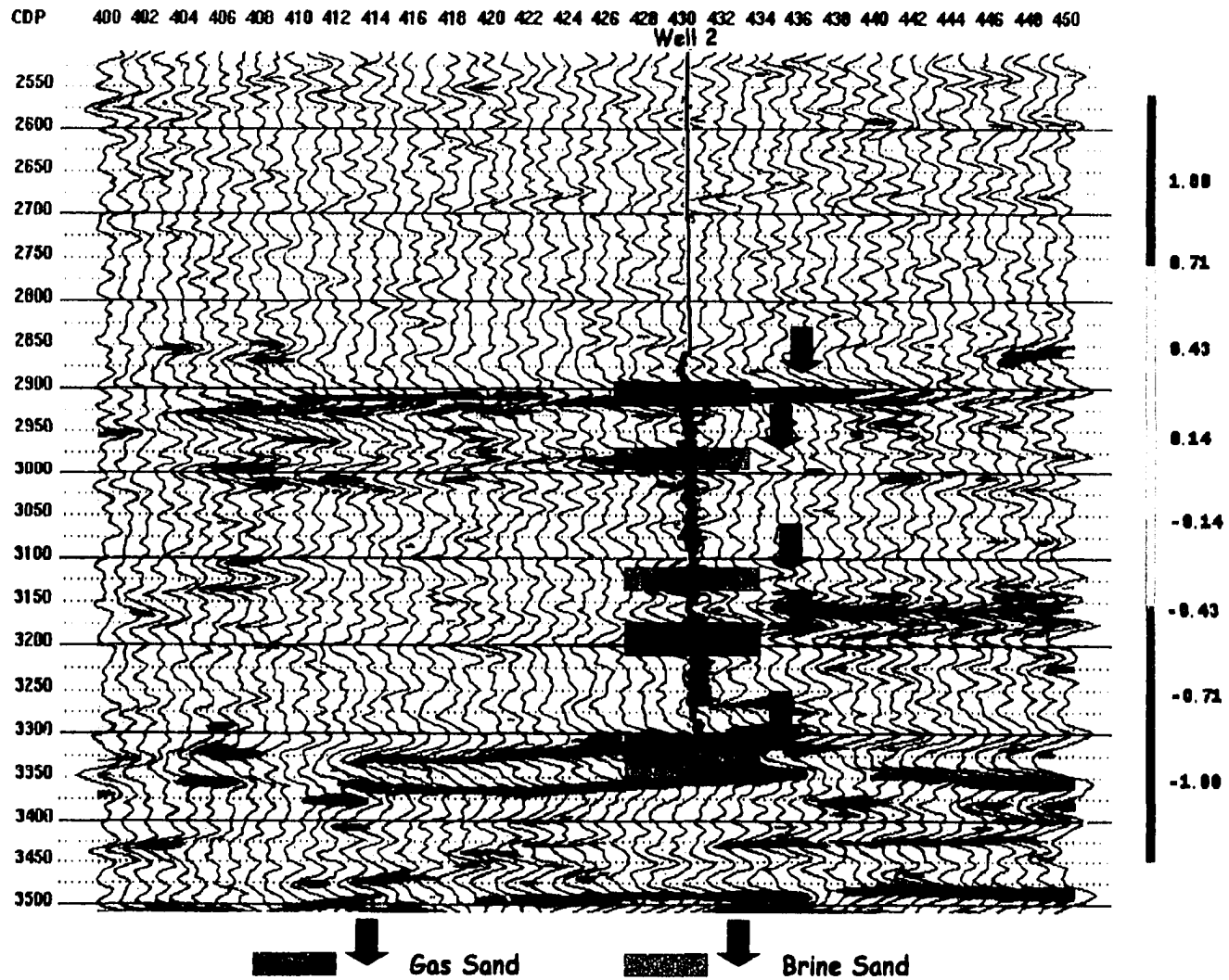


Figure 7.6c. AVO product (A*B) section for seismic line 2. Known brine and gas intervals are indicated in blue and red, respectively.

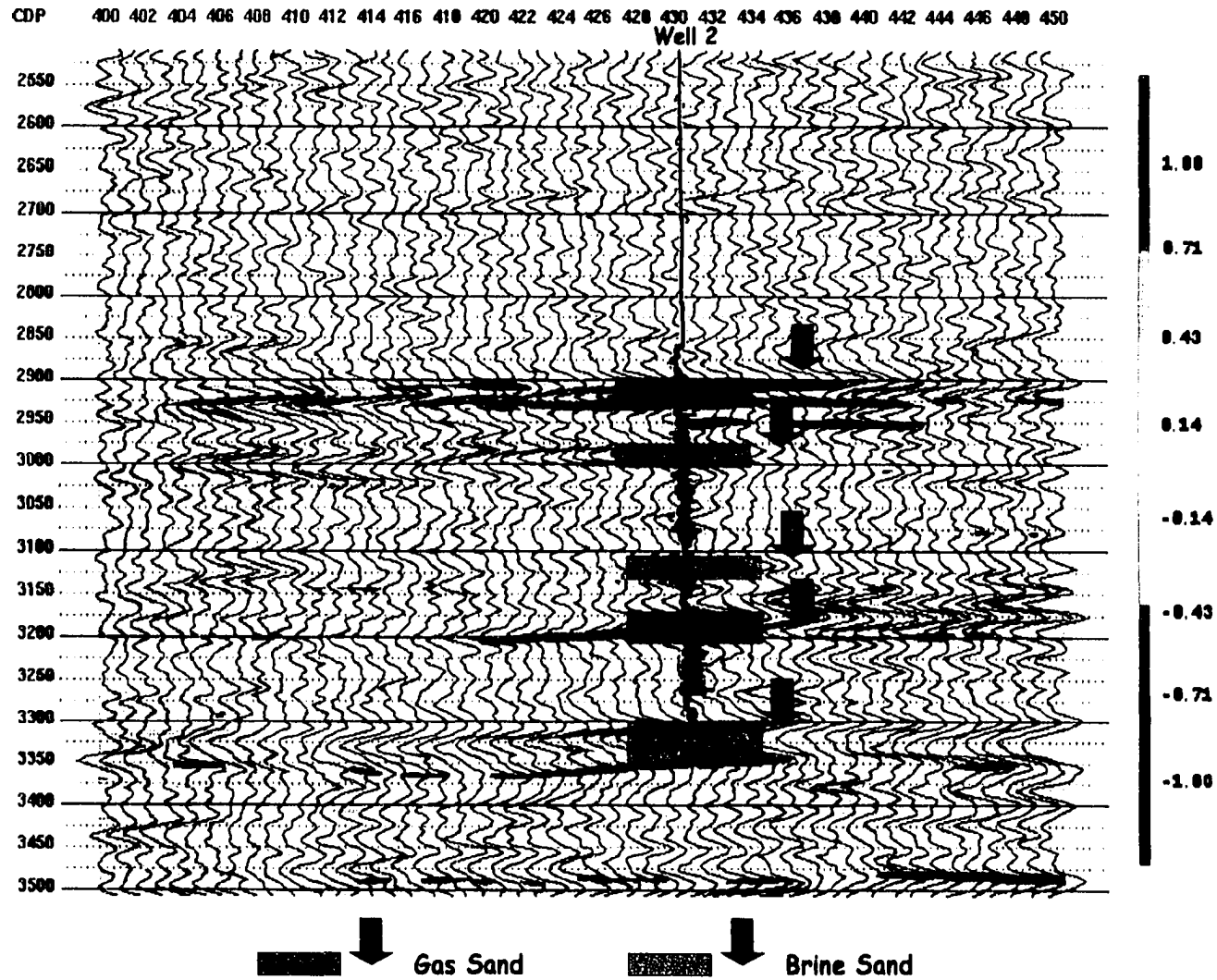


Figure 7.6d. Scaled Poisson's ratio change or fluid factor section for seismic line 2. Known brine and gas intervals are indicated in blue and red, respectively.

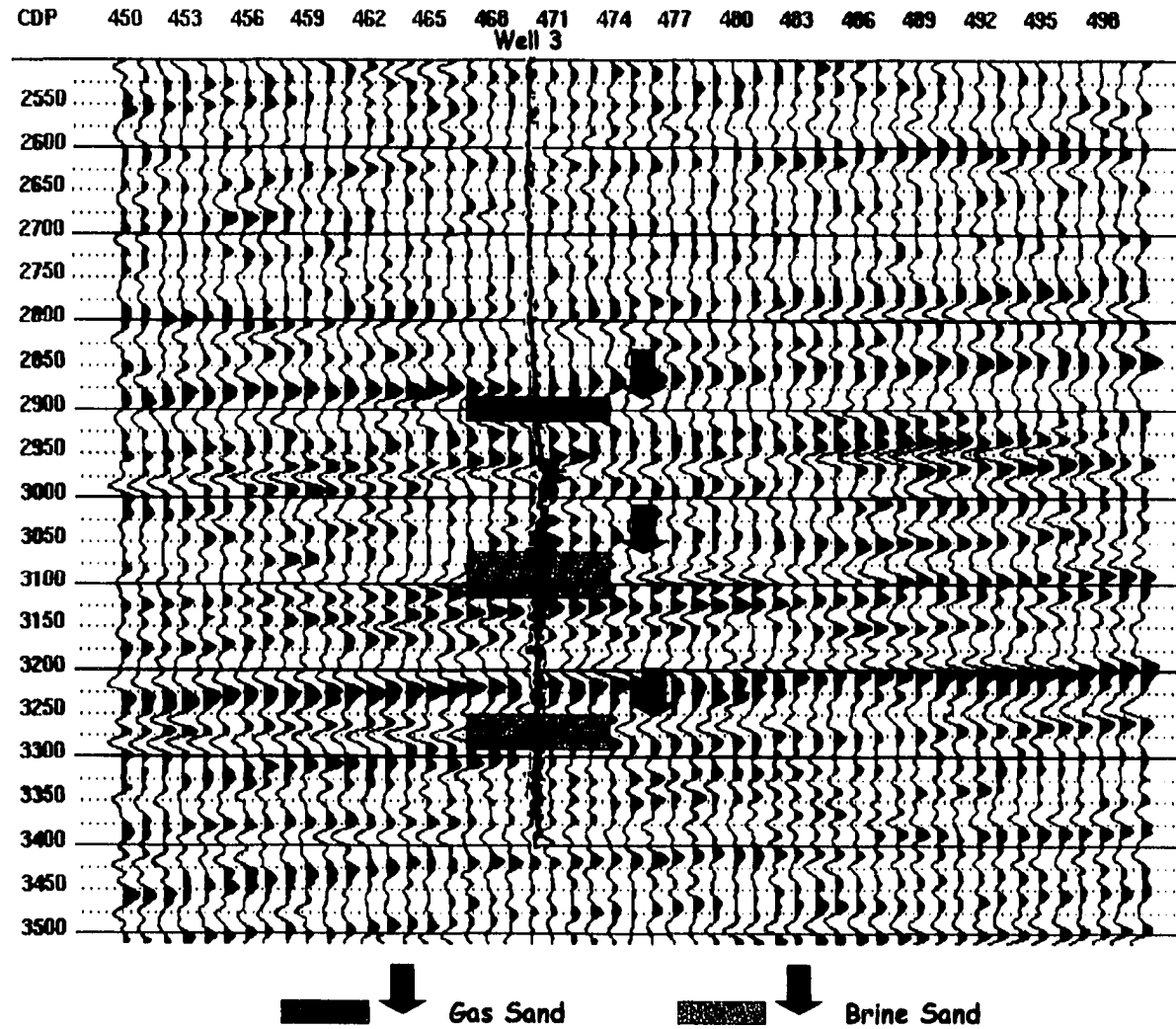


Figure 7.7a. AVO intercept (A) section for seismic line 3. Known gas intervals are shown in red, whereas brine zones are indicated in blue.

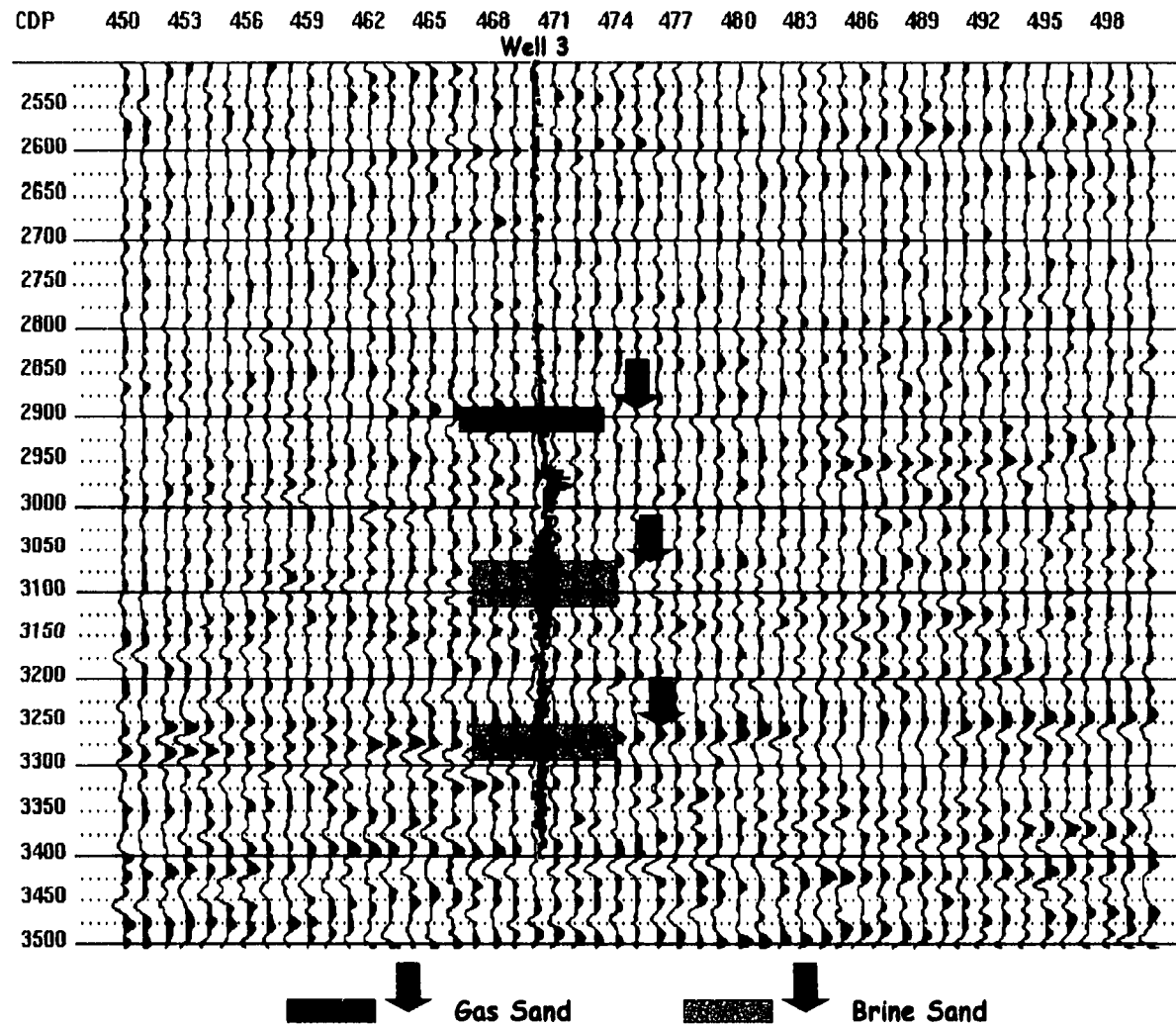


Figure 7.7b. AVO gradient (B) section for seismic line 3. Known gas zones are highlighted in red, whereas brine intervals are shown in blue.

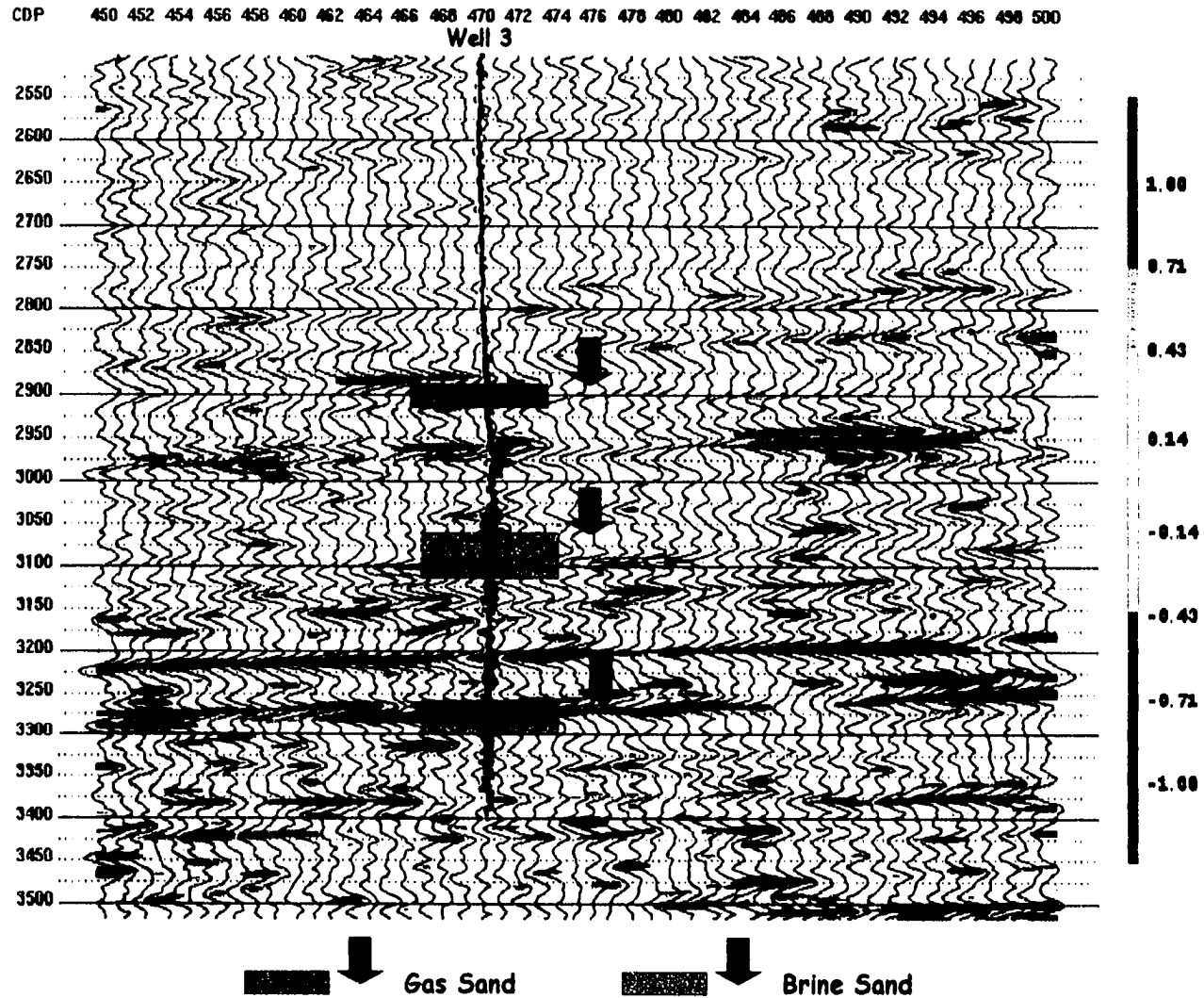


Figure 7.7c. AVO product (A*B) for seismic line 3. Known gas and brine intervals are shown in red and blue, respectively.

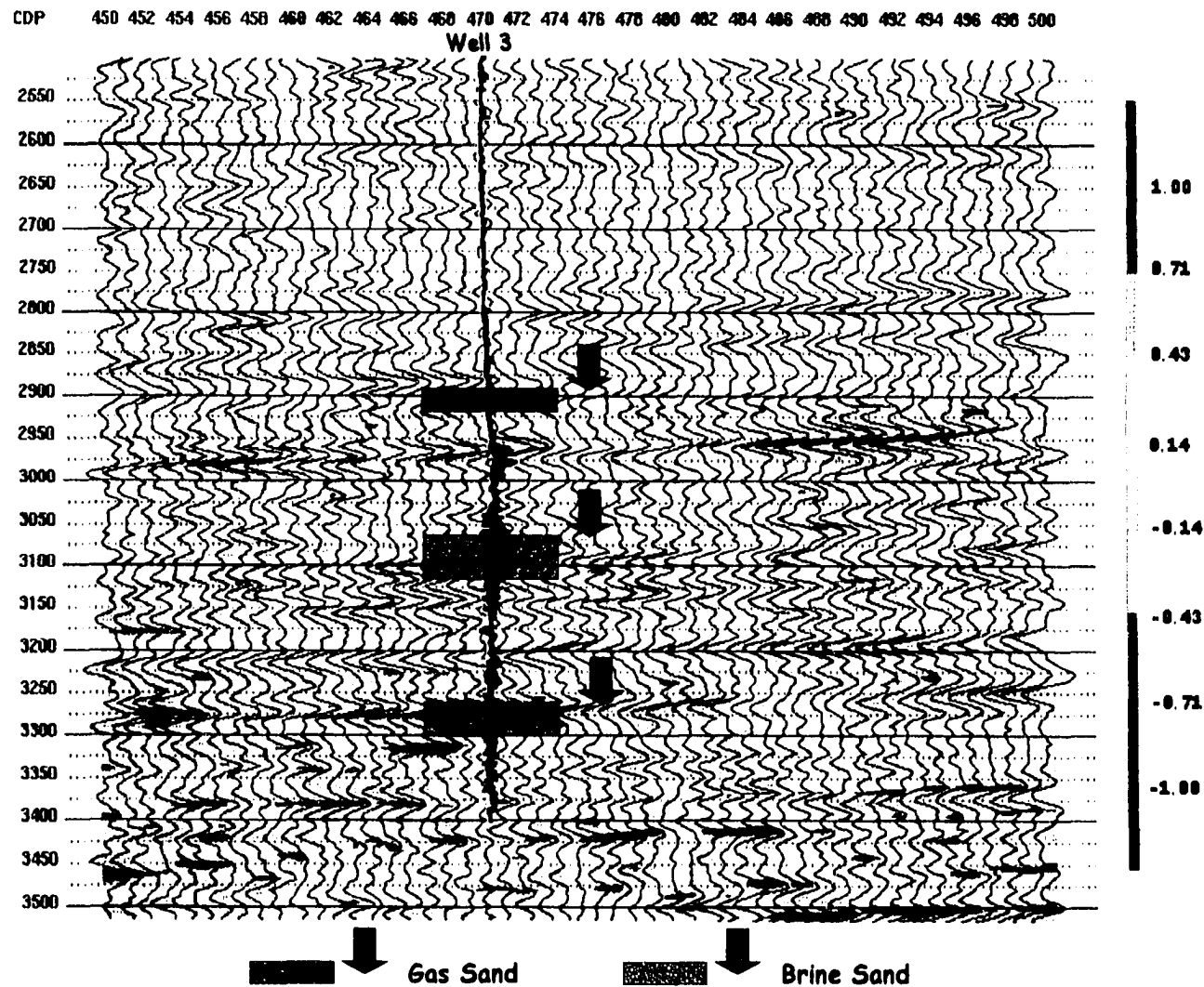


Figure 7.7d. Scaled Poisson's ratio change or fluid factor section for seismic line 3. Known brine and gas intervals are indicated in blue and red, respectively.

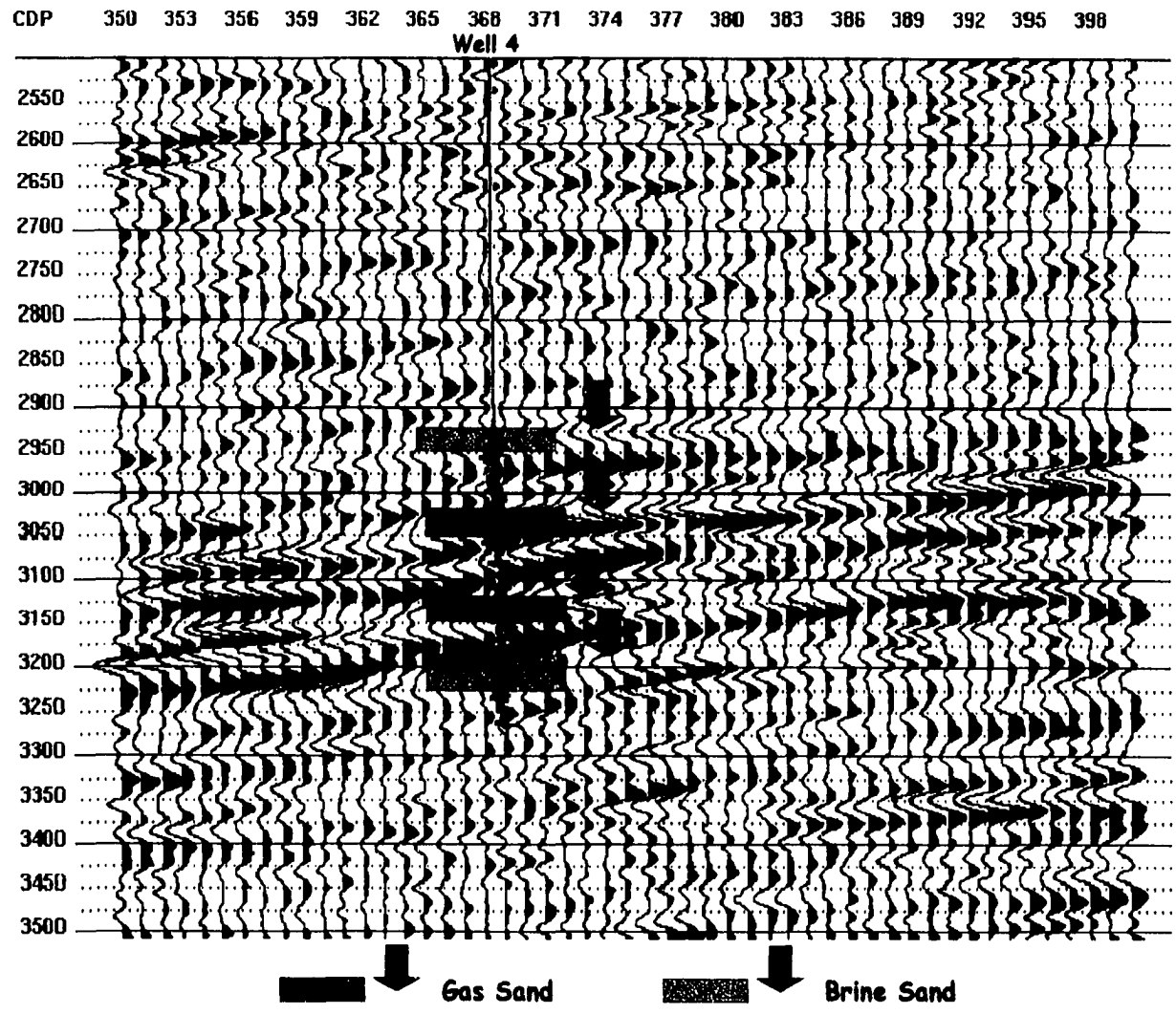


Figure 7.8a. AVO intercept (A) section for seismic line 4. Known gas and brine intervals are shown in red and blue, respectively.

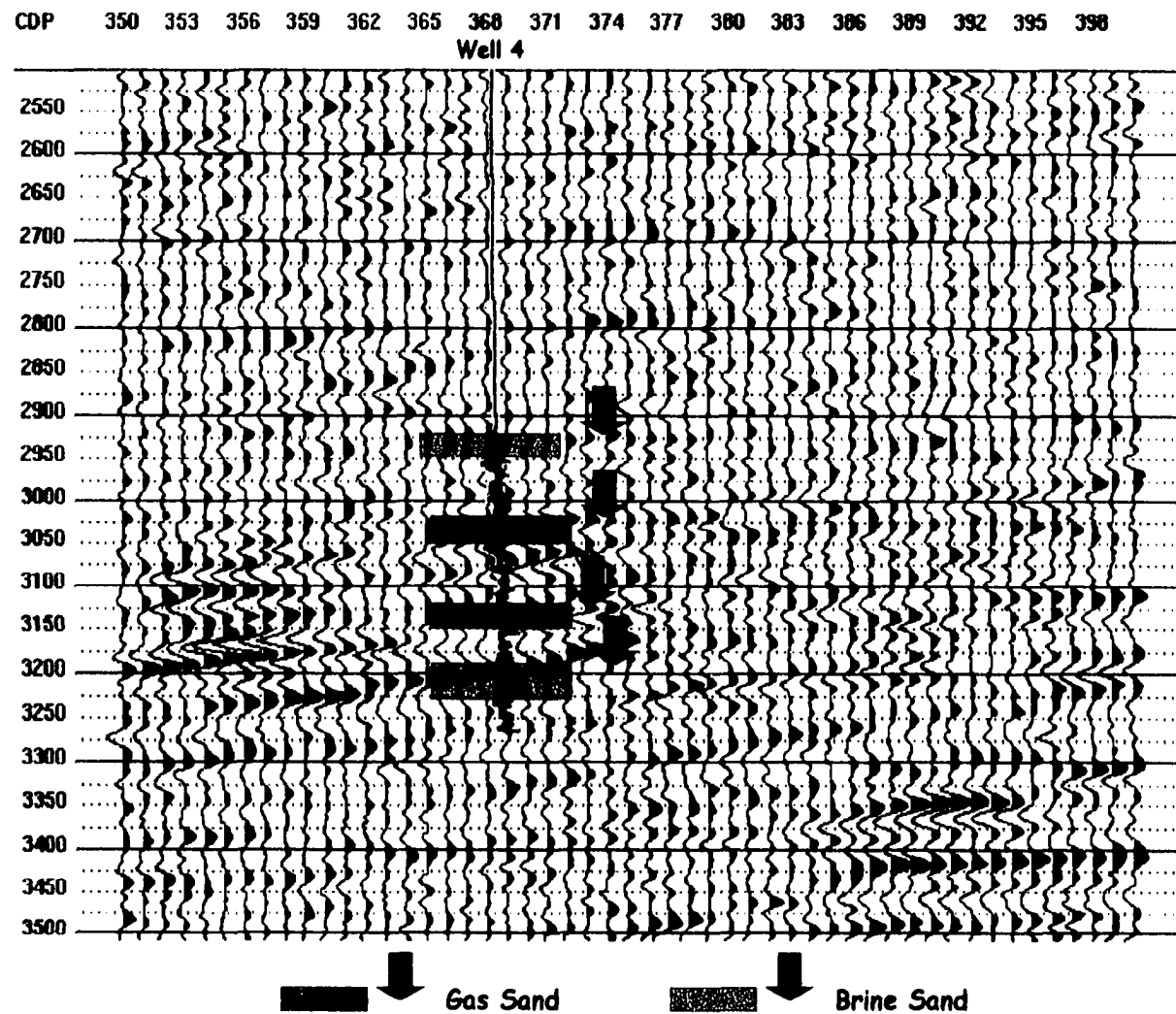


Figure 7.8b. AVO gradient (B) section for seismic line 4. Known brine and gas zones are indicated in blue and red, respectively.

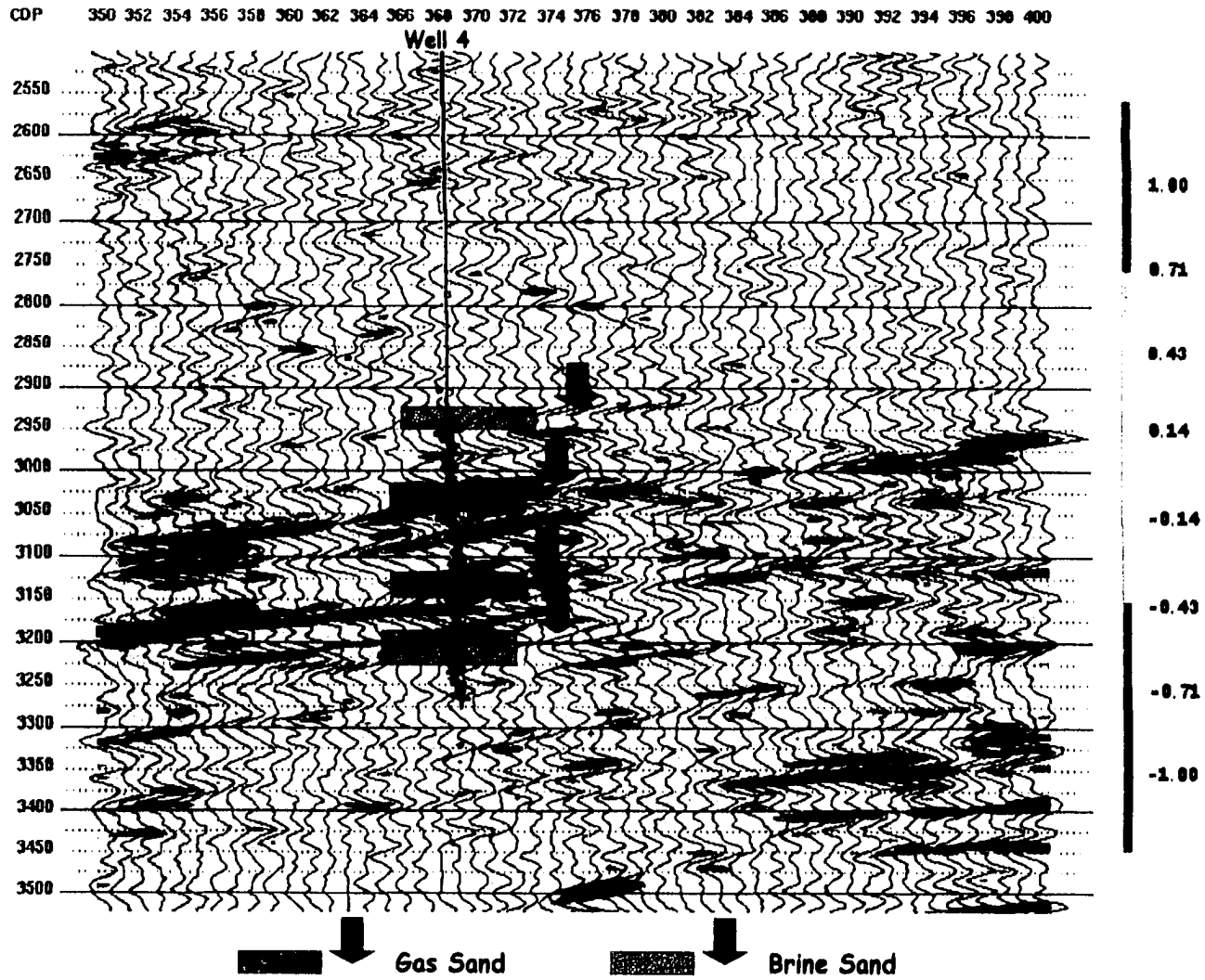


Figure 7.8c. AVO product (A*B) section for seismic line 4. Known brine and gas intervals are highlighted in blue and red, respectively.

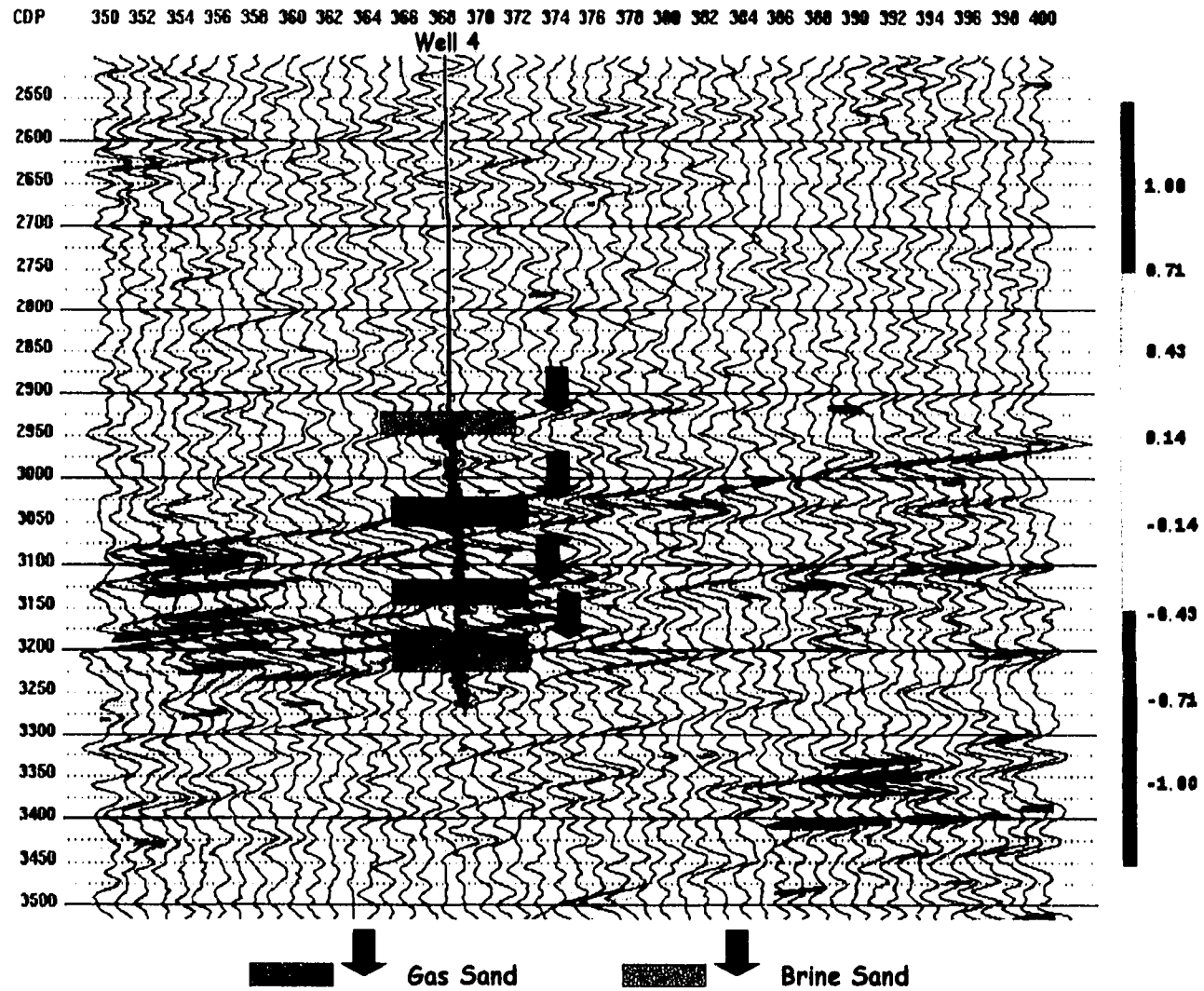
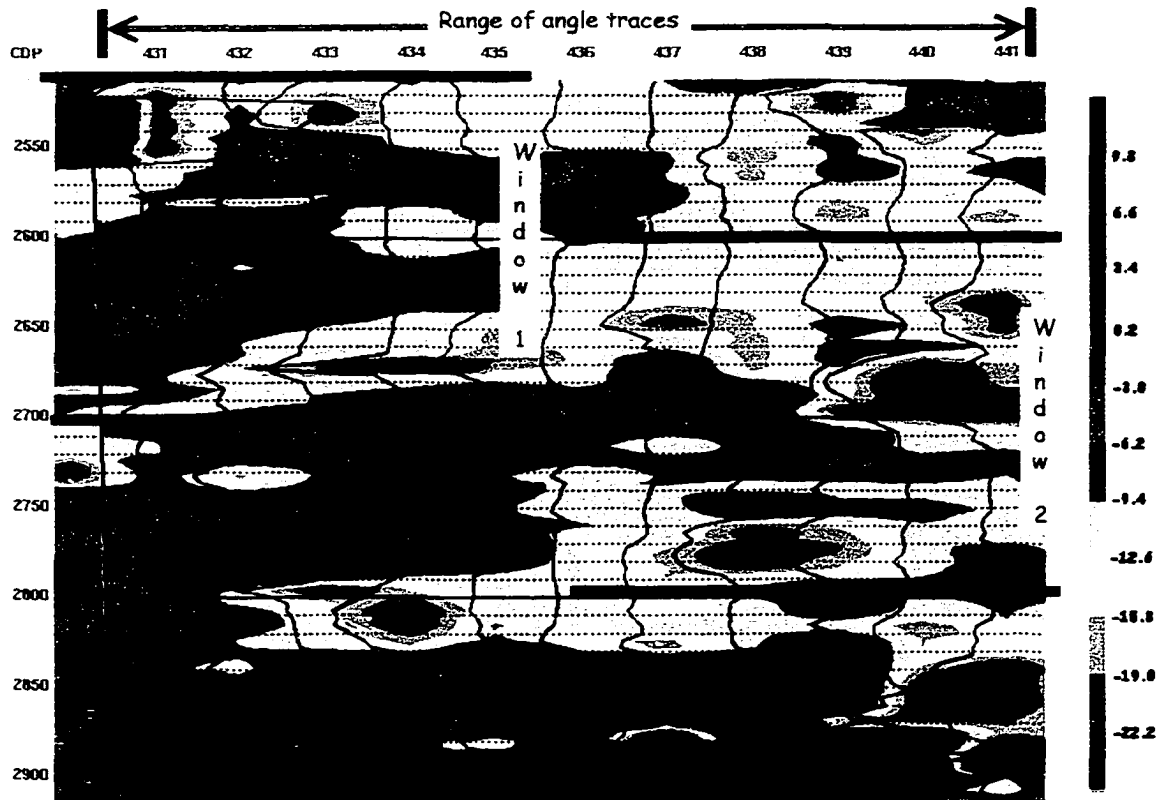


Figure 7.8d. Scaled Poisson's ratio or fluid factor section for seismic line 4. Known gas and brine intervals are indicated in red and blue, respectively.

7.4 Polarization Attributes

The extracted AVO intercept (A) and gradient (B) traces for each seismic line are used to compute the polarization attributes: (1) polarization angle (ϕ), (2) polarization angle difference ($\Delta\phi$), (3) AVO strength (L), (4) polarization product (product of AVO strength and polarization angle difference) ($L\Delta\phi$), and square of linear-correlation coefficient (r^2). A 28-msec sliding time window is chosen as the size of the window analysis along the traces. Since the dominant frequency of the seismic data is approximately 30 Hz, the time window for the computation is roughly $0.85 T$, a value within the suggested range (Keho, 2000). T is the seismic wave period of the data. After examining the polarization angles along many traces for each line, particularly outside of the zones of interest, a constant background polarization angle of -20 degrees (Figure 7.9 and Table 7.1) is used for the calculation of the polarization angle difference along the entire traces. The five attributes at each well location and along each seismic line are depicted in Figures 7.10 to 7.13.



The analysis windows (window 1 and 2) extend from trace 431 to trace 441

Figure 7.9. Background polarization angle determination for seismic line 2. Two time windows are considered for the analysis: (2500 - 2700 ms) and (2600 - 2800 ms). The background angle calculated at a trace from each window is the arithmetical average of the polarization angles within the window. The trace average values for each are presented in Table 7.1. After examination of the values, a rounded value of -20 degrees is chosen for the attribute computation.

Table 7. 1. Average background angle values for seismic line 2. Two time windows are considered: (2500 - 2700 ms) and (2600 - 2800 ms). The angles obtained from the other seismic lines are similar to the values presented in the table below.

Trace	Window 1 (2500 – 2700 ms)	Window 2 (2600 – 2800 ms)
431	-12.60	-22.20
432	-13.40	-12.60
433	-12.60	-13.40
434	-22.20	-15.80
435	-22.20	-15.80
436	-19.00	-12.60
437	-12.60	-16.60
438	-17.40	-15.80
439	-15.80	-22.20
440	-16.60	-12.60
441	-18.20	-17.40
Average Window Value	-16.60	-16.09

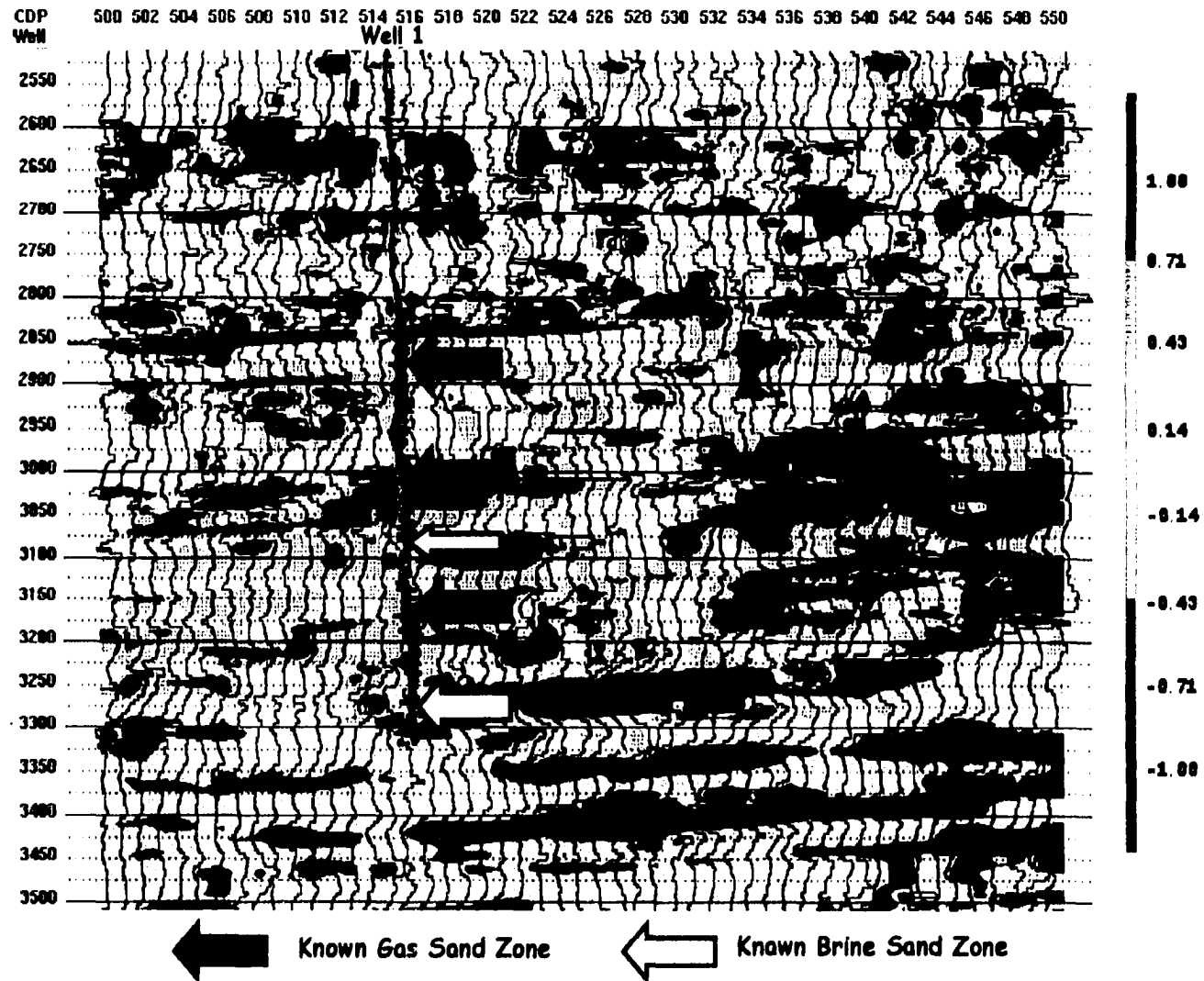


Figure 7.10a. Polarization angle (ϕ) for seismic line 1. A black arrow indicates known gas intervals, whereas a white arrow shows brine zones.

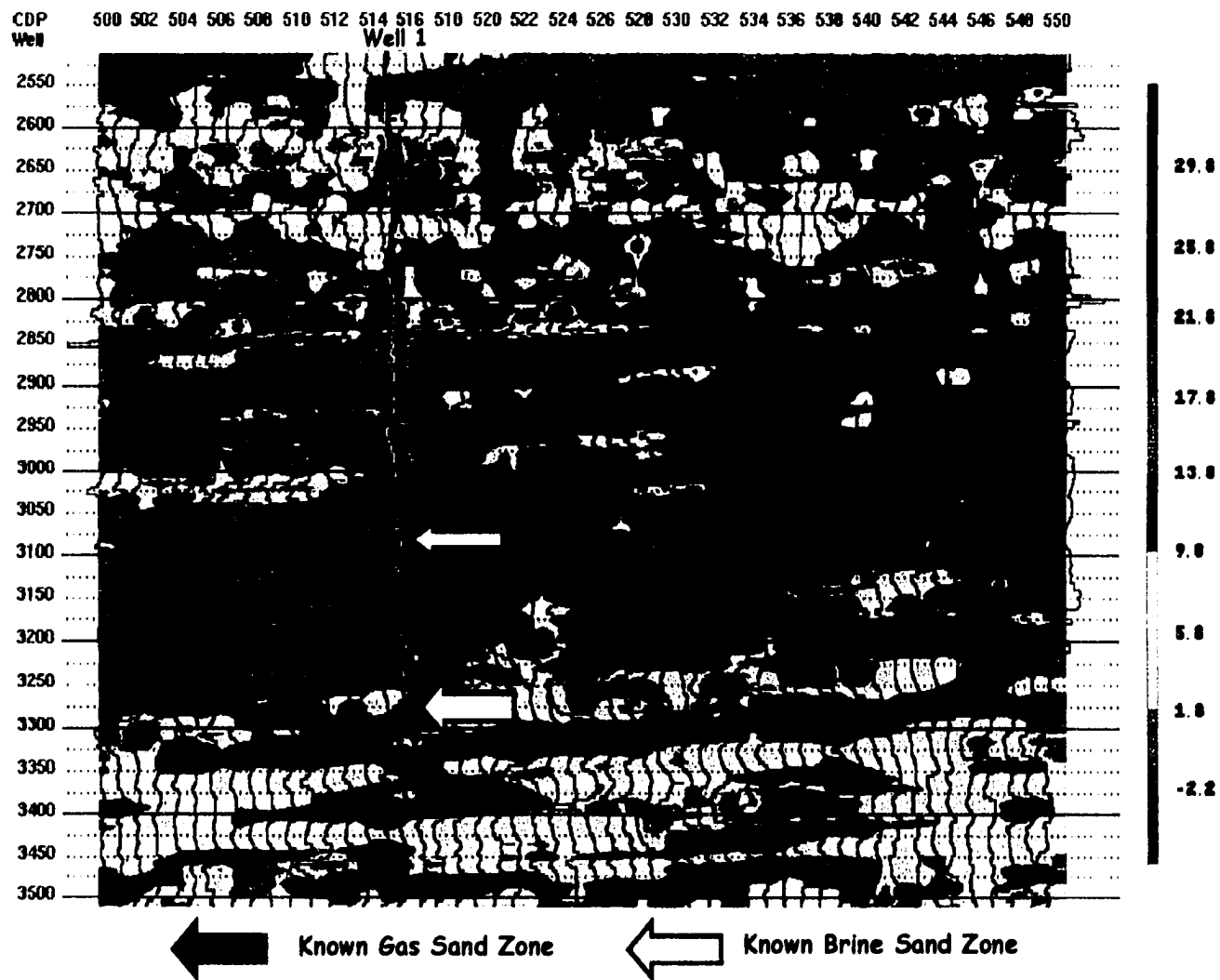


Figure 7.10b. Polarization angle difference ($\Delta\phi$) for seismic line 1. A black arrow indicates known gas zones, whereas a white arrow shows brine intervals.

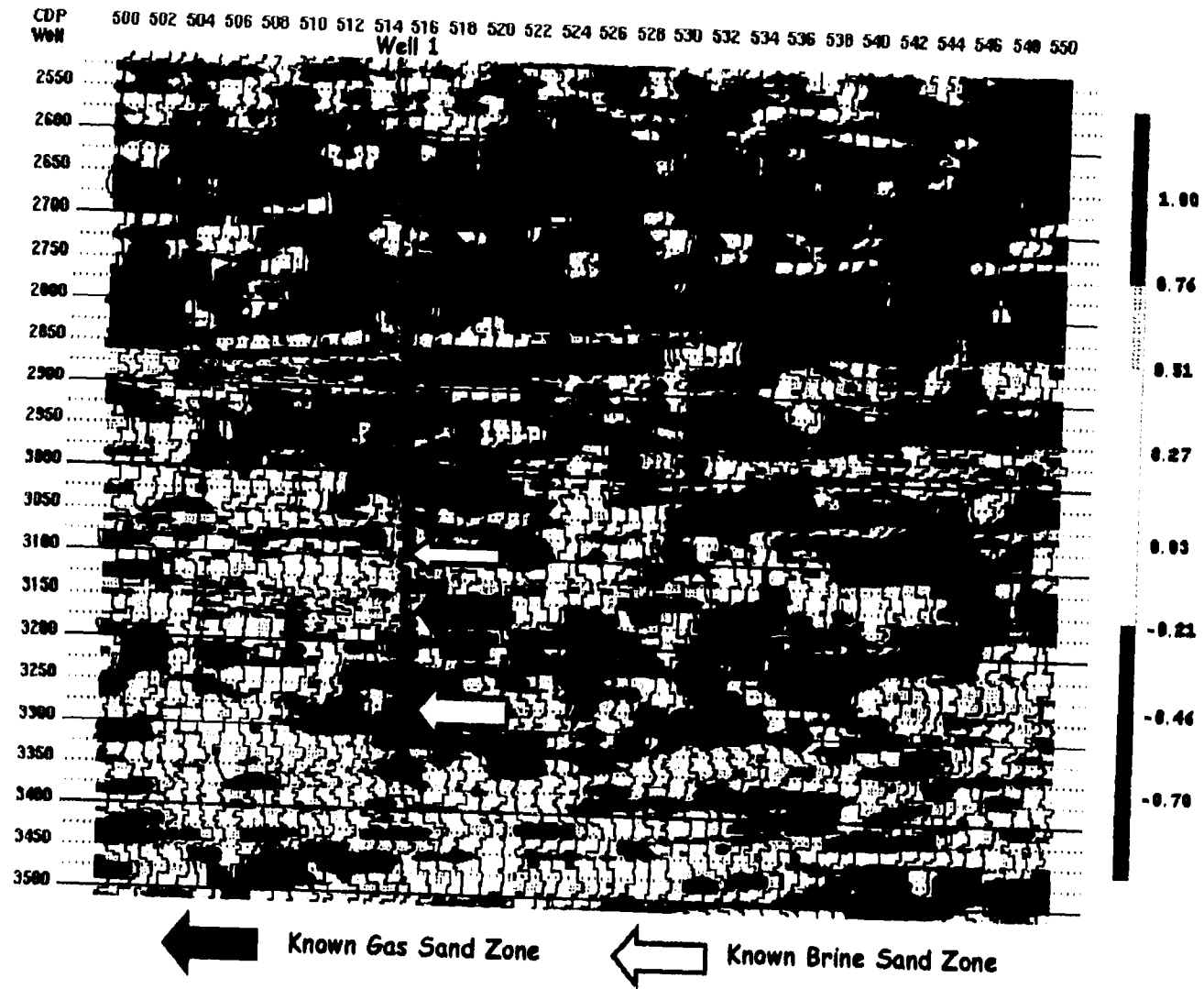


Figure 7.10c. AVO strength (L) for seismic line 1. Known gas intervals are shown by a black arrow, whereas a white arrow indicates brine intervals.

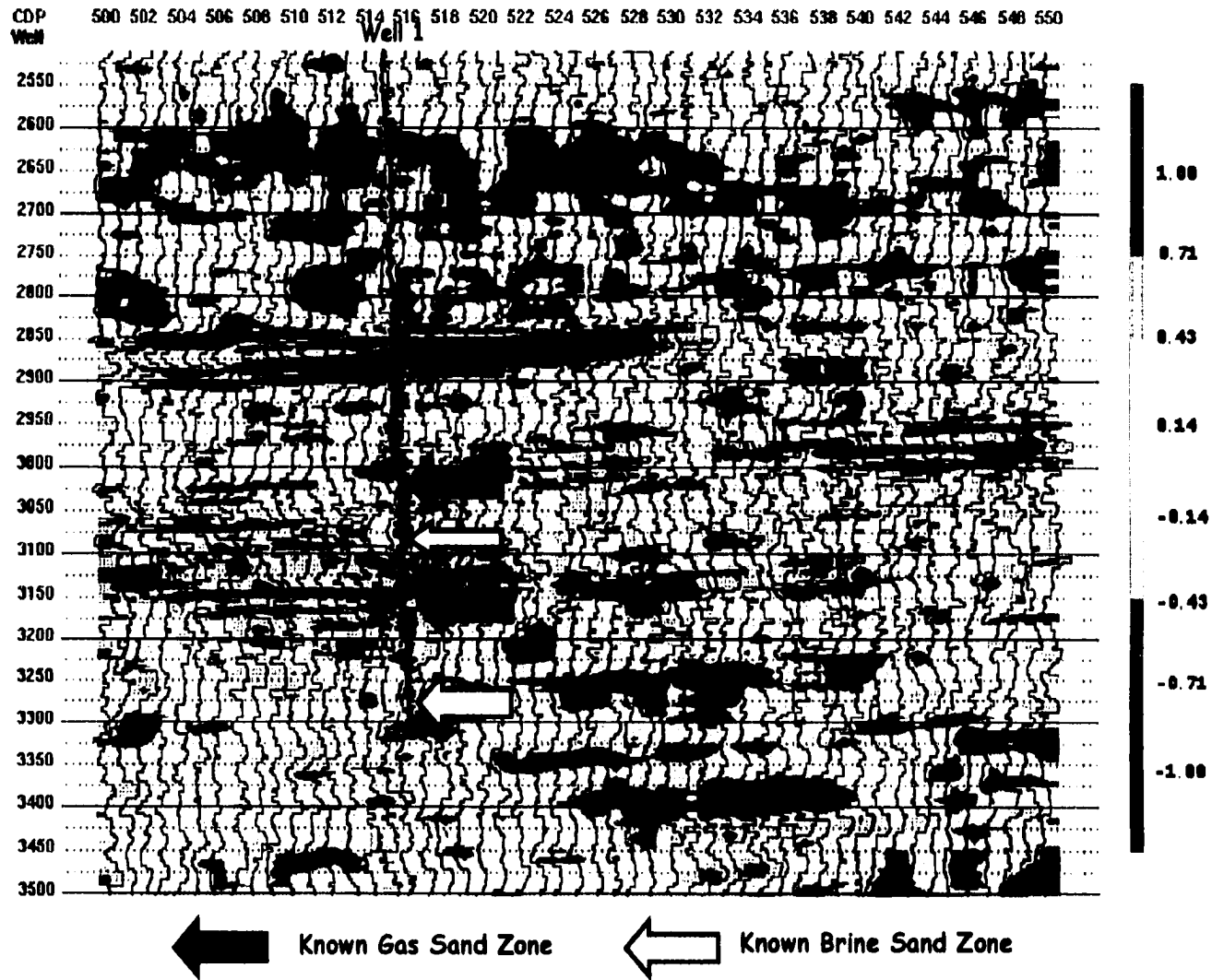


Figure 7.10d. Polarization product ($L\Delta\phi$) for seismic line 1. A black and a white arrow indicate known gas and brine intervals, respectively.

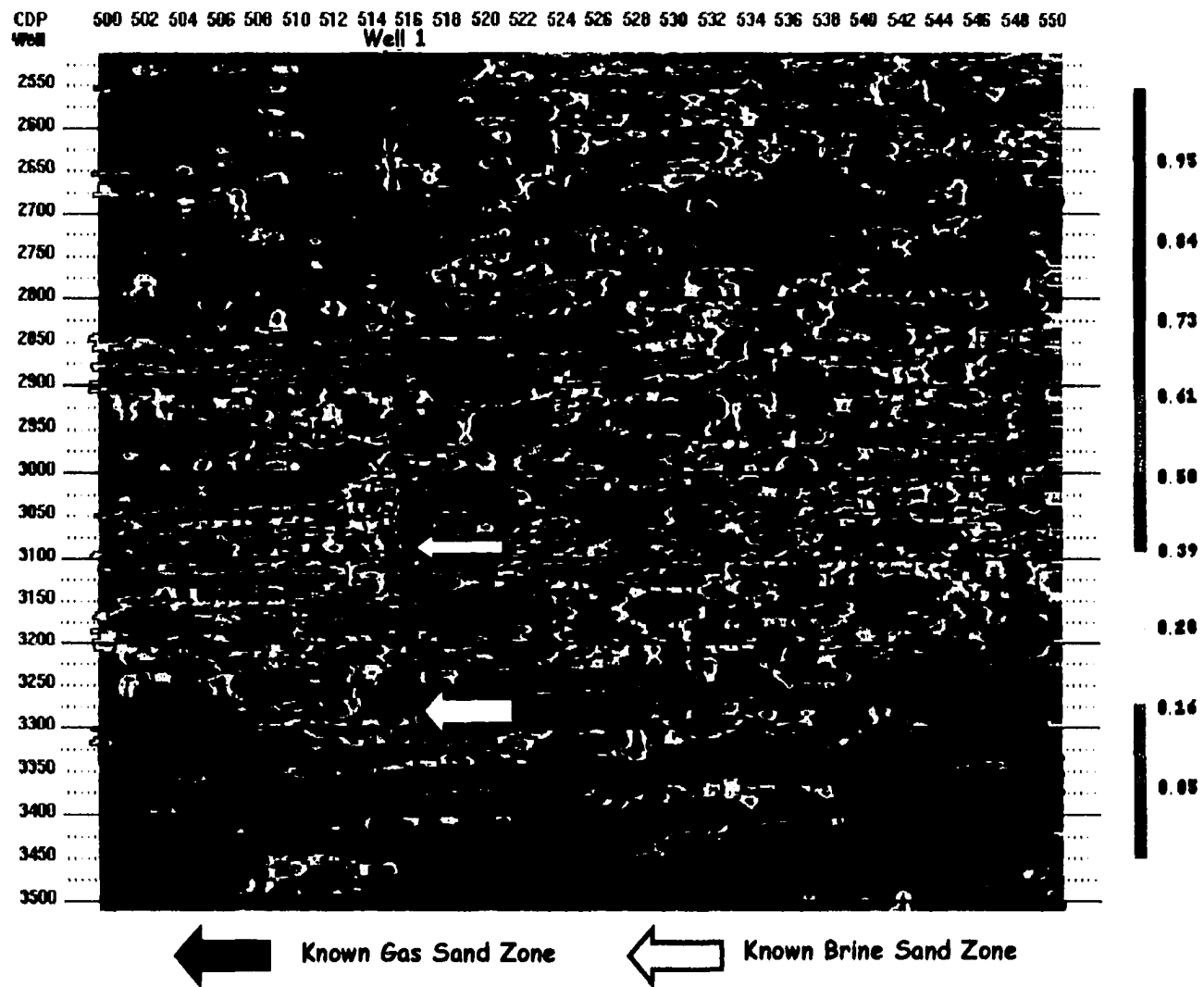


Figure 7.10 e. Square of linear-correlation coefficient (r^2) for seismic line 1. A black arrow indicates known gas sands zones, whereas a white arrow shows brine zones.

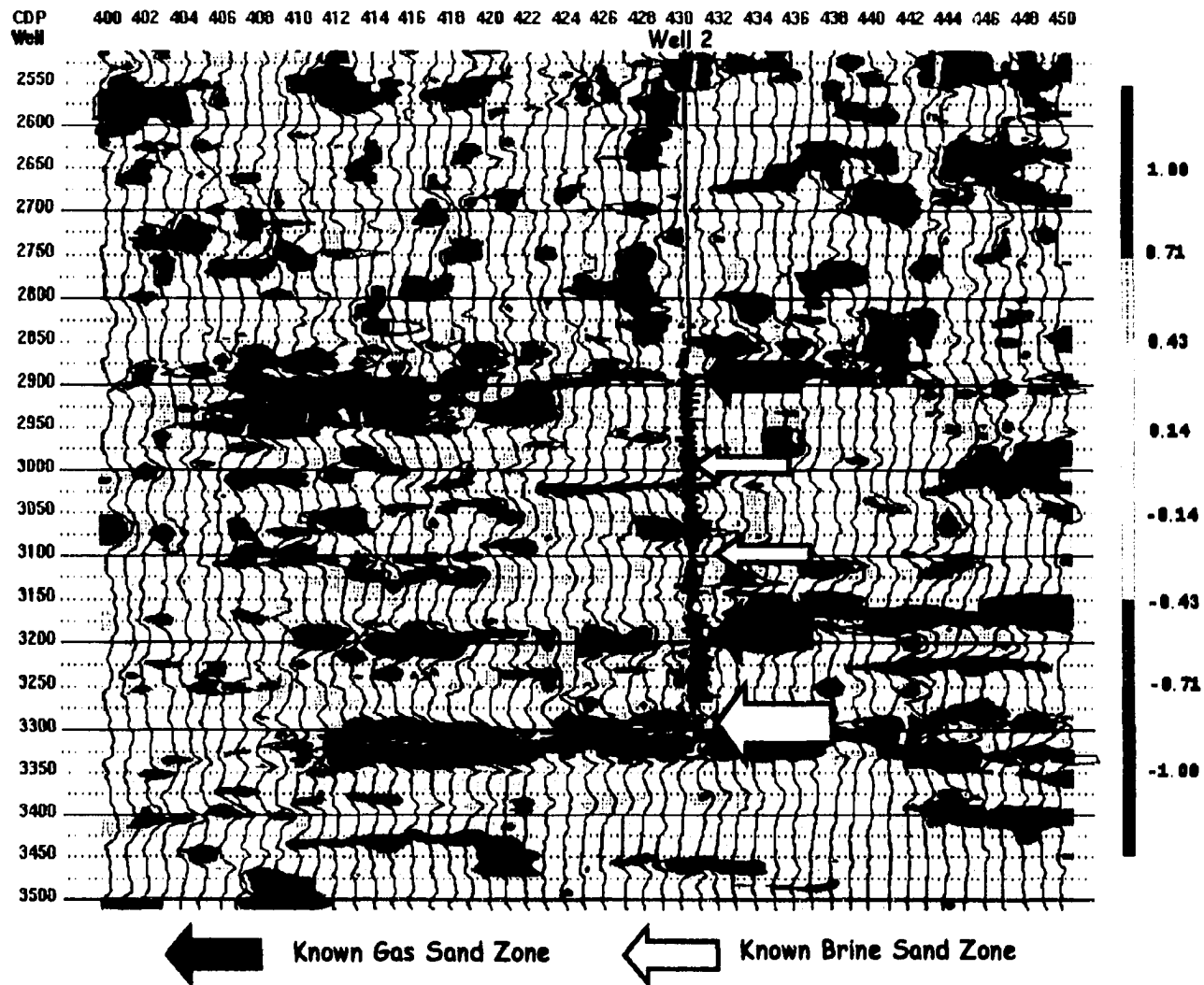


Figure 7.11a. Polarization angle (ϕ) for seismic line 2. Known gas zones are indicated by a black arrow, whereas brine intervals are shown by a white arrow.

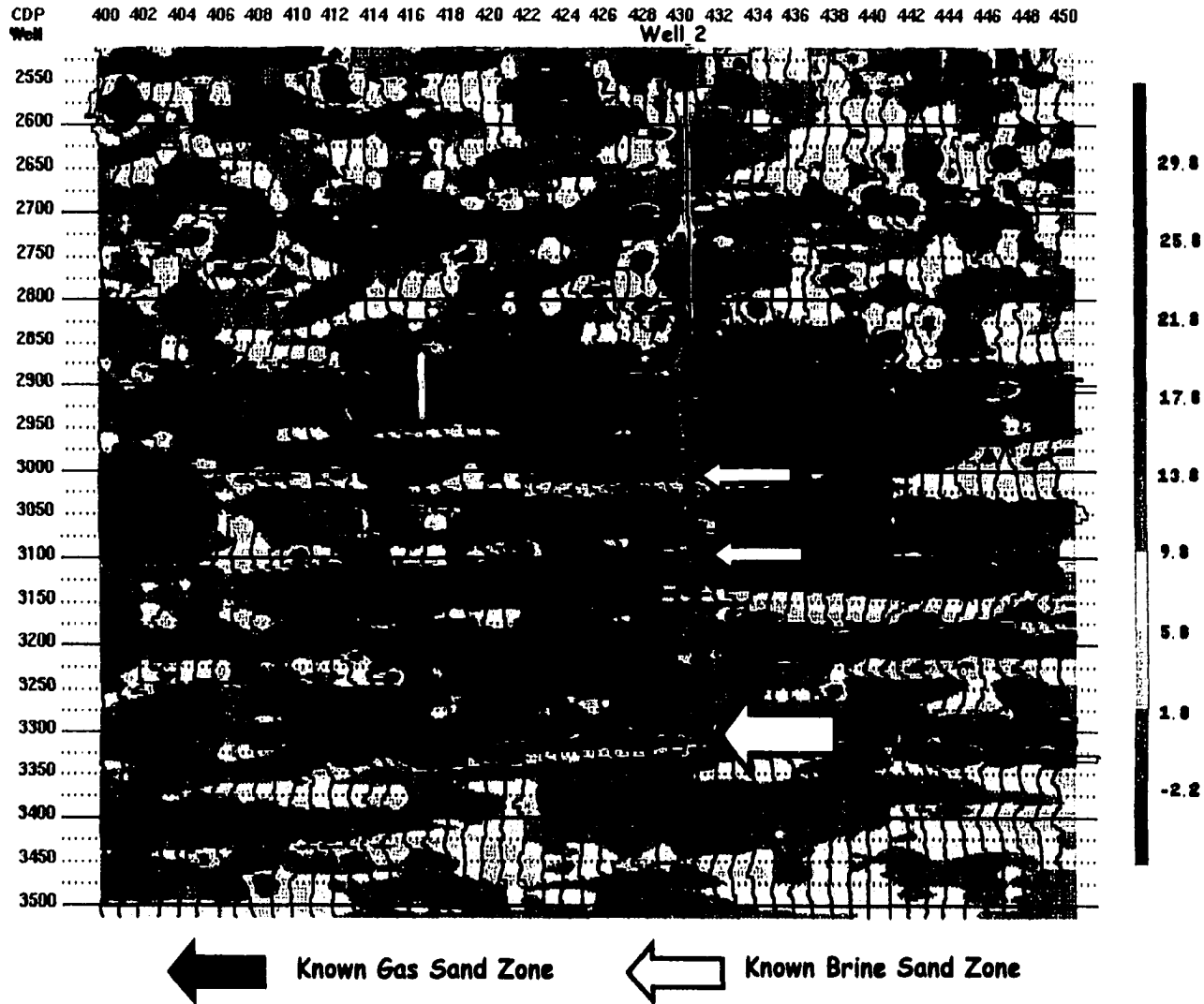


Figure 7.11b. Polarization angle difference ($L\Delta\phi$) for seismic line 2. A black arrow indicates known gas zones, whereas a white arrow shows brine intervals.

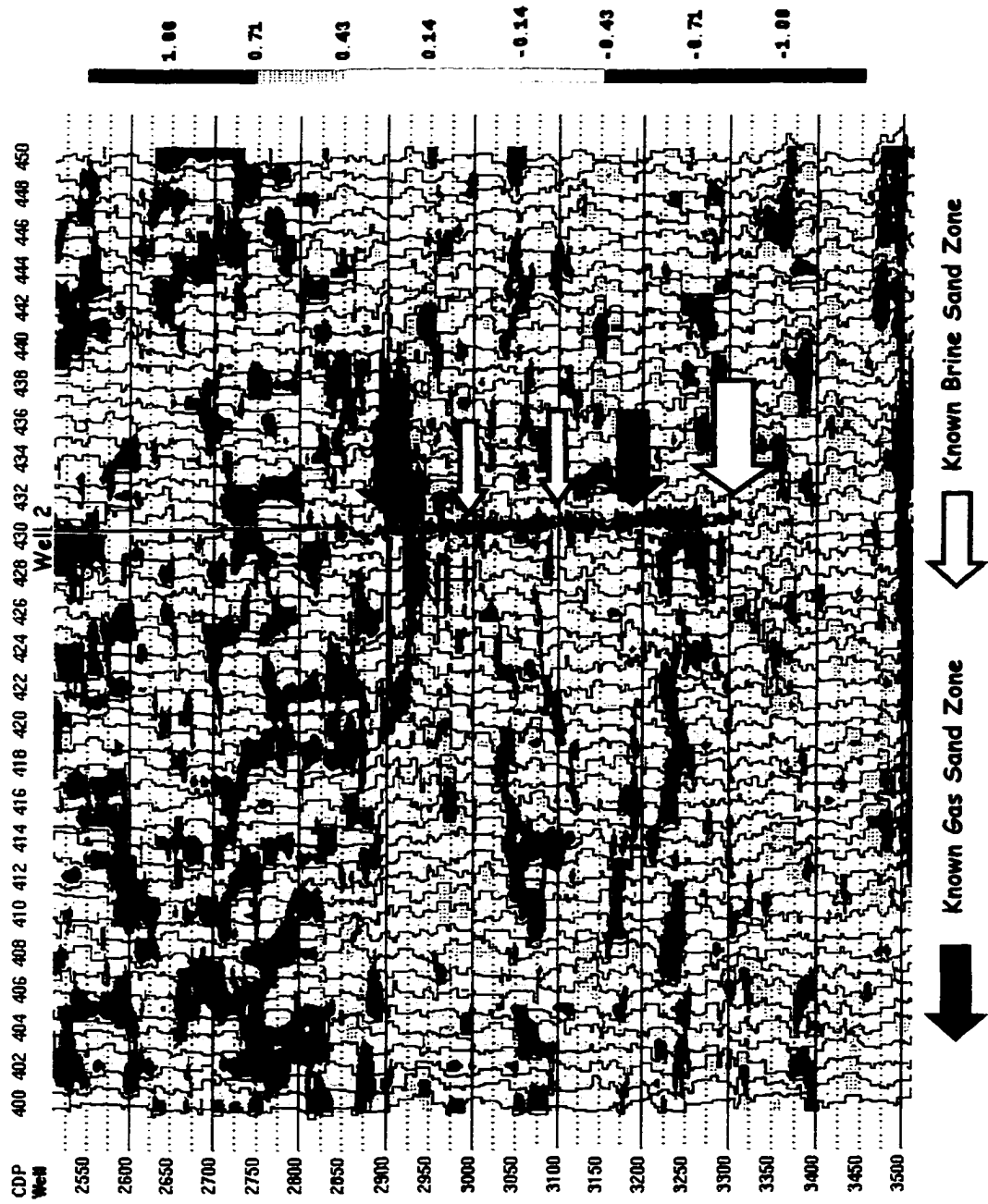


Figure 7.11c. AVO strength (L) for seismic line 2. A black arrow indicates known gas zones, whereas a white arrow shows brine intervals.

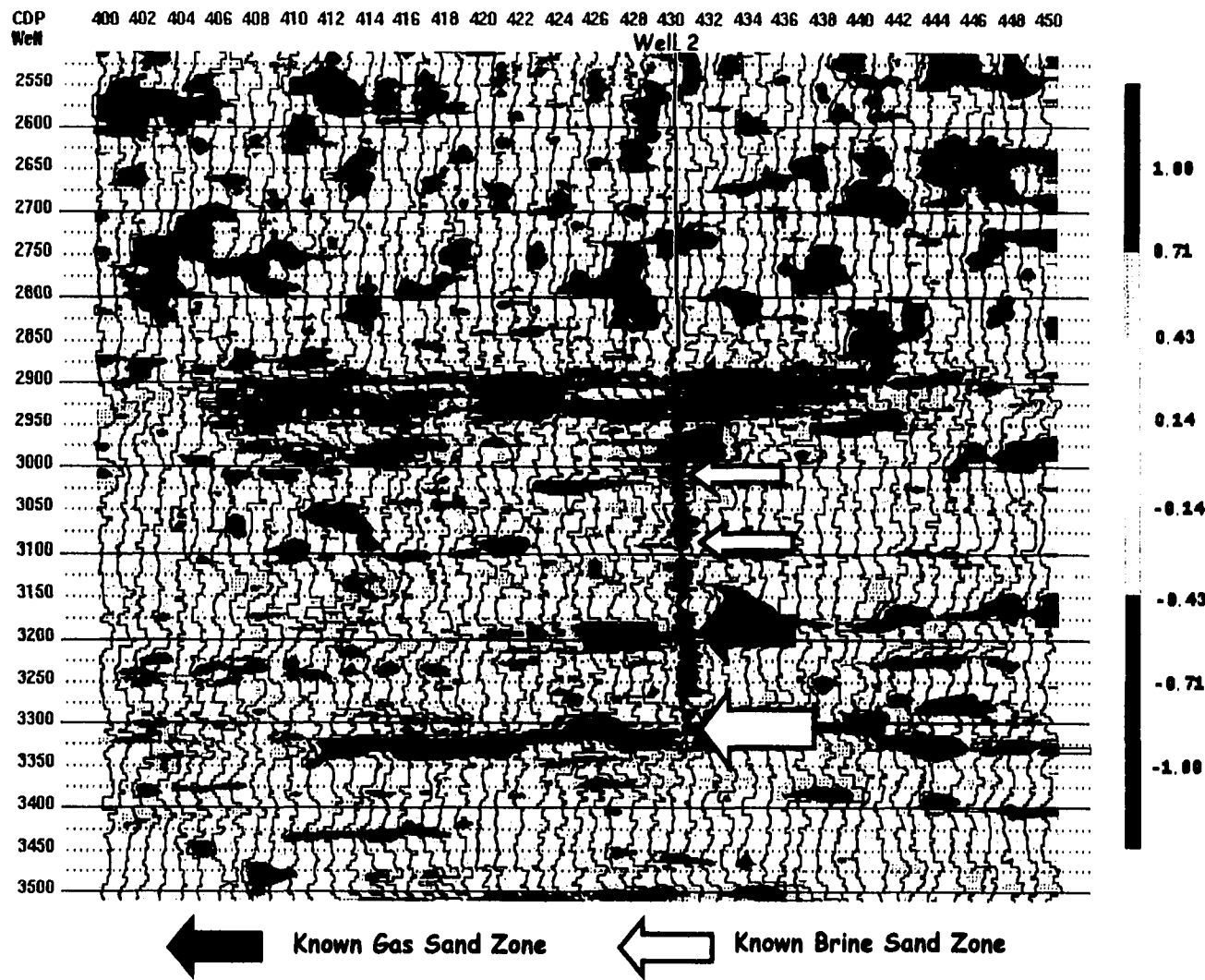


Figure 7.11d. Polarization product ($L\Delta\phi$) for seismic line 2. A black arrow shows known gas zones, whereas a white arrow indicates brine intervals.

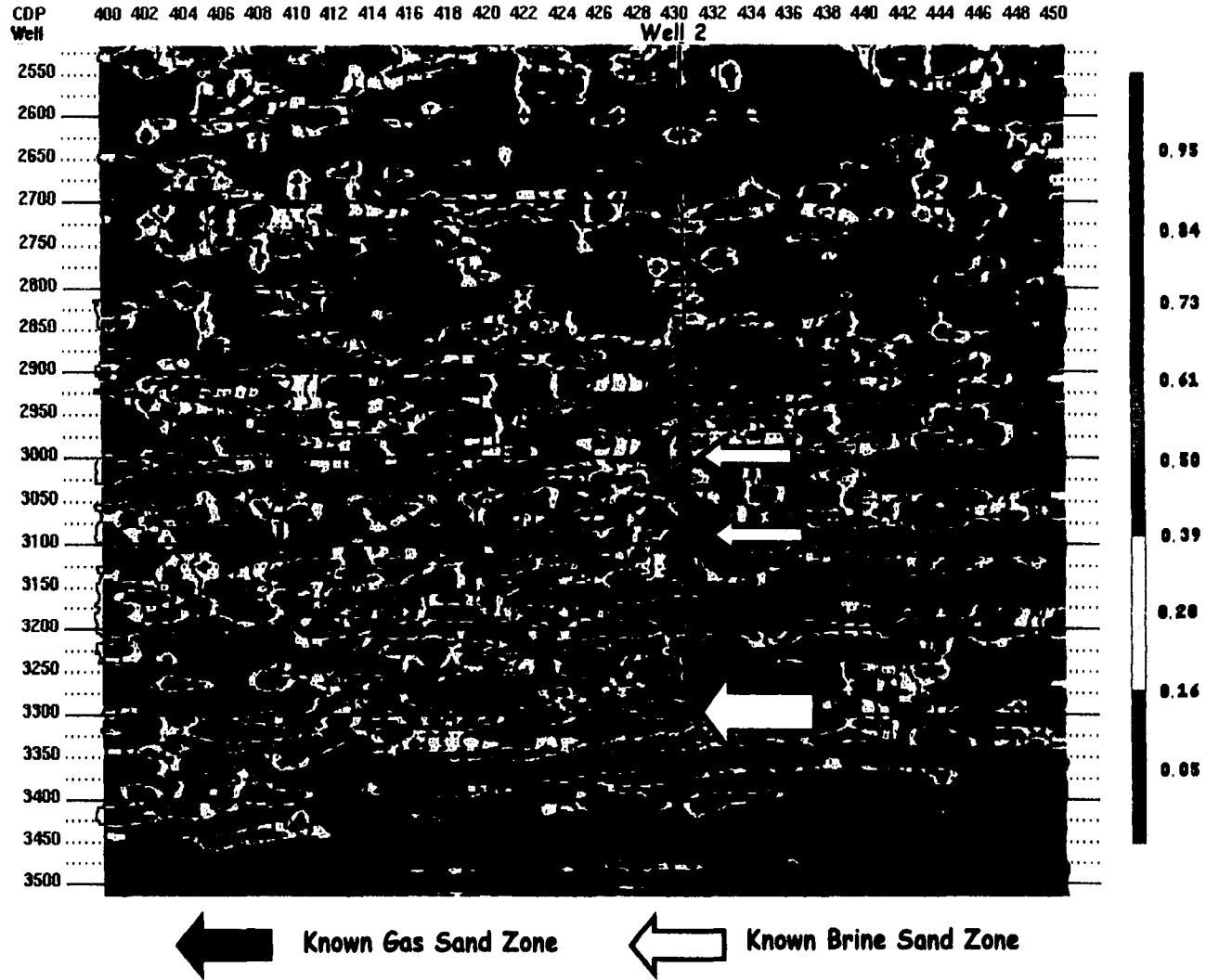


Figure 7.11e. Square of linear-correlation coefficient (r^2). A black arrow indicates known gas zones, whereas a white arrow shows brine intervals.

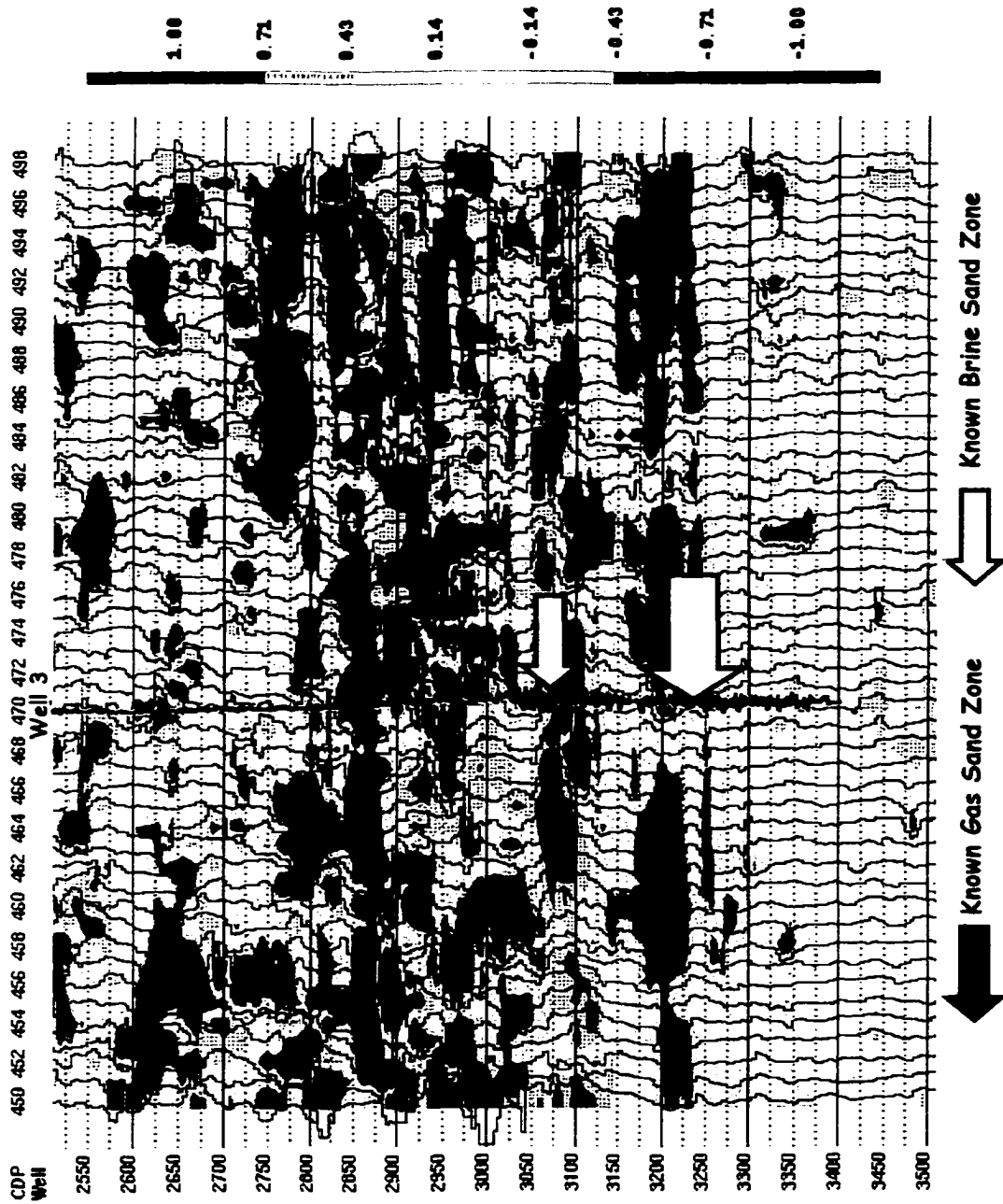


Figure 7.12a. Polarization angle (ϕ) for seismic line 3. A black arrow indicates known gas sand zones, whereas a white arrow shows brine intervals.

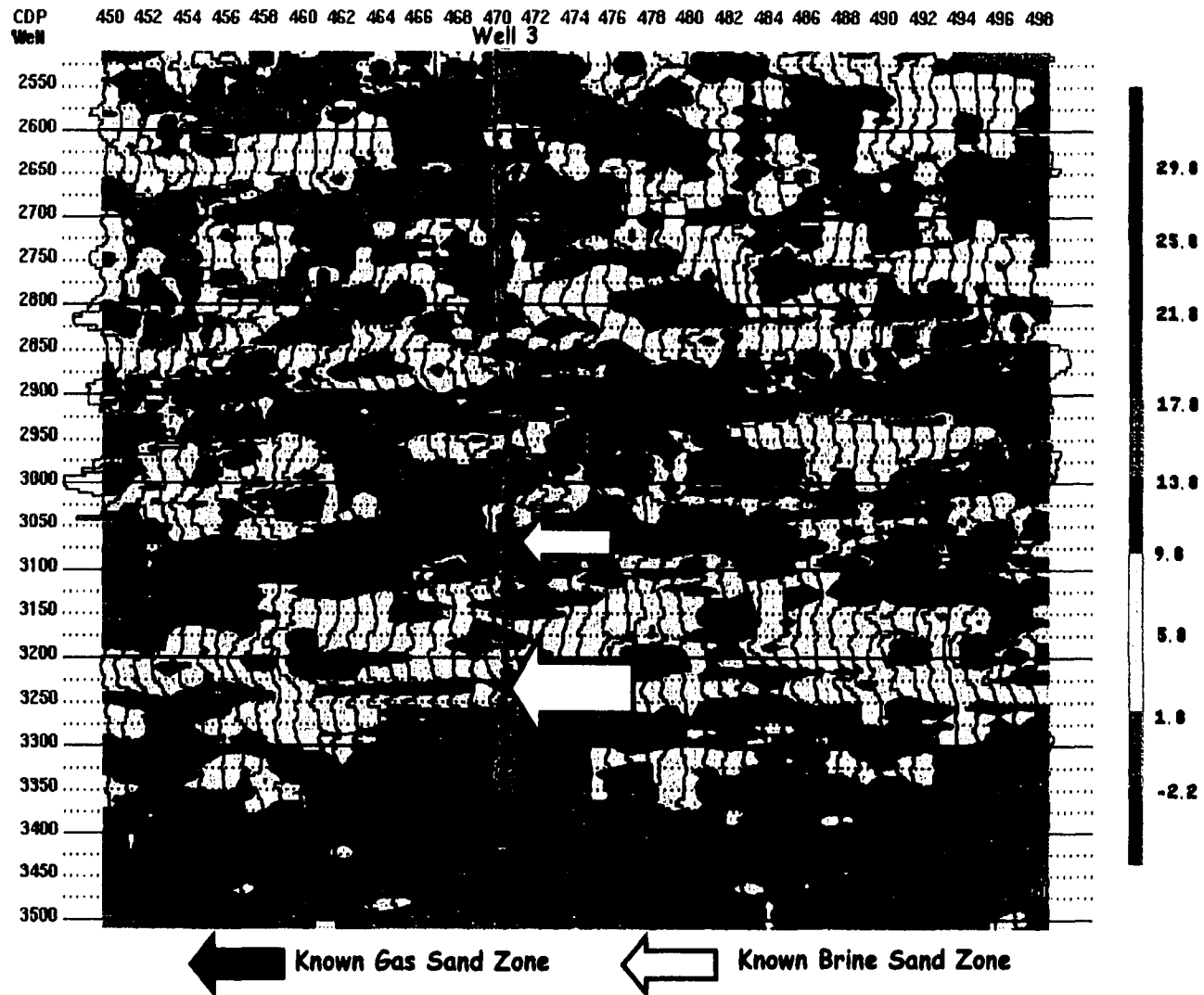


Figure 7.12b. Polarization angle difference ($\Delta\phi$) for seismic line 3. A black arrow indicates known gas intervals, whereas a white arrow shows brine sand zones.

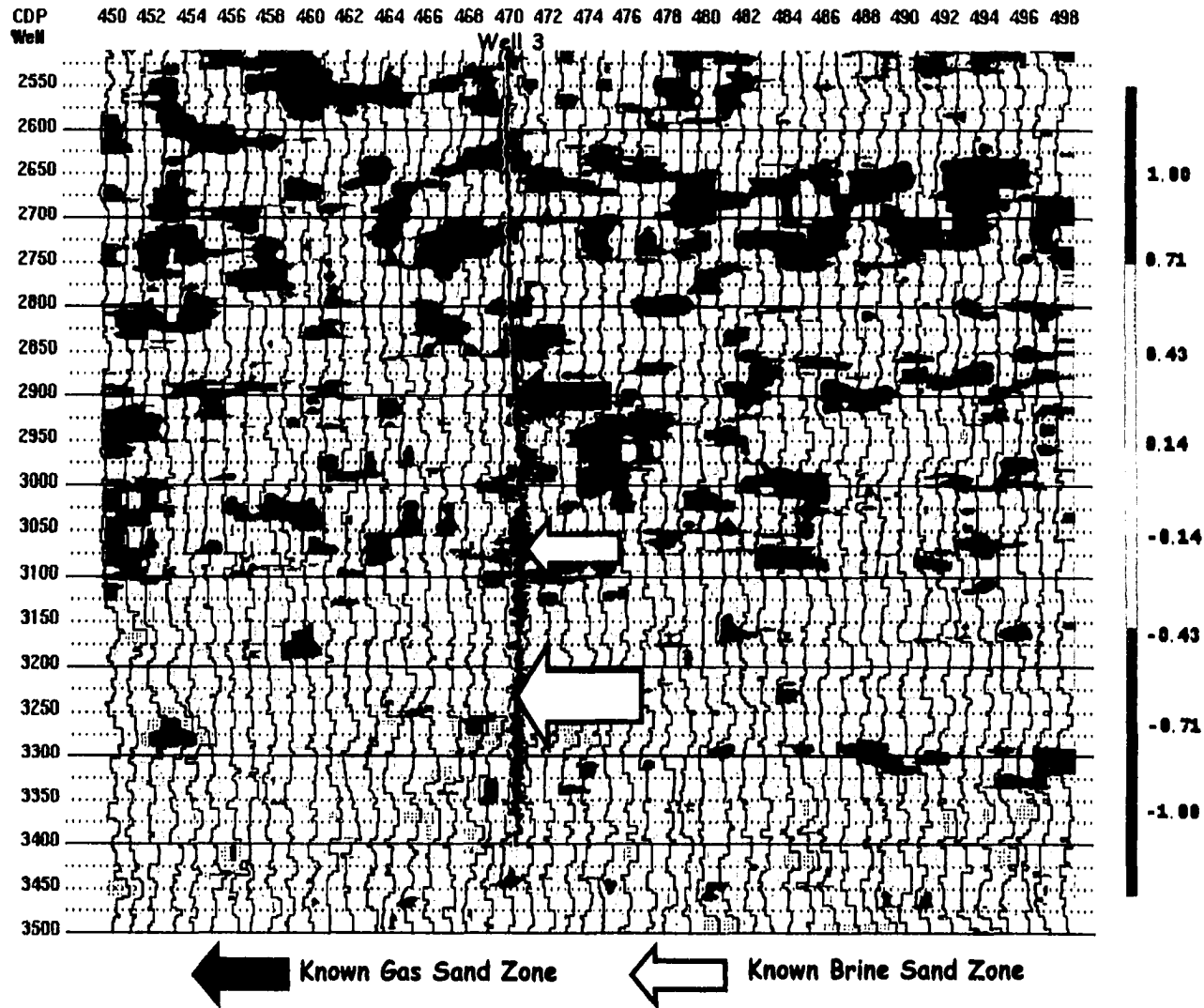


Figure 7.12c. AVO strength (L) for seismic line 3. A black arrow shows known gas zones, whereas a white arrow shows known brine intervals.

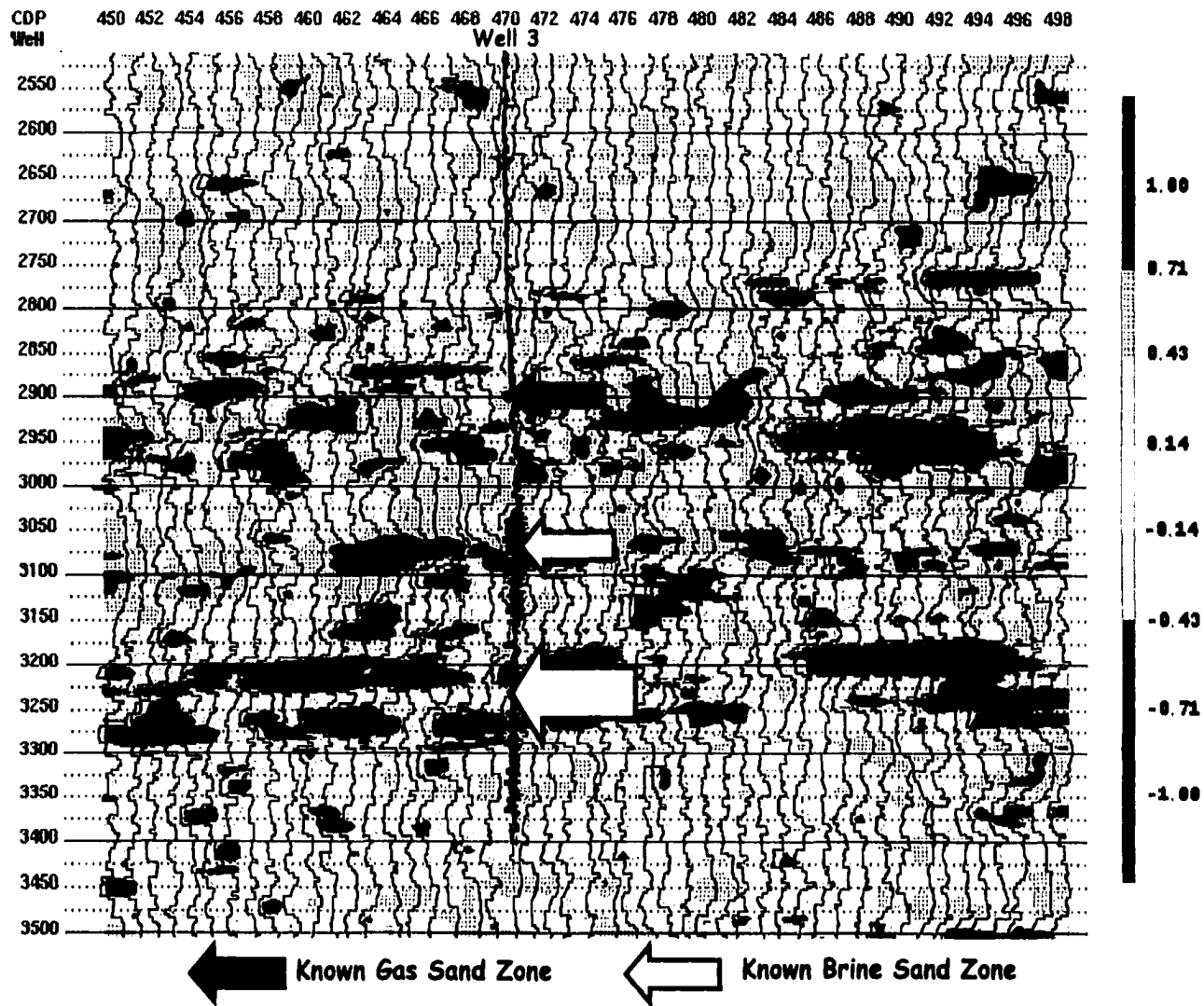


Figure 7.12d. Polarization product ($L\Delta\phi$) for seismic line 3. A black arrow indicates known gas zones, whereas a white arrow shows known brine intervals.

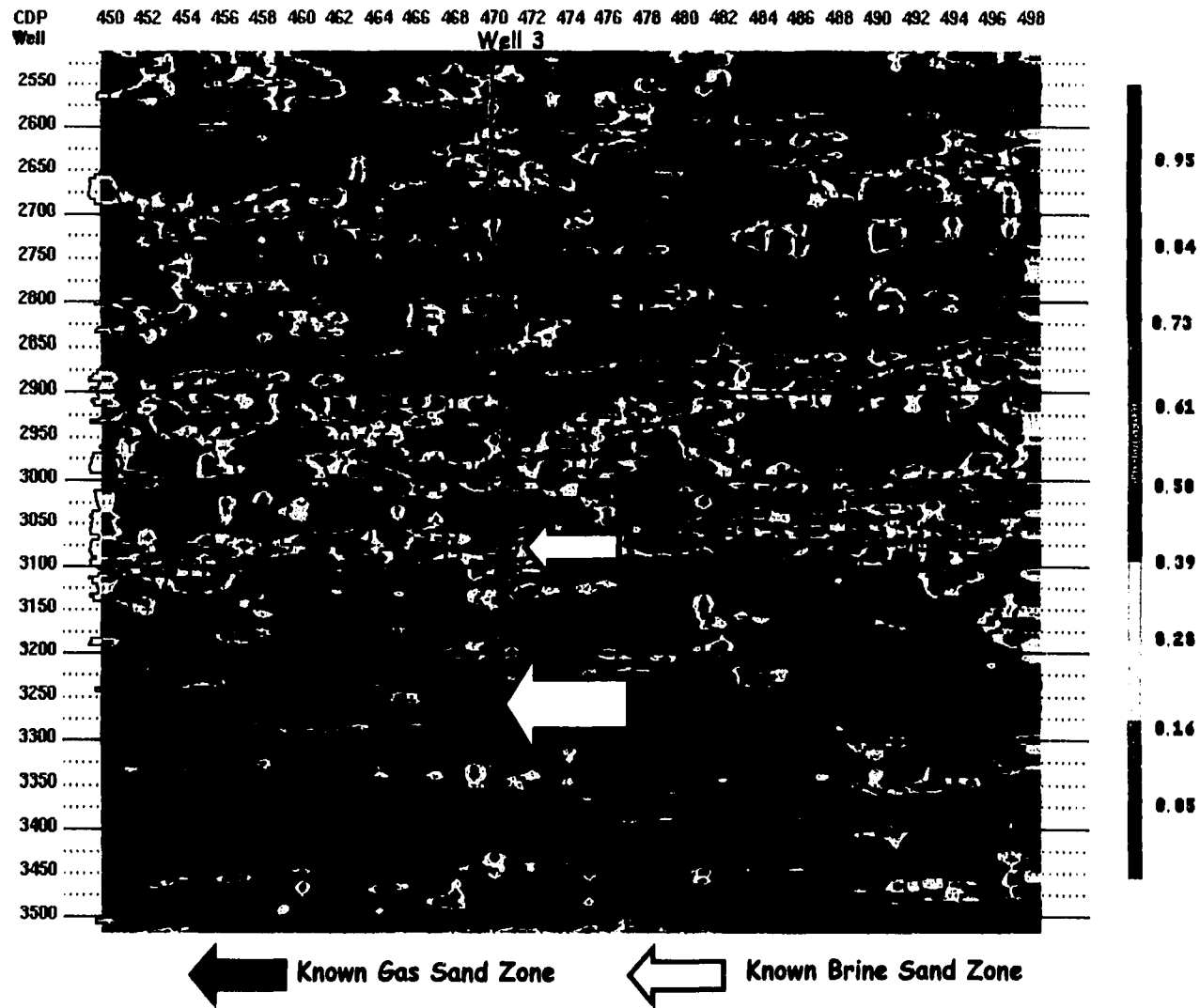


Figure 7.12e. Square of linear-correlation coefficient (r^2) for seismic line 3. A black arrow shows known gas intervals, whereas a white arrow indicates brine intervals.

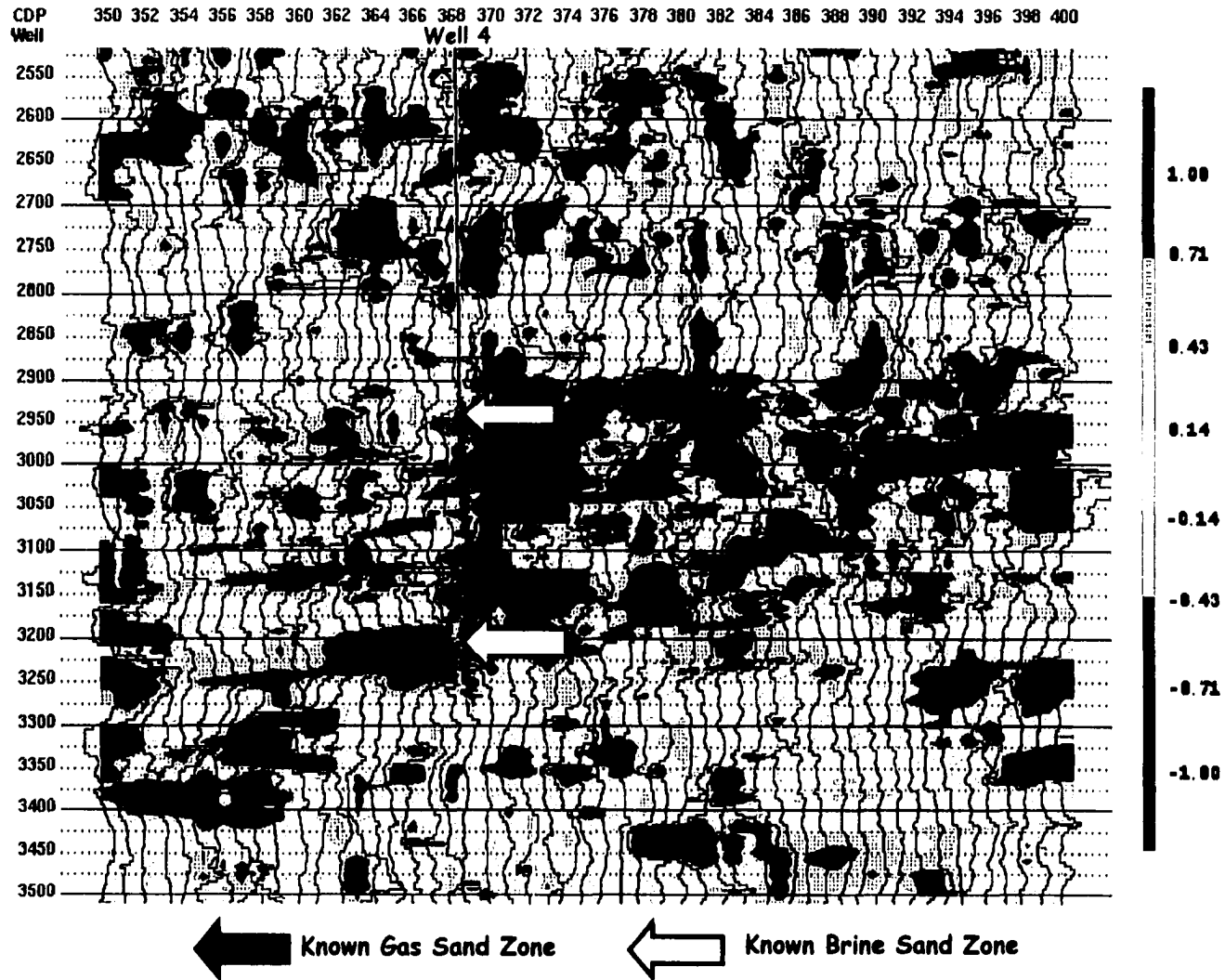


Figure 7.13a. Polarization angle (ϕ) for seismic line 4. A black arrow indicates known gas zones, whereas a white arrow shows brine intervals.

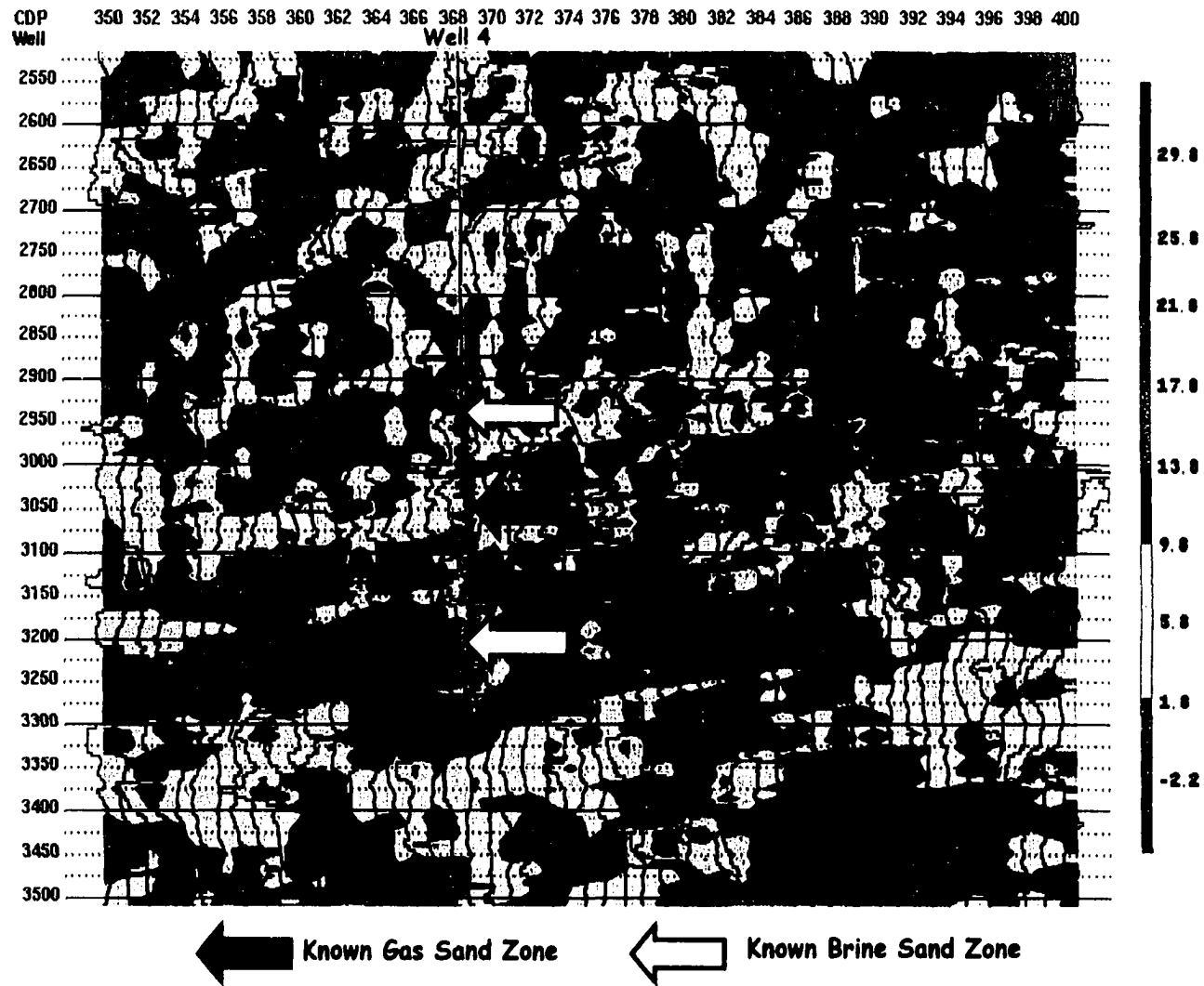


Figure 7.13b. Polarization angle difference ($\Delta\phi$) for seismic line 4. A black arrow indicates known gas zones, whereas a white arrow shows brine intervals.

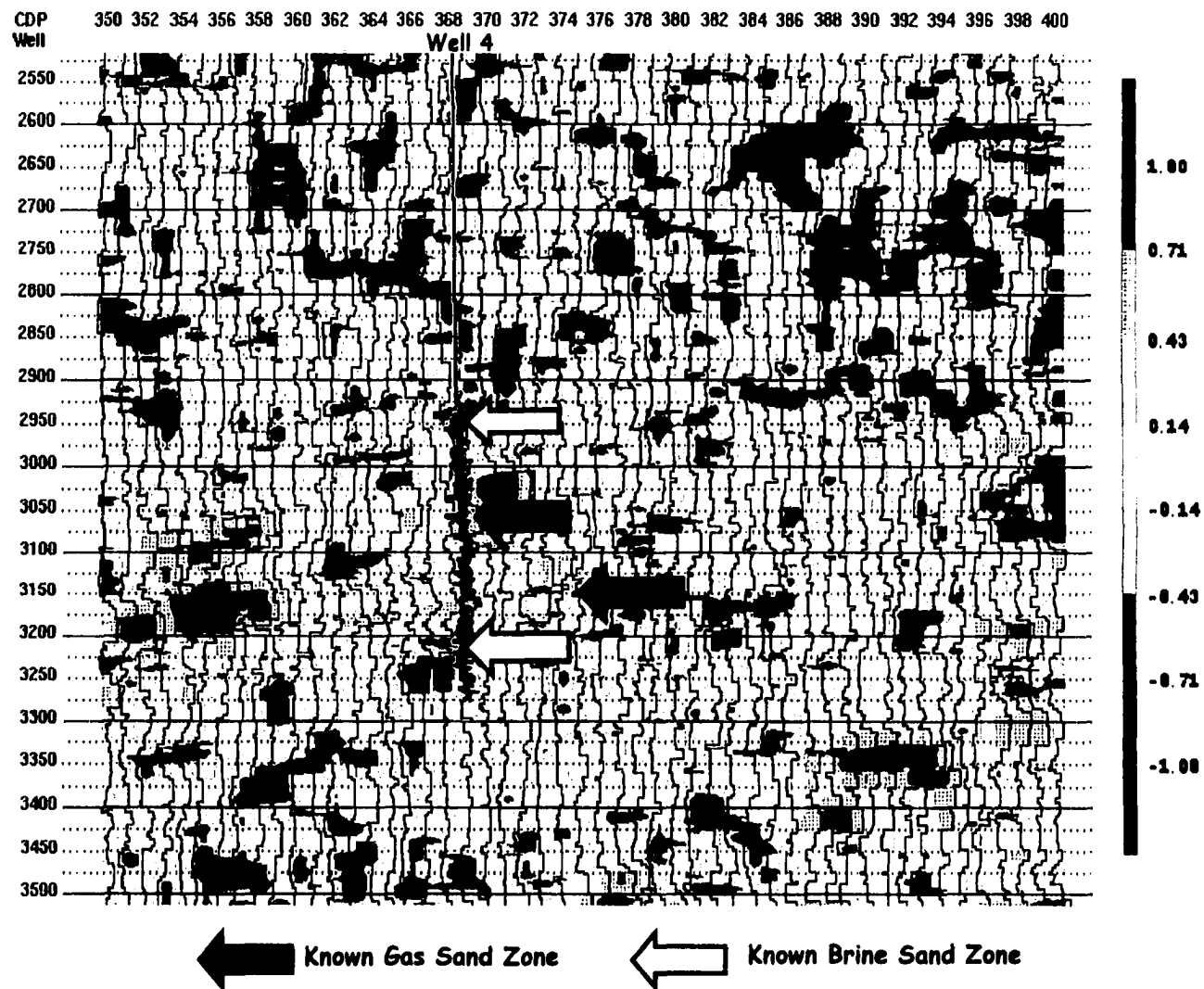


Figure 7.13c. AVO strength (L) for seismic line 4. Known gas zones are indicated by a black arrow, whereas a white arrow shows brine intervals.

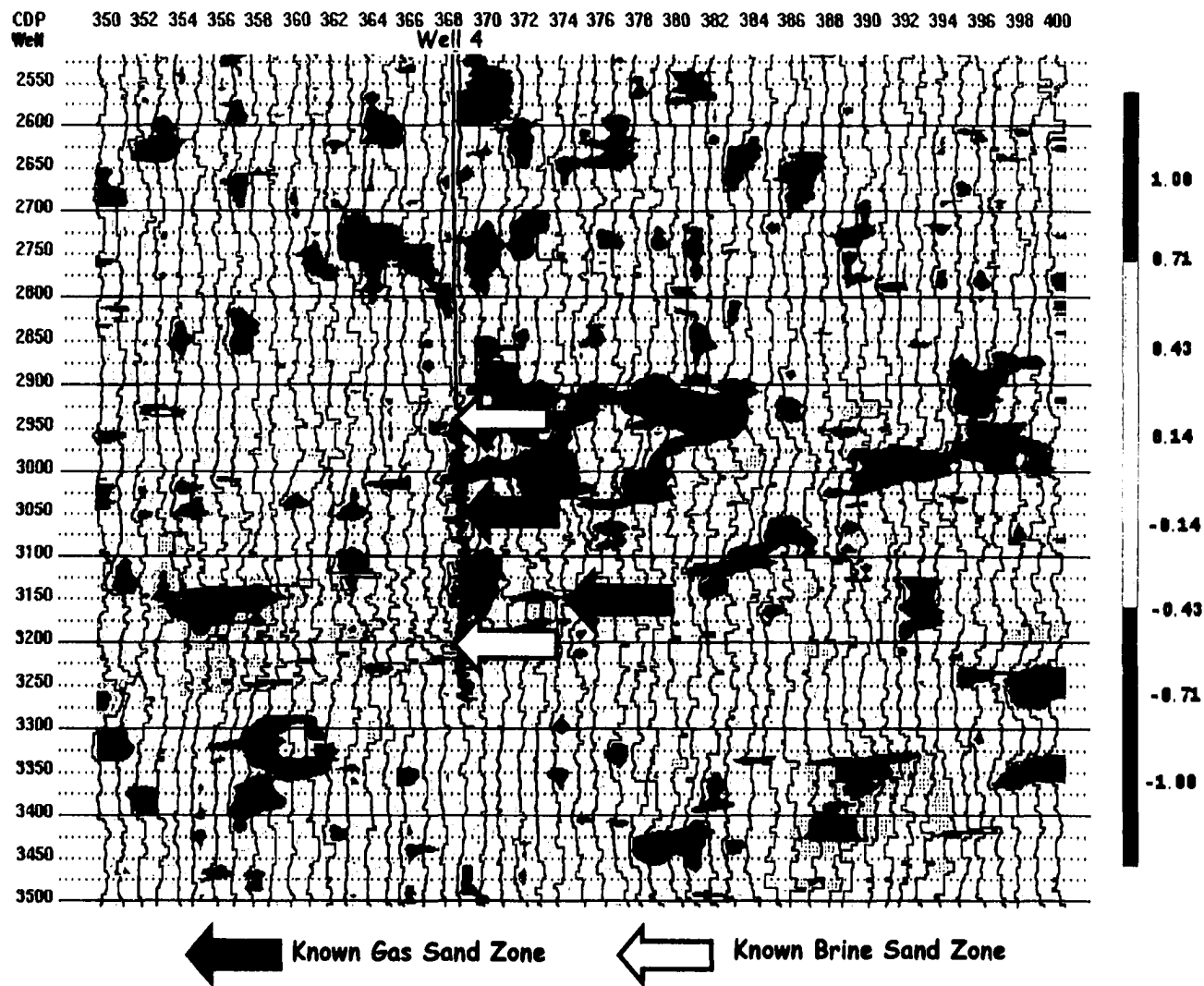


Figure 7.13d. Polarization product ($L\Delta\phi$) for seismic line 4. A black arrow indicates known gas sand zones, whereas a white arrow shows brine intervals.

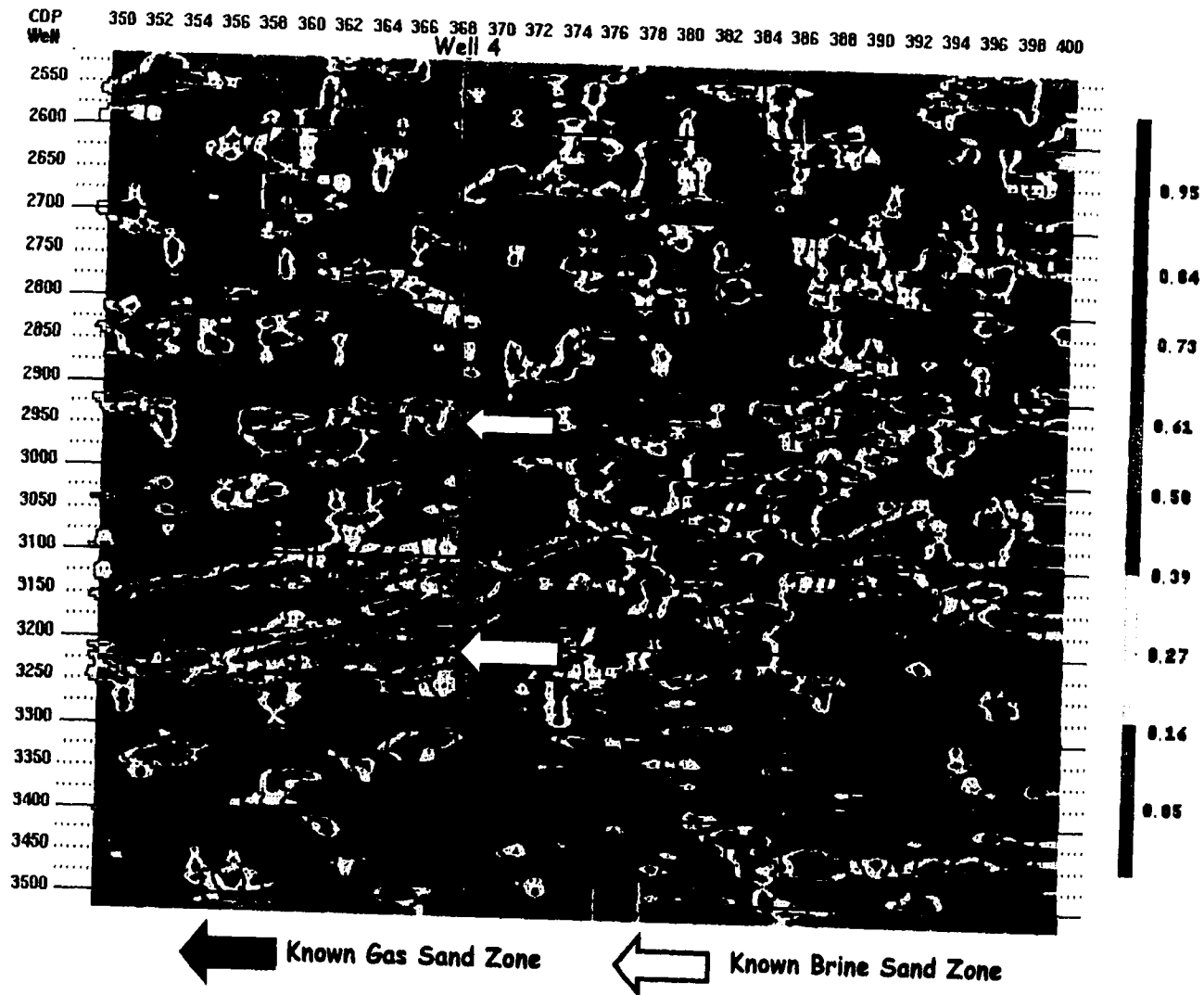


Figure 7.13e. Square of linear-correlation coefficient (r^2) for seismic line 4. A black arrow indicates known gas sand intervals, whereas a white arrow shows brine sand zones.

7.5 Discussion

From the conventional AVO attributes, large values of AVO product ($A*B$) and scaled Poisson's ratio change are associated with the presence of porous sand units. However, gas-charged sands of Class 3 exhibit larger positive values of AVO product as well as scaled Poisson's ratio change. Conventional AVO attributes help identify amplitude anomalies, but do not enhance the interpretation.

The polarization attributes generated at each seismic line show that porous gas sands correspond to large polarization product ($L\Delta\phi$), whereas brine sands do not. The square of the linear-correlation coefficient (r^2) provides an indication of the reliability of the result. It is clear that known hydrocarbon and brine intervals for the case study seismic lines exhibit different signatures on the polarization attributes. The AVO strength seems also a good indicator of porous gas sands. This is validated by the high values of the square of linear-correlation coefficient (≥ 0.60) in gas intervals, but intervals of large polarization product corresponding to brine sands (e.g. seismic line 3 at 3100 ms of TWT) have small values of r^2 (≤ 0.20), meaning that there is a high scattering of time sample points about the polarization trend within these analysis windows.

A large polarization product with large r^2 identifies every productive gas zone. The single large polarization product associated with brine had low r^2 .

The polarization attributes give a better resolution of the known gas and brine sand intervals than the conventional AVO attributes despite the fact that the latter also indicate the amplitude anomalies. In addition, the polarization attributes present a better enhancement of AVO interpretation when used in conjunction with the linear-correlation

correlation that the conventional AVO attributes. The AVO strength, the polarization product, and the linear-correlation coefficient seem to be the most useful attributes.

Chapter 8

CONCLUSIONS AND RECOMMENDATIONS

8.1 Conclusions

The main conclusions of this dissertation are:

- Polarization attributes should be considered as an alternative approach to identifying AVO anomalies.
- Polarization attributes can enhance AVO interpretation.
- Large polarization products and high linear-correlation coefficients from time windows along the traces are related to gas sand intervals.
- Polarization attributes can be used as a reconnaissance tool to identify possible hydrocarbon (gas) intervals.
- A real case study supported modeling results.

This work demonstrates how pre-stack P-wave data can be used to identify and delineate zones of larger polarization attribute values such as the polarization product from extracted intercept and gradient traces. The computation of polarization attributes from four 2-D seismic lines confirmed the results obtained through modeling of sand layers, gas and water-saturated, encased in shale and silt units. Time intervals of large polarization products (product of AVO strength and polarization angle difference) and high linear-correlation coefficients highlight gas zones.

Modeling is a key step in understanding amplitude anomalies observed on seismic data. Polarization attributes calculated from synthetic gathers, generated using a full elastic wave algorithm, have shown hydrocarbon (gas) intervals to be large anomalies

(Figures 7.10, 7.11, 7.12, and 7.13). In addition, from the modeling results on wave propagation and processing effects, the polarization angle seems almost insensitive to NMO errors (see Table 6.4 and Figure 6.8). There is a variation of 10% in angles for the modeling cases investigated. The time window size is very important in computing the polarization attributes (Figures 6.4, 6.5, and 6.6) and should be from half to a wave period.

AVO hodograms can be very useful when examining amplitude anomalies along single traces. Polarization attributes such as AVO strength (L), polarization product ($L\Delta\phi$), and linear-correlation coefficient (r^2) can help identify potential hydrocarbon (gas) zones when used conjointly.

8.2 Recommendations

The main recommendations of this dissertation are:

- Good signal-to-noise ratio seismic gathers with adequate offset range should be used for polarization attribute computations.
- The extraction of AVO intercept (A) and AVO gradient (B) should be done carefully to confirm the amplitude behavior with offset.
- An optimum time window should be used for the attribute calculations to honor the temporal resolution of the seismic data.
- The background angle or trend angle should be determined by examining the polarization angle of several traces within a given time window that can be hundreds of milliseconds in two-way time (TWT).

- Polarizations attributes should be used in conjunction in order to enhance a better AVO interpretation.

The AVO hodogram or polarization angle scheme presented in this dissertation can be extended to a truly three-dimensional AVO interpretation scheme, which would enable us to obtain lateral variations in the AVO responses that can be better correlated with the results provided by other methods.

Polarization attributes and AVO hodogram methodology can also be extended to other applications up-to-date such as multicomponent data analysis, coalbed methane detection, etc...

Finally, it is important to point out that studies involving AVO analysis and direct hydrocarbon detection must always be integrated with petrophysics, geological framework, and reservoir engineering, in order to improve or enhance AVO interpretation.

Future research on polarization attributes and hodograms should include:

- The determination of time-variant background polarization angles.
- The consideration of other attributes to better characterize reservoirs such as polarization product * sign (intercept), polarization product * sign (gradient).
- A 3-D implementation of the 2-D AVO hodogram or polarization angle algorithm presented in this dissertation
- An attempt to integrate AVO interpretation based on polarization attributes with multicomponent data analysis.

REFERENCES

- Adamick, J., Hall, D., Skoyles, D., DeWildt, J., and Erickson, J., 1994, AVO as an exploration tool; Gulf of Mexico case studies and examples: 64th Ann. Intern. Mtg., Soc. Expl. Geophys., Expanded Abstracts, 1107-1111.
- Aki, K., and Richards, P. G., 1980, Quantitative seismology: Theory and methods: W. H. Freeman and Co.
- Allen, J. L., and Peddy, C. P., 1993, Edge effects and out-of-plane effects *in* Levin, F. K., Ed., Amplitude variation with offset: Gulf Coast case studies, Soc. Expl. Geophys., 101-107.
- Barton, J., and Gullette, K., 1996, Reconnaissance amplitude versus offset techniques in the Niger Delta: Ann. Intern. Mtg., Am. Ass. Petr. Geol., Abstracts, AAPG Bulletin, **80**, 1272.
- Backus, M. M., Nepomuceno, F., and Cao, J.Z., 1982, The reflection seismogram in a solid layered earth: 52th Ann. Intern. Mtg., Soc. Expl. Geophys., Expanded Abstracts, 218-220.
- Bevington, P. R., 1969, Correlation probability, *in* Data reduction and error analysis for the physical sciences, McGraw-Hill, 119-132.
- Bortfeld, R., 1961, Approximation to the reflection and transmission coefficients of plane longitudinal and transverse waves: Geophys. Prosp., **9**, 485-503.
- Cardamone, M., Marini, I., and Bertelli, L., 1998, New 3D visualization and analysis tools improve prospect evaluation in a deep offshore environment: Ann. Intern. Mtg., Am. Ass. Petr. Geol., Abstracts, AAPG Bulletin, **82**, 1898.
- Castagna, J. P., and Smith, C. W., 1994, Comparison of AVO indicators: A modeling study: Geophysics, **59**, 1849-1855.
- Castagna, J. P., and Swan, H. W., 1997, Principles of AVO crossplotting: The Leading Edge, **16**, 337-342.
- Castagna, J. P., Swan, H. W., and Foster, D. J., 1998, Framework for AVO gradient and intercept interpretation: Geophysics, **63**, 948-956.
- Castagna, J. P., 1993, AVO analysis - Tutorial and review *in* Castagna, J. P., and Backus, M. M., Eds., Offset-dependent reflectivity - Theory and practice of AVO analysis, Soc. Expl. Geophys., 3-36.
- Castagna, J. P., The University of Oklahoma, Personal Communications, 1997-2001.

- Cerveny, V., and Ravindra, R., 1971, Theory of seismic head waves: Univ. of Toronto Press.
- Cooke, D. A., and Schneider, W. A., 1983, Generalized linear inversion of reflection seismic data: *Geophysics*, **48**, 665-676.
- Chapman, C. H., 1976, Exact and approximate generalized ray theory in vertically inhomogeneous media: *Geophys. J. R. Astr. Soc.*, **46**, 201.
- DiSiena, J. P., Gaiser, J. E., and Corrigan, D., 1981, Horizontal components and shear wave analysis of three-component VSP data, *in* Toksoz, M. N., and Stewart, R. R., Eds, Handbook of Geophysical Exploration, Vol. 14B: Advanced Concepts, Geophysical Press, 177-188.
- Domenico, S. N., 1984, Rock lithology and porosity determination from shear and compressional wave velocities: *Geophysics*, **49**, 1188-1195.
- Dong, W., 1998, AVO detectability against tuning and stretching artifacts: *Geophysics*, **64**, 494-503.
- Dong, W., 1996, Fluid line distortion due to migration stretch: 66th Ann. Intern. Mtg., Soc. Expl. Geophys., Expanded Abstracts, 1345-1348.
- Esmersoy, C., 1984, Polarization analysis, rotation and velocity estimation in three-component VSP, *in* Toksoz, M. N., and Stewart, R. R., Eds, Handbook of Geophysical Exploration, Vol. 14B: Advanced Concepts, Geophysical Press, 236-255.
- Ewing, W. M., Jardetzky, W. S., and Press, F., 1957, Elastic waves in layered media: McGraw-Hill, New York.
- Foster, D. J., Keys, R. G., and Reilly, J. M., 1997, Another perspective on AVO crossplotting: *The Leading Edge*, **16**, 1235-1237.
- Hidalgo, R., and Haryono, S., 2000, 3-D seismic imaging and interpretation of thin gas sandstone reservoirs using multi-attribute analysis on post-stack and AVO data, offshore SE Sumatra, Indonesia: Ann. Intern. Mtg., Am. Ass. Petr. Geol., Abstracts, AAPG Bulletin, **84**, 1438.
- Keho, T. H., 2000, The AVO hodogram: Using polarization to identify anomalies: 70th Ann. Intern. Mtg., Soc. Expl. Geophys., Expanded Abstracts, 1345-1348.
- Koefoed, O., 1955, On the effect of Poisson's ratio of rock strata on the reflection coefficients of plane waves: *Geophys. Prosp.*, **3**, 381-387.

- Kopsen, E., and McGann, G., 1985, A review of the hydrocarbon habitat of the eastern and central Borrow-Dampier Sub-Basin, Western Australia: *The APEA Journal*, **25**, 154-176.
- Knott, C. G., 1899, Reflexion and refraction of elastic waves with seismological applications: *Phil. Mag.*, **48**, 64-69.
- Lefevre, F., 1994, Fractured related anisotropy detection and analysis; "and if P-waves were enough?": 64th Ann. Intern. Mtg., Soc. Expl. Geophys., Expanded Abstracts, 942-945.
- Nelson, V., 1989, Display techniques for AVO analysis: 59th Ann. Intern. Mtg., Soc. Expl. Geophys., Expanded Abstracts, 447-448 .
- Ostrander, W. J., 1982, Method for interpretation of seismic records to yield indication of gaseous hydrocarbons: United States Patents No. 4,316,268.
- Ostrander, W. J., 1984, Plane-wave reflection coefficients for gas sands at nonnormal angles of incidence: *Geophysics*, **49**, 1637-1648.
- Ramos, A. C. B., 1996, Three-dimensional AVO analysis and anisotropic modeling applied to fracture characterization in coalbed methane reservoirs, Cedar Hill field, San Juan basin, New Mexico: Ph.D. dissertation, Colorado School of Mines.
- Rawlings, J. O., Pantula, S. G., and Dickey, D. A., 1998, Applied regression analysis: a research tool, second edition: Springer – Verlag New York, Inc.
- Richards, P. J., and Frasier, C. W., 1976, Scattering of elastic waves from depth-dependent inhomogeneities: *Geophysics*, **41**, 441-458.
- Ross, C. P., and Kinman, D. L., 1995, Non-bright spot AVO: Two examples: *Geophysics*, **60**, 1398-1408.
- Ross, C. P., 1992, Incomplete AVO near salt structures: *Geophysics*, **57**, 543-553.
- Ross, C. P., 2000, Effective AVO crossplot modeling: A tutorial: *Geophysics*, **65**, 700-711.
- Rueger, A., and Tsvankin, I., 1995, Azimuthal variation of AVO response for fractured reservoirs: 65th Ann. Intern. Mtg., Soc. Expl. Geophys., Expanded Abstracts, 1103-1106.
- Rutherford, S. R., and Williams, R. H., 1989, Amplitude-versus-offset variations in gas sands: *Geophysics*, **54**, 680-688.

- Sams, M., 1998, Yet another perspective on AVO crossplotting: *The Leading Edge*, **17**, 911-917.
- Sheriff, R. E., 1991, *Encyclopedic Dictionary of Exploration Geophysics*, 3rd Edition: Soc. Expl. Geophys.
- Shuey, R. T., 1985, A simplification of the Zoeppritz equations: *Geophysics*, **50**, 609-614.
- Smith, G. C., and Gidlow, P. M., 1987, Weighted stacking for rock property estimation and detection of gas: *Geophys. Prosp.*, **35**, 993-1014.
- Waters, K. H., 1981, *Reflection Seismology: A tool for energy resource exploration*: John Wiley & Sons, Inc.
- Wiggins, R., Kenny, G. S., and McClure, C. D., 1983, A method for determining and displaying the shear-velocity reflectivities of a geologic formation: European Patent Application 0113944.
- Wrolstad, K. H., 1988, AVO representations: 58th Ann. Intern. Mtg., Soc. Expl. Geophys., Expanded Abstracts, 1355.
- Young, G. B., and Braile, L. W., 1976, A computer program for the application of Zoeppritz' amplitude equations: *Bull. Seis. Soc. Am.*, **52**, 923-956.
- Zoeppritz, K., 1919, *Erdbebenwellen VIII B*, On the reflection and propagation of seismic waves: *Gottinger nachrichten*, I, 66-84.

Appendix A

MATRIX REPRESENTATION OF THE KNOTT-ZOEPPRITZ EQUATIONS

The complete Knott-Zoeppritz equations given by Aki and Richards (1980) are presented here in a matrix form.

For an interface between two semi-infinite elastic media, there are sixteen reflection and transmission coefficients (see Figure A-1). According to the Aki and Richards notation, the coefficients are represented by two letters (e.g. $\overset{\backslash}{P}\overset{/}{S}$). The first letter indicates the type of incident wave and the second letter represents the type of derived wave. The acute accent (/) indicates an upgoing wave while a downgoing wave has a grave accent (\). Hence, $\overset{\backslash}{P}\overset{/}{S}$ is the downgoing P-wave to upgoing S-wave coefficient. The scattering matrix, \mathbf{Q} , is

$$\mathbf{Q} = \begin{pmatrix} \overset{\backslash}{P}\overset{/}{P} & \overset{\backslash}{S}\overset{/}{P} & \overset{/}{P}\overset{/}{P} & \overset{/}{S}\overset{/}{P} \\ \overset{\backslash}{P}\overset{/}{S} & \overset{\backslash}{S}\overset{/}{S} & \overset{/}{P}\overset{/}{S} & \overset{/}{S}\overset{/}{S} \\ \overset{\backslash}{P}\overset{\backslash}{P} & \overset{\backslash}{S}\overset{\backslash}{P} & \overset{\backslash}{P}\overset{\backslash}{P} & \overset{\backslash}{S}\overset{\backslash}{P} \\ \overset{\backslash}{P}\overset{\backslash}{S} & \overset{\backslash}{S}\overset{\backslash}{S} & \overset{\backslash}{P}\overset{\backslash}{S} & \overset{\backslash}{S}\overset{\backslash}{S} \end{pmatrix} = \underset{-}{P}^{-1} \underset{-}{R} \quad (\text{A-1})$$

where $\underset{-}{P}$ is the matrix

$$\begin{pmatrix} -\sin\theta_1 & -\cos\phi_1 & \sin\theta_2 & \cos\phi_2 \\ \cos\theta_1 & -\sin\phi_1 & \cos\theta_2 & -\sin\phi_2 \\ 2\rho_1 V_{S1} \sin\phi_1 \cos\theta_1 & \rho_1 V_{S1} (1-2\sin^2\phi_1) & 2\rho_2 V_{S2} \sin\phi_2 \cos\theta_2 & \rho_2 V_{S2} (1-2\sin^2\phi_2) \\ -\rho_1 V_{P1} (1-2\sin^2\phi_1) & \rho_1 V_{S1} \sin 2\phi_1 & \rho_2 V_{P2} (1-2\sin^2\phi_2) & -\rho_2 V_{S2} \sin 2\phi_2 \end{pmatrix}$$

and R is the matrix

$$\begin{pmatrix} \sin\theta_1 & \cos\phi_1 & -\sin\theta_2 & -\cos\phi_2 \\ \cos\theta_1 & -\sin\phi_1 & \cos\theta_2 & -\sin\phi_2 \\ 2\rho_1 V_{S1} \sin\phi_1 \cos\theta_1 & \rho_1 V_{S1} (1-2\sin^2\phi_1) & 2\rho_2 V_{S2} \sin\phi_2 \cos\theta_2 & \rho_2 V_{S2} (1-2\sin^2\phi_2) \\ \rho_1 V_{P1} (1-2\sin^2\phi_1) & -\rho_1 V_{S1} \sin 2\phi_1 & -\rho_2 V_{P2} (1-2\sin^2\phi_2) & \rho_2 V_{S2} \sin 2\phi_2 \end{pmatrix}$$

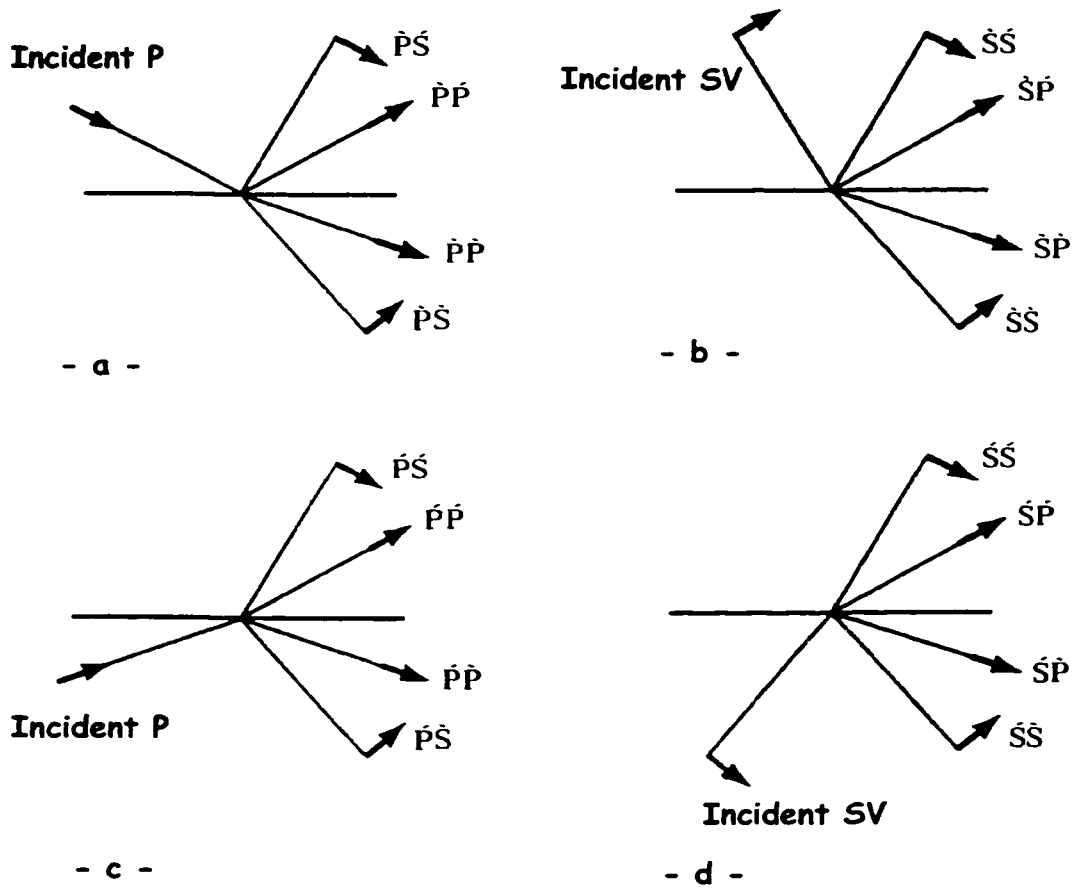


Figure A- 1. Notation for the sixteen possible reflection/transmission coefficients for P and SV waves at an interface between two different medium half-spaces. Short arrows show the directions of particle motion (Modified from Aki and Richards, 1980).

Appendix B

DERIVATION OF THE POLARIZATION VECTOR COMPONENTS

The polarization vector is determined by eigenvector analysis. The formulation is:

$$|R_m - \lambda I| = 0 \quad (\text{B-1})$$

where

R_m , the correlation matrix of the AVO intercept (A) and gradient (B), is defined as:

$$R_m = \frac{1}{2N+1} \begin{pmatrix} \sum_{i=-N}^N A_{t+i}^2 & \sum_{i=-N}^N A_{t+i} B_{t+i} \\ \sum_{i=-N}^N A_{t+i} B_{t+i} & \sum_{i=-N}^N B_{t+i}^2 \end{pmatrix} \quad (\text{B-2})$$

I is the unity matrix:

$$I = \begin{pmatrix} 1 & 0 \\ 0 & 1 \end{pmatrix} \quad (\text{B-3})$$

and

λ represents the eigenvalues.

Hence, the eigenvalue matrix from Equation B-1 is:

$$\frac{1}{2N+1} \begin{pmatrix} \sum_{i=-N}^N A_{t+i}^2 - \lambda & \sum_{i=-N}^N A_{t+i} B_{t+i} \\ \sum_{i=-N}^N A_{t+i} B_{t+i} & \sum_{i=-N}^N B_{t+i}^2 - \lambda \end{pmatrix} \quad (\text{B-4})$$

The eigenvalues are obtained by solving the determinant of the matrix presented in Equation B-4. The two values of λ are:

$$\lambda_1 = \frac{1}{2} \left(\sum_{i=-N}^{i=N} A_{t+i}^2 + \sum_{i=-N}^{i=N} B_{t+i}^2 - \sqrt{\left(\left(\sum_{i=-N}^{i=N} A_{t+i}^2 - \sum_{i=-N}^{i=N} B_{t+i}^2 \right)^2 + 4 \left(\sum_{i=-N}^{i=N} A_{t+i} \sum_{i=-N}^{i=N} B_{t+i} \right)^2 \right)} \right) \quad (\text{B-5})$$

$$\lambda_2 = \frac{1}{2} \left(\sum_{i=-N}^{i=N} A_{t+i}^2 + \sum_{i=-N}^{i=N} B_{t+i}^2 + \sqrt{\left(\left(\sum_{i=-N}^{i=N} A_{t+i}^2 - \sum_{i=-N}^{i=N} B_{t+i}^2 \right)^2 + 4 \left(\sum_{i=-N}^{i=N} A_{t+i} \sum_{i=-N}^{i=N} B_{t+i} \right)^2 \right)} \right)$$

In our application, only the largest eigenvalue of the two, λ_2 , is considered for the determination of the unit eigenvector. The components of the eigenvector are P_x and P_y .

After substituting λ_2 in the eigenvalue matrix, and rearranging common terms, the matrix is multiplied by the eigenvector:

$$\frac{1}{2N+1} \begin{pmatrix} \sum_{i=-N}^N A_{t+i}^2 - \lambda_2 & \sum_{i=-N}^N A_{t+i} B_{t+i} \\ \sum_{i=-N}^N A_{t+i} B_{t+i} & \sum_{i=-N}^N B_{t+i}^2 - \lambda_2 \end{pmatrix} \cdot \begin{pmatrix} P_x \\ P_y \end{pmatrix} = 0 \quad (\text{B-6})$$

Since the unit vector is considered, the following condition is set:

$$P_x^2 + P_y^2 = 1 \quad (\text{B-7})$$

The components of the unit eigenvector, obtained by solving Equations B-6 and B-7, are:

$$\begin{pmatrix} P_x \\ P_y \end{pmatrix} = \begin{pmatrix} \frac{\sqrt{2}}{[1+D]^{\frac{1}{2}}} \frac{\sum_{i=-N}^N A_{t+i} B_{t+i}}{\sqrt{4 \left(\sum_{i=-N}^N A_{t+i} B_{t+i} \right)^2 + \left(\sum_{i=-N}^N A_{t+i}^2 - \sum_{i=-N}^N B_{t+i}^2 \right)^2}} \\ \frac{\sqrt{2}}{2} [1+D]^{\frac{1}{2}} \end{pmatrix} \quad (\text{B-8})$$

where

$$D = \frac{\left(\sum_{i=-N}^N A_{t+i}^2 - \sum_{i=-N}^N B_{t+i}^2 \right)}{\sqrt{4 \left(\sum_{i=-N}^N A_{t+i} B_{t+i} \right)^2 + \left(\sum_{i=-N}^N A_{t+i}^2 - \sum_{i=-N}^N B_{t+i}^2 \right)^2}} \quad (\text{B-9})$$

Therefore, the components of the unit eigenvector are the components of the polarization vector.